

University of Alberta

Robust contactless sensor for real-time vital signs monitoring

by

Kevin Khee Meng Chan

A thesis submitted to the Faculty of Graduate Studies and Research
in partial fulfillment of the requirements for the degree of

Doctor of Philosophy

in

Electromagnetics and Microwaves

Department of Electrical and Computer Engineering

© Kevin Khee Meng Chan

Spring 2014

Edmonton, Alberta

Permission is hereby granted to the University of Alberta Libraries to reproduce single copies of this thesis and to lend or sell such copies for private, scholarly or scientific research purposes only. Where the thesis is converted to, or otherwise made available in digital form, the University of Alberta will advise potential users of the thesis of these terms.

The author reserves all other publication and other rights in association with the copyright in the thesis and, except as herein before provided, neither the thesis nor any substantial portion thereof may be printed or otherwise reproduced in any material form whatsoever without the author's prior written permission.

Abstract

Wireless sensing find many biomedical applications due to the benefit and convenience of having no contact with the patients. Low power radio waves, that are biologically safe, can monitor the patient's medical conditions such as the breathing and heart beat rate. Electro-magnetic (EM) waves extract the small movements of the chest and heart via field disturbance phenomena. The patient's breathing and heart beat modulate the radio waves for the vital signs to be monitored in real-time.

Ultra-wideband (UWB) radar is an EM scattering technology that has been proven to discriminate targets with less than 30mm range resolution, which is smaller than the average size of a human heart. The UWB radar emits 200ps pulses that occupy a bandwidth from 3 to 10GHz. For linearly polarized radiation, the radar cross-section (RCS) of a moving target having complex shapes such as the thorax section of a human body causes regular fading. The scattering from a complex target rotates the radio wave vector to result in non-optimal signal reception due to polarization losses.

The research focuses on the design of a circularly polarized (CP) UWB radar system for contactless vital signs monitoring of a patient. Circular polarization is introduced to address the fading RCS problem thus achieving a more robust system.

The same CP UWB radar system with radio waves that penetrate through dielectric objects can be used for time-critical rescue operations in locating survivors buried under collapsed structures or in buildings engulfed in flames where visibility is hampered. Furthermore, by employing material characterization and microwave imaging techniques, it is possible to use the proposed system for other biomedical applications such as tumor localization and damaged tissue identification.

The thesis is organized as follows. Firstly, the operation of UWB radar is presented and the research topic addressed. The pulse generator design suited for low pulse repetition rates is then introduced. The design of a decade bandwidth circularly polarized antenna array is described. The methodology and performance of the robust vital signs monitoring system is shown and compared with the linear polarized counterpart. A new method for material characterization using time domain RCS measurements is demonstrated. The future work is finally proposed.

Acknowledgements

First and foremost, I would like to thank my supervisor Dr. Rambabu Karumudi for giving me the opportunity to come to the University of Alberta and embark on this journey of learning through the PhD program. Through his training, mentorship and guidance, I have developed a greater understanding on the body of knowledge around the technology of time-domain electromagnetics and their related concepts. His trust to me has been crucial in producing the work that is reported in this thesis. His friendship has grown me beyond the classroom and lab, to benefit and mature me in my personal life.

Next, I am grateful to my colleagues, Dr. Adrian Tan and Lin Li for their collaboration with me. Co-working together established the next level of know-how, built upon the foundation that Dr. Rambabu laid on us and of what was there beforehand from our past experiences. Our combined diligence and perseverance pushed the boundaries of the collective knowledge that we had, to contribute to the community.

Alberta Innovates Technology Futures and Natural Sciences and Engineering Research Council are acknowledged for providing me with scholarship and research assistantship to support the work that we carried out.

I thank my wife, Jeannie, for her sacrifices to be with me through this journey and for supporting me through words and deeds. Her provision put my mind at ease to focus on the work at hand. Her help though in the background, contributed in finishing the tasks done in the foreground. Also thanks to my family and friends for their prayers and help that supported the completion of the work.

Last but not least, I thank God for making it all happen!

Contents

Chapter 1 - Introduction	1
1.1 Principles of UWB radar	3
1.2 Contributions of this work.....	8
Chapter 2 - Pulse generator	10
2.1 Types of pulse generator	10
2.2 Limitations of the shunt mode step recovery diode pulse generator	13
2.3 The cascaded shunt mode step recovery diode pulse generator	14
2.4 Optimization for pulse amplitude.....	16
2.5 Optimization for pulse width.....	18
2.6 Performance of the optimized pulse generator.....	19
Chapter 3 - Decade bandwidth circularly polarized antenna array	22
3.1 180° hybrid coupler	23
3.1.1 Types of 180° hybrid coupler.....	24
3.1.2 The asymmetric tapered 8.34dB 180° hybrid coupler.....	24
3.1.3 3dB 180° hybrid coupler	26
3.1.4 Results.....	32
3.2 Quadrature hybrid coupler.....	36
3.2.1 Types of quadrature hybrid coupler	36
3.2.2 The symmetric 3dB quadrature hybrid coupler.....	37
3.2.3 Optimization of the symmetric coupler design	38
3.2.4 Results.....	40

3.3	Integrated feed network.....	42
3.3.1	Design	42
3.3.2	Results.....	43
3.4	Circularly polarized antenna array	47
Chapter 4 - Robust contactless sensor for real-time vital signs monitoring.....		54
4.1	System design.....	55
4.2	Time expanded correlation receiver	58
4.3	Circularly polarized antenna	65
4.4	Vital signs monitoring application	67
Chapter 5 - Dielectric material characterization using time domain RCS:		
A feasibility study for fat characterization.....		71
5.1	Methodology	72
5.1.1	Theory	72
5.1.2	Procedure	74
5.1.3	The case of thin dielectrics.....	75
5.1.4	Frequency response of the relative permittivity	76
5.1.5	Thickness estimation.....	76
5.2	Experimental validation	77
5.2.1	Far-field measurements.....	78
5.2.2	Near-field measurements	82
5.2.3	Multi-layered MUTs	86
5.3	Application	87
5.4	Circularly polarized material characterization	89

Chapter 6 - Future work	91
6.1 Single circularly polarized antenna array radar system.....	91
6.2 Characterization of internal organs	93
6.3 Determining blood oxygen levels in real-time during surgery.....	94
Bibliography	97

List of Tables

Table 1.1 Pulse width relation to bandwidths for various Gaussian pulses.....	7
Table 2.1 Types of pulse generators.....	11
Table 3.1 Impedances and dimensions of the nine section symmetric quadrature hybrid...	37
Table 3.2 Optimized design dimensions for the proposed quadrature hybrid.....	38
Table 3.3 Received pulses with antenna rotation.....	52
Table 4.1 System measurements of various polarization configurations.....	70
Table 4.2 Comparison of radars for vital signs monitoring.....	70
Table 5.1 Measured ϵ_r for various MUTs using (5-5).....	79
Table 5.2 MUT thickness measurements.....	82
Table 5.3 Measured ϵ_r at near-field distance using (5-5).....	84
Table 5.4 MUT thickness using near-field data.....	86
Table 5.5 Measured ϵ_r for two MUT layers.....	87

List of Figures

Fig. 1.1	Illustration of centralized contactless real-time vital signs monitoring system	2
Fig. 1.2	Bandwidth of a pulse of 200ps duration.....	4
Fig. 1.3	Bandwidth of time-gated 6.5GHz sinusoid with 200ps pulse duration....	4
Fig. 1.4	Non-aliased adjacent pulses at system range resolution.....	5
Fig. 1.5	Example representation of UWB radar operating at system range resolution.....	5
Fig. 1.6	Received signals of example radar operating at system range resolution.	5
Fig. 1.7	Block diagram of the proposed circularly polarized UWB radar system..	9
Fig. 2.1	Schematic diagram of the shunt mode SRD harmonic generator.....	11
Fig. 2.2	Charge storage and minority carrier recombination with respect to input voltage.....	12
Fig. 2.3	Schematic diagram of the proposed UWB radar pulse generator.....	14
Fig. 2.4	Effect of L_1 on output pulse ($L_2=12\text{nH}$, $C_1=3.9\text{pF}$, $V_{in}=10\text{V CW}$).....	16
Fig. 2.5	Effect of SRD_1 on output pulse ($L_1=22\text{nH}$, $L_2=12\text{nH}$, $C_1=3.9\text{pF}$, $V_{in}=10\text{VCW}$).....	17
Fig. 2.6	Simulation to compare single and cascaded stages.....	17
Fig. 2.7	Effect of L_2 on output pulse ($L_1=3.9\text{nH}$, $C_1=3.9\text{pF}$, $V_{in}=10\text{V CW}$).....	18
Fig. 2.8	Photograph of the UWB radar pulse generator prototype.....	19
Fig. 2.9	Outputs of prototype compared with single stage design for 10MHz CW input.....	20
Fig. 2.10	Output of prototype compared with single stage design for square wave input.....	21
Fig. 3.1	Schematic of UWB CP radar antenna feed network.....	23
Fig. 3.2	Schematic of tapered coupled line hybrid.....	24
Fig. 3.3	Tandem connection of two hybrid couplers.....	26
Fig. 3.4	Reflection coefficient of the coupled lines for various lengths.....	28
Fig. 3.5	Even and odd mode impedances of the coupled lines.....	29
Fig. 3.6	Dimensions of the coupled lines along the coupling section.....	30
Fig. 3.7	Structure of the 180° hybrid with gap and overlap grounds.....	30
Fig. 3.8	Line widths for various gaps and overlaps of grounds.....	32

Fig. 3.9	Input port return loss (S_{11}) and isolation (S_{31}) responses.....	33
Fig. 3.10	Through (S_{21}) and coupled (S_{41}) ports responses.....	33
Fig. 3.11	Phase difference between the coupled and through ports of the prototype 180° hybrid.....	34
Fig. 3.12	Time-domain input and outputs for the proposed 180° hybrid.....	34
Fig. 3.13	Simulation result of hybrid with lengthened meander line to correct for phase error.....	35
Fig. 3.14	Time domain measurement setup.....	35
Fig. 3.15	Simulation results of hybrid without and with offset grounds.....	36
Fig. 3.16	Structure of the nine section symmetric quadrature hybrid.....	38
Fig. 3.17	Impedances versus normalized length for the optimized quadrature hybrid.....	39
Fig. 3.18	Structure of the proposed quadrature hybrid coupler.....	39
Fig. 3.19	Input port return loss (S_{11}) and isolation (S_{31}).....	40
Fig. 3.20	Through (S_{21}) and coupled (S_{41}) ports.....	41
Fig. 3.21	Phase difference between coupled and through ports.....	41
Fig. 3.22	Time-domain input and outputs for the proposed quadrature hybrid.....	42
Fig. 3.23	Structure of the proposed integrated feed network.....	43
Fig. 3.24	Photograph of the middle substrate layer with connectors.....	43
Fig. 3.25	Input port return loss (S_{11}).....	44
Fig. 3.26	Isolated ports ($S_{31} - 90^\circ$ hybrid, S_{21} and $S_{41} - 180^\circ$ hybrid).....	44
Fig. 3.27	Through (S_{51}) and coupled ports (S_{61} , S_{71} , S_{81}).....	45
Fig. 3.28	Phase differences between coupled and through ports.....	45
Fig. 3.29	Time-domain input and output pulses for the proposed integrated feed network.....	46
Fig. 3.30	Dimensions of the antenna array element.....	47
Fig. 3.31	Circularly polarized antenna array arrangement.....	48
Fig. 3.32	Photograph of the antenna array mounted on antenna measurement system.....	48
Fig. 3.33	Reflection coefficient of the element and antenna array.....	49
Fig. 3.34	Radiation patterns; (a),(b): 1GHz, (c),(d): 5.5GHz, (e),(f): 10GHz; azimuth (left) and elevation (right).....	50
Fig. 3.35	Axial ratio for CP antenna array.....	51
Fig. 3.36	Simulated gain as a function of frequency.....	51

Fig. 3.37 Phase center and propagation delay of the antenna array.....	51
Fig. 3.38 Phase center measurement set-up.....	51
Fig. 4.1 Schematic of the UWB radar system.....	56
Fig. 4.2 Spectrum of the output pulse.....	57
Fig. 4.3 Photograph of the UWB radar hardware.....	58
Fig. 4.4 Block diagram of stored reference correlation receiver.....	59
Fig. 4.5 Example of a 1000 times expanded waveform.....	60
Fig. 4.6 Example UWB radar system with target at 1m.....	60
Fig. 4.7 Received 10MHz PRF pulses of target at 1m.....	61
Fig. 4.8 Non-overlapped reference pulse.....	61
Fig. 4.9 Reference pulse delayed by 100ps.....	62
Fig. 4.10 IF output with respect to delay of reference pulse.....	62
Fig. 4.11 IF port output with respect to delay of dirac-delta impulse at LO port....	63
Fig. 4.12 LO and RF pulses and integrator output at PRI #65.....	64
Fig. 4.13 LO and RF pulses and integrator output at PRI #66.....	65
Fig. 4.14 Interpolated time-expanded waveform from integrator output.....	65
Fig. 4.15 a) “Cross” structure b) “Box” structure.....	66
Fig. 4.16 Return loss of combined feed network and antenna array.....	66
Fig. 4.17 Axial ratio performance of the CP antenna.....	67
Fig. 4.18 Photograph of CP UWB radar system for vital signs monitoring.....	68
Fig. 4.19 Spectral and time-domain plots of radar system measurements.....	69
Fig. 5.1 Experimental validation test set-up.....	77
Fig. 5.2 Transmitted and received pulses for Granite (MUT).....	78
Fig. 5.3 Time gated pulses for Granite (MUT).....	79
Fig. 5.4 Material characteristics of Granite slab.....	80
Fig. 5.5 Material characteristics of Marble slab.....	80
Fig. 5.6 Material characteristics of Formica laminate sheet.....	81
Fig. 5.7 Material characteristics of Gypsum board.....	81
Fig. 5.8 Impulse response, $r'_{MUTc}(t)$, of the Granite slab.....	82
Fig. 5.9 Geometry of the near-field measurement set-up.....	83
Fig. 5.10 Near-field measurement with large metal plate used for calibration.....	83
Fig. 5.11 Material characteristics of Granite slab in near field.....	84
Fig. 5.12 Material characteristics of Marble slab in near field.....	85
Fig. 5.13 Material characteristics of Formica sheet in near field.....	85

Fig. 5.14 Material characteristics of Gypsum board in near field.....	86
Fig. 5.15 Test set-up for fat localization using phantom model (porcine tissue)....	88
Fig. 5.16 ϵ_r mapping of the pig's fat and flesh measurements.....	89
Fig. 6.1 Test set-up for single circularly polarized antenna array radar system.....	91
Fig. 6.2 Pulses recorded at ports 1 (S_{11}) and 3 (S_{21}) of the feed network.....	92
Fig. 6.3 Relative permittivity of blood at various oxygenation percentages.....	95
Fig. 6.4 Loss tangent of blood at various oxygenation percentages.....	95
Fig. 6.5 Loss tangent of oxygenated blood from 1 to 3GHz.....	96

List of Symbols

τ	Pulse duration
f_c	Center frequency
c	Speed of wave propagation in free space
ϵ_r	Relative permittivity
Q	Stored charges
I_f	Forward current
τ_L	Diode lifetime
T_f	Period of forward conduction
T_s	Diode recombination time
I_r	Reverse current
C_v	Diode junction capacitance
A_d	Diode junction area
d	Distance between the conducting plates in diode
ϵ	Permittivity
T_t	Diode transition time
G_q	Diode impedance transition time
G_{RLC}	Diode residual charge transmission time
C_d	Diode reverse bias capacitance
τ_s	System pulse width
R_L	Load resistor
h	Height of the substrate (thickness)
λ	Wavelength
z	Position along coupler's length
L	Length of the coupler
Z_o	Characteristic impedance
k	Coupling factor
V	Voltage input into coupler
θ	Phase
β	Propagation constant
$\delta\theta$	Phase difference between even/odd transmission coefficients
C	Coupling coefficient of the coupler
Z_{oe}	Even mode impedance
Z_{oo}	Odd mode impedance

x	Position on the taper's length
l	Length of taper
ρ_o	Zero frequency reflection coefficient of the even mode
λ_m	Cut-off wavelength of the coupler
ρ_{om}	Maximum passband ripple
s	Normalized thickness of the middle substrate
v	Speed of wave propagation in the dielectric
μ	Permeability
C_l	Capacitance per unit length in dielectric
ρ_j	Surface charge density of sub-length section j
n	Section number
δ	Length of section
l_q	Length of quadrature hybrid coupler
λ_c	Wavelength of the centre frequency
T_d	Time delay
σ_{MUT}	RCS of the MUT
σ_∞	RCS of perfectly conducting MUT
Γ_{MUT}	Reflection coefficient of the MUT
η_{MUT}	Intrinsic impedance of the MUT
η_x	Intrinsic impedance of the medium prior to MUT
η	Intrinsic impedance
η_o	Intrinsic impedance of free-space
σ_{avg}	Frequency averaged RCS
$r(t)$	Received pulse at the receiving antenna
$s(t)$	Transmitted pulse fed to the transmitting antenna
R	Distance from the antenna to the MUT
h_{et}	Effective height of the transmitting antenna
h_{er}	Effective height of the receiving antenna
A_s	Area of calibration metal plate
R	Distance from radar to target
$r_m(t)$	Reflected pulse from metal plate
$r_d(t)$	Ambient pulse
$r_{mc}(t)$	Calibrated pulse for metal plate
B_s	Area of the MUT
$r_{MUT}(t)$	Reflected pulse from MUT
$r_{MUTc}(t)$	Corrected pulse for MUT
$r'_{mc}(t)$	Scaled calibrated pulse for metal plate

$\sigma_{avg_r'mc}(t)$	Frequency averaged RCS for the scaled metal plate
$\sigma_{avg_rMUTc}(t)$	Frequency averaged RCS for the MUT
r	Free space range resolution
BW	Bandwidth of the radar system
ϵ'_r	Real part of relative permittivity
$\tan \delta$	Loss tangent of material
$r'_{mc}(\omega)$	Frequency response of the scaled calibrated pulse for metal plate
$r_{MUT}(\omega)$	Frequency response of the MUT pulse
$\Gamma_{MUT}(\omega)$	Frequency response of the MUT's reflection coefficient
$\epsilon_r(\omega)$	Frequency response of the MUT's relative permittivity
$\tan \delta(\omega)$	Frequency response of the MUT's loss tangent
$r'_{MUTc}(t)$	MUT impulse response after deconvolution

List of Abbreviations

UWB	Ultra-wideband
EM	Electro-magnetic
RCS	Radar cross-section
CP	Circularly polarized
SARS	Severe acute respiratory syndrome
PPG	Photoplethysmography
LED	Light emitting diode
ICU	Intensive care unit
FCC	Federal Communications Commission
Tx	Transmitter
Rx	Receiver
FWHM	Full Width at Half Maximum
IF	Intermediate frequency
LO	Local oscillator
RF	Radio frequency
LNA	Low noise amplifier
PC	Personal computer
CMOS	Complementary metal oxide semiconductor
FET	Field effect transistor
SRD	Step-recovery diode
NLTL	Non-linear transmission line
MIC	Microwave integrated circuit
PRF	Pulse repetition frequency
PRT	Pulse repetition period
CW	Continuous wave
GPS	Global Positioning System
SatCom	Satellite Communications
SDARS	Satellite Digital Audio Radio Service
RFID	Radio Frequency Identification
AR	Axial ratio
MOM	Method of Moments
IFN	Impulse forming network
GA	Genetic Algorithm

LHCP	Left-hand circularly polarized
ECG	Electro-cardiographs
MTI	Moving Target Indicator
DC	Direct current
LP	Linearly polarized
DDS	Direct digital synthesizer
A/D	Analog-to-digital
ADC	Analog-to-Digital Converter
PRI	Pulse repetition interval
DETASA	Dual elliptically tapered antipodal slot antenna
RHCP	Right-hand circularly polarized
FFT	Fast Fourier transform
LPH	Horizontal polarization
MUT	Material under test
P.O.	Physical optics
SNR	Signal-to-noise ratio

Chapter 1

Introduction

Air-borne viruses and communicable diseases have become more prevalent in the past decade as evidenced by numerous epidemics such as the H1N1, avian flu and severe acute respiratory syndrome (SARS). As new strains of viruses surface, cures take time to develop. Therefore preventive measure for rapid spread is an important recourse. For the measuring and monitoring of patients' vital signs, contactless and remote sensing based systems are desired for the containment of disease spreading.

Health professionals have to periodically examine the breathing and heart beat rates of patients in hospital wards. The conventional technique for recording breathing rates is to visually count the number of times the chest of a patient rise and fall for a set period of time. This could be inaccurate due to human errors. Heart beat monitoring is usually done using electrodes attached to various locations on the chest, arms or legs of the patient. This can cause discomfort and inconvenience to the patient. Germs and diseases can also spread through the electrodes. A modern method includes photoplethysmography (PPG) [1], which uses an infra-red light emitting diode (LED) and a photodiode pair to probe the blood flow through the capillaries by measuring the scattered light intensity over time. Although this method is contact based, it is non-invasive and low cost. Because it allows continuous monitoring, PPG is gaining popularity. A Doppler radar-based solution is presented in [2] for monitoring respiration rate. This is a viable solution for the above needs. However, due to the reported phase noise problems and its narrow band nature, it suffers from performance instabilities. The Doppler radar and PPG methods have problems with precision when the patients move. Improvements for these systems still have to be developed. An alternative contactless and robust method is preferred to overcome the existing deficiencies. The ultra-wideband (UWB) radar technique is a wireless method that has a high range resolution of better than 3cm. This system can measure the finer body movements to capture the breathing and heart beat rates. Circular polarized radiation can improve the robustness of received signals from the human body and irregularly shaped contours by reducing signal fading.

In an intensive care unit (ICU) scenario, multiple patients have to be monitored in real-time round the clock by a limited number of staff. Automating vital signs monitoring provides timely information especially when a patient's vital signs deteriorate to dangerous levels. In this process, precious lives may be saved or conditions prevented from worsening when resources are allocated to the most needed patients. Hospital procedures can be optimized with a centralized automated vital signs monitoring system whereby multiple patients' vital signs are continuously being monitored in real-time.

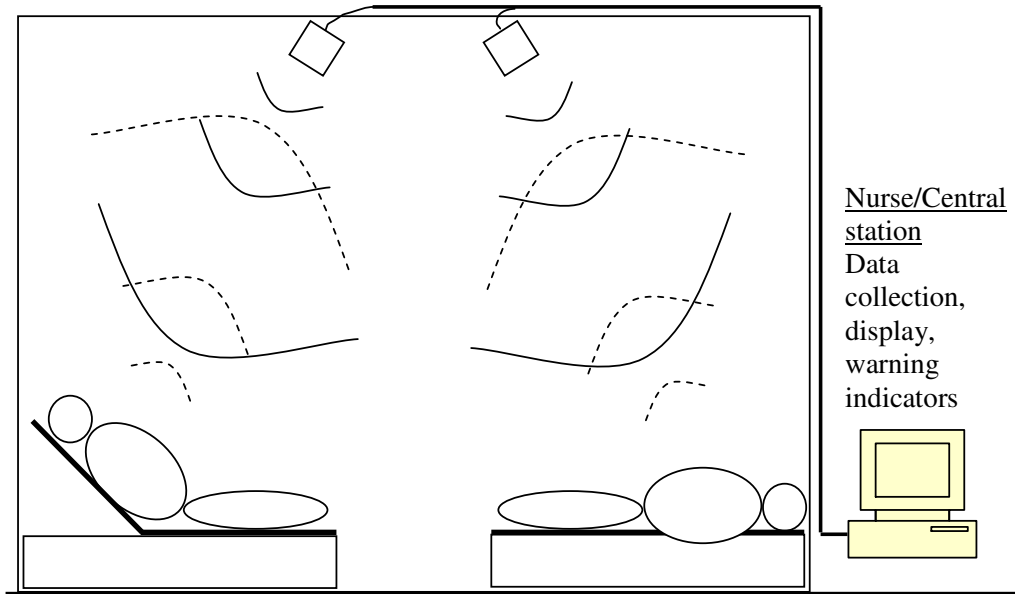


Fig. 1.1 - Illustration of centralized contactless real-time vital signs monitoring system.

An illustration of a radar system for centralized automated vital signs monitoring is shown in Fig. 1.1. For this configuration, ultra-wideband (UWB) radar technology [3] is an ideal candidate for implementation. UWB radar uses low power microwave radiation that is biologically safe for probing the vital signs. Microwaves can penetrate non-metallic surfaces, thus an under-bed (beneath the mattress) location for the radar system is also possible rather than the overhead scenario as depicted in Fig. 1.1. The UWB radar can discriminate multiple targets via time-of-arrival (ranging) methods. Therefore interference from neighboring radar units in the same proximity can be minimized or eliminated. In addition to breathing and heart beat rates monitoring, the UWB radar system can also monitor heart rate variability which can provide an advanced warning of impending heart failures.

The UWB radar vital signs monitor can be miniaturized and made portable to become a bedside device that can be conveniently placed to enable monitoring of sleep apnea, or used in senior homes where there is a higher risk of heart related conditions. When connected to the internet, the commercially deployed monitors can provide peace of mind to care givers of people with heart or breathing problems.

The above mentioned factors provide the motivation for a contactless real-time vital signs monitoring system to complement the status quo. The system has to be reliable and able to sense at distances of at least a few meters. Therefore it is the goal of this thesis to develop a robust centralized automated vital signs monitoring system that can monitor multiple patients in real-time.

The following section will describe the principles of UWB radar, explain the block diagram of the proposed work, and highlight the contributions that the work produced.

1.1 Principles of UWB radar

UWB systems are characterized by a wide frequency bandwidth and low radiated power spectral density. They operate by the exchange of short electromagnetic pulses between a transmitter and receiver [4]. The Federal Communications Commission (FCC) released regulations for UWB emission limits in 2002 [5] allowing UWB systems to radiate -41.3dBm/MHz in the frequency band of 3.1 to 10.6GHz. The low power emission limits the maximum range of UWB radars to less than 100m, however the wide bandwidth gives a typical range resolution of less than 30mm. UWB radar systems are compact in size, can easily be made portable and can operate using batteries [6].

UWB radar is essentially a pulse radar [7] with very wide bandwidth. Pulse-width in a radar system determines the range resolution. Range resolution of 30mm is typical for a pulse propagating in free-space occupying 10GHz zero-crossing bandwidth. The derivation of range resolution for a particular zero-crossing bandwidth is illustrated with an example as follows:

For a rectangular pulse of finite duration τ , the approximate zero-crossing bandwidth (energy within the main lobe of the double-sided power spectral density) is $2/\tau$, as shown in Fig. 1.2 for a 200ps zero-crossing pulse width. Other definition of bandwidth and pulse width for various pulse shapes will be detailed in the later part of this section.

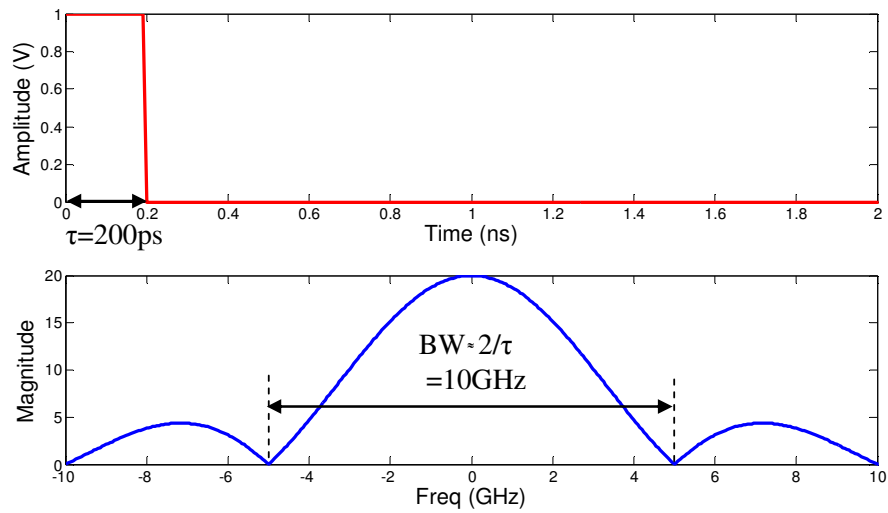


Fig. 1.2 - Bandwidth of a pulse of 200ps duration.

Moreover when the rectangular pulse of duration τ is used to time-gate a sinusoid with frequency of f_c , the spectrum will be shifted to f_c . The spectral plot of a 200ps time-gated 6.5GHz sinusoid in Fig. 1.3 verifies the prediction.

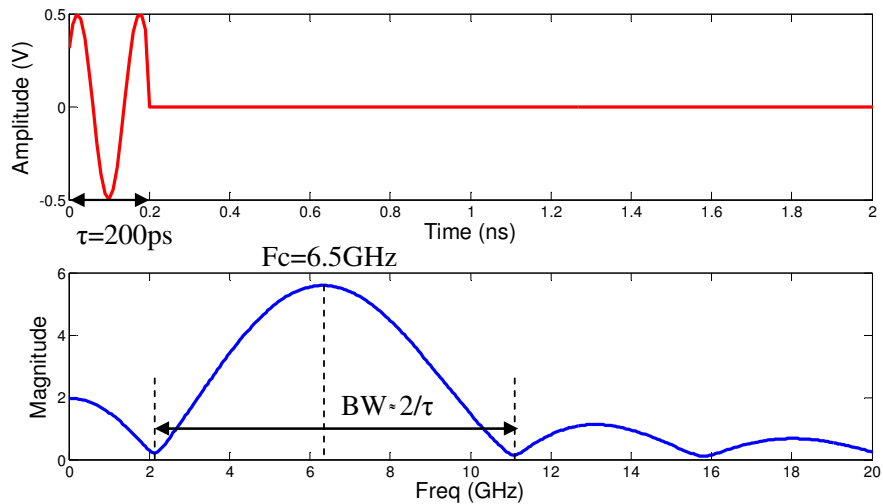


Fig. 1.3 - Bandwidth of time-gated 6.5GHz sinusoid with 200ps pulse duration.

Therefore in general, a rectangular pulse with τ duration will occupy an approximate zero-crossing bandwidth of $2/\tau$ and the pulse shape will determine its center frequency.

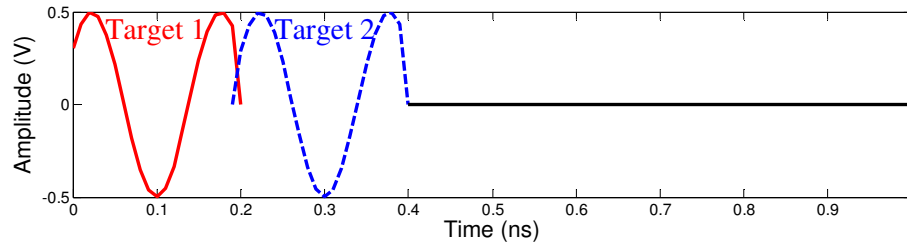


Fig. 1.4 - Non-aliased adjacent pulses at system range resolution.

Adjacent pulses can be distinctively identified if they do not overlap. Therefore at the radar receiver, non-aliased adjacent pulses determine the range resolution of the system. This is shown in Fig. 1.4. The red solid pulse is scattered from the nearer target and the blue dashed pulse is from a target located at the system range resolution distance away. Fig. 1.5 shows the physical description of targets placed at 1m distance away from the antennas, and their corresponding received signals (without distortion and amplitudes normalized) are displayed in Fig. 1.6. The dotted black line in Fig. 1.6 is the transmitted pulse that has been picked up at the receiver via coupling.

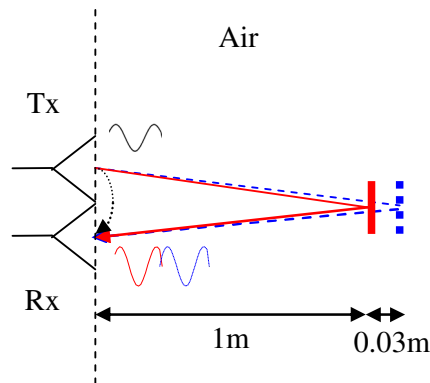


Fig. 1.5 - Example representation of UWB radar operating at system range resolution.

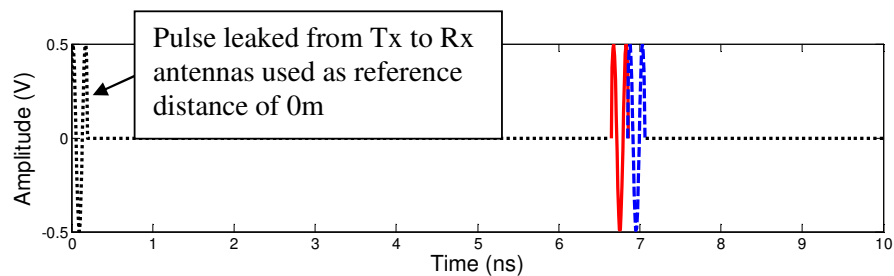


Fig. 1.6 - Received signals of example radar operating at system range resolution.

In free-space, the time taken to travel 2m (round trip distance for a target 1m away) is: $T = 2m/c = 6.67ns$ where c is the speed of wave propagation in air.

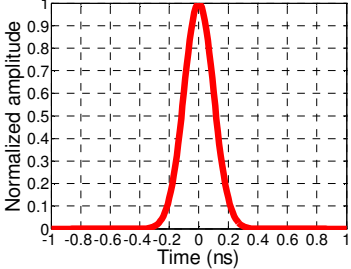
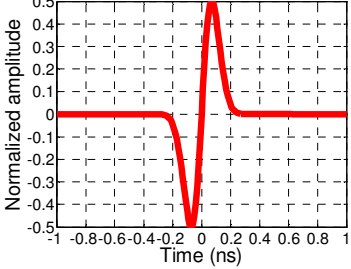
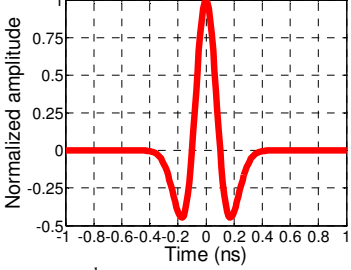
Therefore the received pulses for targets at 1m are delayed by 6.67ns from the transmitter (Tx) to receiver (Rx) leaked pulse. The leaked pulse is used as a reference for 0m distance.

For a 200ps delay between pulses such that they are non-overlapping (c.f. Fig. 1.4), distance travelled in free-space $D = c \times 200ps = 0.06m$. This is the round trip distance between targets for radars. Therefore the physical distance between the targets is 0.03m, which is the range resolution of the radar system for a pulse of 10GHz zero-crossing bandwidth. When a dielectric material of relative permittivity ϵ_r is between the targets, the range resolution will improve as the speed of propagation within the material will slow to $c/\sqrt{\epsilon_r}$.

In some literature, rather than a zero-crossing bandwidth, the 3dB bandwidth is described. When the 3dB bandwidth is defined for a rectangular pulse of duration τ (c.f. Fig. 1.2), the 3dB bandwidth will occupy an approximate bandwidth of $1/\tau$, as compared to $2/\tau$ when a zero-crossing bandwidth is used as shown previously. Therefore the 3dB bandwidth of the rectangular pulse with a 200ps zero-crossing pulse duration τ is ~5GHz. Also, some radar texts list the range resolution to be $c/(2 \times \text{bandwidth})$ where the definition of the bandwidth is mainly the 3dB bandwidth. Table 1.1 presents various Gaussian pulse shapes, full-width at half-maximum (FWHM) pulse widths, and their associated bandwidths according to the respective bandwidth definitions. For Gaussian pulses, the FWHM pulse width is often cited rather than the zero-crossing pulse width. The illustration through the example radar system above is visually easier to follow.

When a UWB system radiates any Gaussian shaped pulse through a medium via an antenna pair, the type of antenna used has an effect on the pulse shape transmitted and received. When the transmit antenna is of the aperture type, the radiated pulse will be a differentiated form of the input pulse; and when the receive antenna is of a bicone type, the pulse received will be an integral form of the radiated pulse [8]. The pulse shape analysis is important to develop an optimal receiver architecture design. Apart from the pulse shape and distortion analysis, the prediction of the received pulse power across the channel can provide for the link budget estimation in the system design. The power budget can be estimated using the antenna aperture dimensions together with its radiation efficiency to obtain its effective height, and the path loss parameter [9].

Table 1.1
Pulse width relation to bandwidths for various Gaussian pulses

Pulse type	FWHM Pulse width, τ	Zero-crossing bandwidth, $\approx 2/\tau$	3dB bandwidth, $\approx 1/\tau$
 <p>Gaussian pulse</p>	240ps	9GHz	3GHz
 <p>1st derivative Gaussian</p>	260ps	8GHz	2.5GHz
 <p>2nd derivative Gaussian</p>	400ps	6GHz	2GHz

A UWB radar's operation is governed by the radar range equation given as [3]:

$$R(s,t) \leq \sqrt[4]{\frac{EG(\theta, \phi, S, t)\sigma_{UWB}(t)A(\theta, \phi, S, t)}{(4\pi)^2 \rho q N_o}} \quad (1-1)$$

where R is the detectable range of the target, s is the received pulse shape, t is the time variable, E is the radiated pulse energy, G is the transmit antenna gain, σ_{UWB} is the radar cross section of the target, S is the pulse shape due to the impulse response of antenna, A is the receive antenna aperture effective cross section, ρ is the additional losses in the radar system, q is the threshold signal-to-noise ratio set for the radar system, and N_o is the spectral density of the noise at the receiver.

From the UWB radar range equation, it can be observed that the radar cross-section (RCS) of the target is time-varying. The RCS is dependent on the target's size, shape and material. Many targets are dispersive due to the frequency-dependent nature of their materials. For complex shaped targets, there will be bright spots that will scatter more energy than other parts. For example, the muscle tissues have a larger permittivity ($\epsilon_r \cong 50 @ 6.5\text{GHz}$) [10] and thickness (1.35cm) [11] beneath the skin and fat layers ($\epsilon_r \cong 5 @ 6.5\text{GHz}$; 0.96cm thickness) and will scatter more energy due to a larger ϵ_r contrast as the pulse propagates through the layers. When the bright spots are constantly moving and changing its shape due to breathing, the result will be a time-varying RCS that causes the target to suddenly fade, thus affecting the radar's reliability.

1.2 Contributions of this thesis

The research focuses on the fading RCS problem of moving/rotating targets. A target scatters energy in various directions and alters the polarization of the incident waves depending on the target's shape and material properties. The exploitation of circular polarization to reduce the polarization losses due to complex target scattering is a solution. The circular polarized UWB radar improves the robustness and accuracy for detecting and monitoring human targets due to reduced polarization losses from curvatures, orientation and movements of the human body.

The May 2013 issue of the IEEE Transactions on Microwave Theory and Techniques has a special emphasis on biomedical applications. This special issue contains the state-of-the-art in radar vital signs monitors and biological imaging systems. There are nine papers in this special issue that described implementations using both Doppler and impulse-based radar methods for sensing vital signs, integrated circuit forms of microwave board design as system implementation, system performance improvement for impulse radar by adopting clutter removal processing methods to reduce undesired signals from system jitter that resemble breathing signals, and a six-port receiver design for detecting life signs, including the work of this thesis proposing a circular polarization system design to improve robustness in vital signs monitoring. Fig. 1.7 outlines the block diagram of the circularly polarized UWB radar system developed in this thesis.

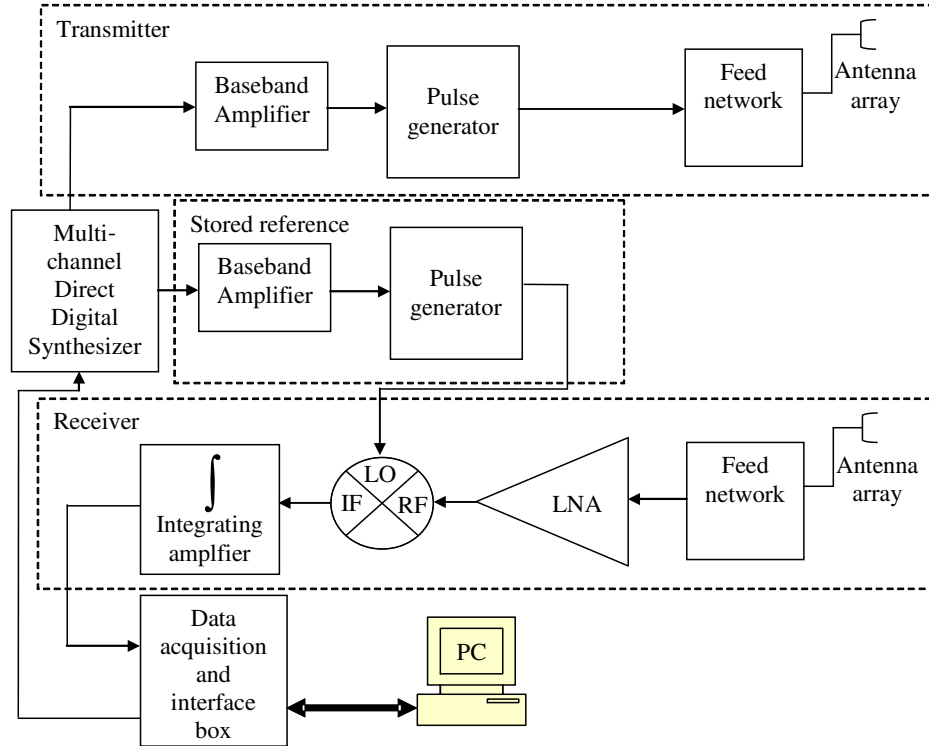


Fig. 1.7 - Block diagram of the proposed circularly polarized UWB radar system.

For this thesis, the critical components of the system have been developed and applications of the technology are demonstrated. The pulse generator is designed for low pulse repetition rate yielding high amplitudes with narrow pulse widths [12]. Tandem asymmetric tapered 180° hybrid couplers [13] cascaded with an optimized symmetric quadrature hybrid coupler form the decade bandwidth feed network design to feed an array of sequentially rotated antennas for circular polarized radiation. The circular polarized antenna system is characterized and achieved a decade bandwidth axial ratio which is the widest axial ratio bandwidth reported in literature [14]. The amplifiers, broadband mixer, direct digital synthesizer and data acquisition device are assembled using commercial off-the-shelf components. The system has been integrated and the software for breathing and heart beat rates detection is developed [15]. It is shown that the circular polarized radar is more robust in monitoring breathing and heart beat rates than a linear polarized system. A new method of multi-layered material characterization using time domain RCS measurement has been demonstrated [16].

The following chapter will introduce the design of the pulse generator, the starting component of the circularly polarized UWB radar system.

Chapter 2

Pulse generator

The pulse generator is the heart of a UWB radar system and it produces the narrow pulses to achieve the high resolution radar functionalities. Typical pulses used in UWB radar systems are the Gaussian pulse and its derivatives [17]. The most common way to generate such pulses is by the introduction of non-linear devices to a sinusoidal source. Harmonics of the source frequency will be generated from the nonlinearity of the circuitry that is realized using passive or active devices. The choice of implementation is determined by the specifications of the UWB pulses, such as the pulse peak voltage, pulse width and pulse repetition frequency.

2.1 Types of pulse generator

The use of CMOS devices, which are very fast acting switches, yields an almost ideal non-linear response that can generate narrow pulses. When the CMOS devices are combined with cascaded stages of inverter gates in a series configuration to tune the overall propagation delay, the pulse-widths can be controlled [18]. Full-width at half-maximum (FWHM) pulse-width in the order of 50ps is possible with state-of-the-art CMOS circuits [19]. However the operating voltages of these circuits are $\sim 1V$ due to nanometer scale gate dimensions, therefore limiting the amplitude of the output pulses.

Avalanche transistor based pulse generators have been reported to generate 1ns to 100ps FWHM pulse-widths with amplitudes of 15 to 1100V [20-21]. However these designs are only for very low repetition rates of up to 200kHz. FET transistors are usually used for pulse compression and step ramp sharpening [22-23] to achieve 30 to 300ps FWHM pulse-widths at 2V amplitude. The design complexity of the pulse generators designed with active components is high. Transistors require external power sources, biasing and have the possibility of oscillation through coupling.

Diodes are the most common passive non-linear devices. Step-recovery diodes (SRD), tunnel, and avalanche diodes are typically used for pulse generation [24]. The transition time of a diode which corresponds to the degree of non-linearity, determines

Portions of this chapter have been published in reference [12]

the pulse-width when the diode is used as a generator. The faster the transition time, the more non-linear is the diode and a narrower pulse-width will be generated [25]. A FWHM pulse-width of 100ps at 15V peak amplitude is possible with the SRD pulse generator. The maximum output voltage of the SRD is limited by its reverse breakdown voltage, which is at least 15V.

Alternatively, non-linear transmission lines (NLTL) are found to generate shock waves that have pico-second rise/fall times. NLTLs can be used for generating pulses of less than 10ps FWHM pulse-width at peak-to-peak voltages of 3 to 7V [26-27]. However they are packaged in microwave integrated circuits (MICs). They are suited more for MIC designs.

Table 2.1 summarizes the capabilities of various pulse generators.

Table 2.1
Types of pulse generators

Type	Step/Pulse	FWHM pulse width/rise time@Amplitude	Notes
CMOS [19]	Pulse	250ps@1.4V	
Avalanche transistor [21]	Pulse	1.3ns@1kV	Max. 200kHz rep. rate
FET [23]	Pulse	30ps@1V	
SRD [22]	Pulse	140ps@1V	
Avalanche diode [24]	Pulse	400ps@125V	GHz rep. rate
NLTL [27]	Step	2ps@5V	Fastest transition time, MIC

From the available methods of generating pulses, for UWB radar applications, the SRD is the most suitable due to the better than 100ps transition time and greater than 15V breakdown voltage. For such a performance, the SRD can potentially generate up to 15V pulses with FWHM pulse-widths of ~200ps.

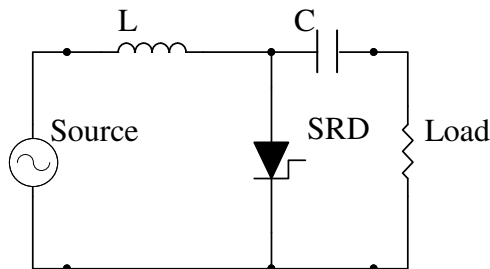


Fig. 2.1 - Schematic diagram of the shunt mode SRD harmonic generator.

Gaussian mono-pulses (impulses) are generated using the shunt mode SRD harmonic generators [28]. The schematic of the shunt mode SRD pulse generator is shown in Fig. 2.1. In the positive half cycle, the SRD stores charge across the intrinsic region between its junctions. As the input changes its polarity in the negative half cycle, the stored minority charges will recombine. For the duration of the recombination which is proportional to the diode's life-time, the diode will remain in forward bias. When all the stored charges are removed, the diode will change to the reversed biased state in an instant according to its transition time [29]. Fig. 2.2 gives an illustration of the finite stored charge highlighted by the shaded red area during the conducting period of the diode, and minority carrier recombining during the time when the input voltage falls below the diode's contact voltage (shaded red area in the negative half cycle). When all the stored charges are recombined, the diode stops conducting shown by the sudden drop to the input voltage. The snap can be differentiated by a series capacitor as shown in Fig. 2.1 to form the Gaussian impulse train.

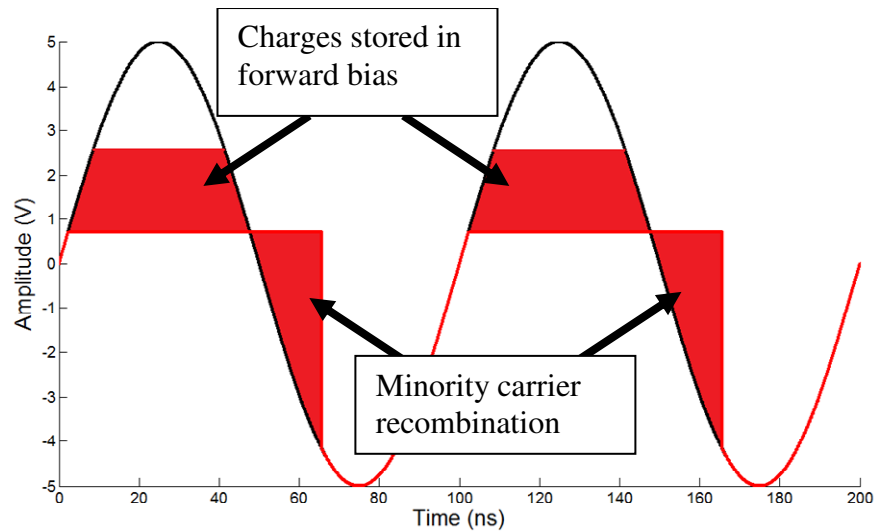


Fig. 2.2 - Charge storage and minority carrier recombination with respect to input voltage (input is black line, output is red line; shaded areas are stored charges).

2.2 Limitations of the shunt mode step recovery diode pulse generator

To achieve a UWB radar range of 15 meters, the pulse repetition frequency (PRF) should be 10MHz or lower to prevent range ambiguity [7]. The range resolution of 15mm of the UWB radar system requires 200ps FWHM pulse widths. The goal of the UWB radar is to have further range with good resolution. To meet this goal, the PRF will typically be below 10MHz and pulse-width ~200ps.

For a SRD to generate high amplitude pulses, it is recommended to use a diode that has a lifetime greater than 10 times of the pulse repetition period (PRT) [25]. At a low PRF of 10MHz, the typical SRD with the recommended lifetime has a transition time in the order of 240ps. This will result in ~500ps pulse width. To generate 200ps impulses, the SRD capable of such a specification has a typical life-time of 15ns which is about 67 times less than the recommended. The consequence of using this SRD at low PRF is that the diode changes impedance at a time when the reverse current is far from the maximum level, thus achieving only a fraction of the maximum capable voltage.

The life-time of the diode determines the amount of charge it can store during the conduction stage (forward-biased phase) [29]. The total charge stored in the positive cycle is

$$Q = I_f \tau_L \left(1 - e^{-T_f / \tau_L}\right) \quad (2-1)$$

where I_f is the forward current, τ_L is the diode lifetime and T_f is the period of forward conduction. For a short lifetime diode, this limits the amount of charges it can store.

The time taken for the diode's minority carriers to recombine its stored charges is

$$T_s = \tau_L \ln \left(1 + \frac{Q}{I_r \tau_L}\right) \quad (2-2)$$

where I_r is the reverse current. The recombination time of the stored charges is a fraction of the lifetime of the diode. At low PRFs where the period of the input signal is multiple times of the diode lifetime, this will create only a small voltage snap as the time when all the stored charges are recombined is not far from the start of the reverse bias half period.

Longer lifetime diodes have a larger junction capacitance. Consequently, the transition time for the diode will be longer. The relationship between the junction capacitance, C_v , and junction area, A_d , is given by

$$C_v = \frac{\epsilon A_d}{d} \quad (2-3)$$

where d is the distance between the conducting plates of area A_d with a substrate of ϵ permittivity.

The transition time, T_t , of the diode is related to A_d by

$$T_t = G_q A_d^{-2/3} + G_{RLC} A_d \quad (2-4)$$

where G_q is the impedance transition time and G_{RLC} is the residual charge transmission time. It can be seen that T_t is proportional to A_d and therefore also proportional to C_v .

From the above discussion, the ideal SRD for our application will be the one that has a long life-time and short transition time to generate a high amplitude pulse with small pulse width at low PRF. Since such a SRD does not exist, we propose a novel design using the combination of a long life-time SRD together with a fast transition SRD to achieve a high voltage pulse with small pulse width.

2.3 The cascaded shunt mode step recovery diode pulse generator

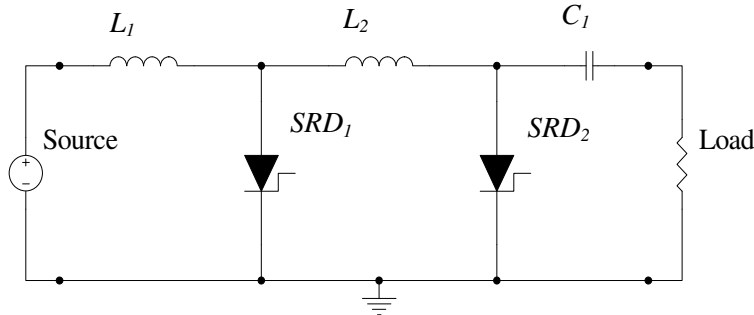


Fig. 2.3 - Schematic diagram of the proposed UWB radar pulse generator.

As capacitances (charge storage) add in shunt, a long life-time SRD placed near the source can be cascaded in shunt to a fast transition SRD placed near the load. The schematic diagram of such an arrangement has been shown in Fig. 2.3, with SRD_1 being the diode with a long life-time and SRD_2 being the diode with fast transition time. When the charges stored in SRD_1 is depleted during the negative half cycle and rapidly changes its impedance from low to high, SRD_2 will then start to discharge its stored charges. This will make SRD_2 as though it has an equivalent life-time of SRD_1 and SRD_2 combined.

Thus when SRD_2 depletes its charges, the reverse current through it will be closer to the maximum. Hence as SRD_2 changes impedance from low to high, the voltage transient produced will be in the order of SRD_2 's transition time, but with a voltage output that is equivalent to what SRD_1 can produce for the given PRF.

The design starts with the specification of the system pulse width that determines the selection of SRD_2 . Pulse widths of each stage are, at minimum, twice the transition time of the respective SRD. SRD_1 is then chosen, to have a longer carrier lifetime than SRD_2 . Equation (2-5) shows the relation between pulse width and inductor value L in a single stage shunt-mode harmonic generator [25] (c.f. Fig. 2.1). C_d is the reverse bias capacitance of the respective SRD. Values of L_1 and L_2 in Fig. 2.3 are determined by

$$\text{Pulse-width} = \pi\sqrt{LC_d} \quad (2-5)$$

For UWB applications with 6.5GHz center frequency, the required system FWHM pulse width, τ_s , is 200ps. For $\tau_s=200$ ps, SRD_2 (M-Pulse MP4023) is chosen with a transition time of 50ps. The reverse bias capacitance of SRD_2 is 0.35pF and the calculated L_2 is 12nH. SRD_1 (M-Pulse MP4043) is chosen, as discussed later, for a carrier lifetime that is four times of SRD_2 . It has a transition time of 120ps and reverse bias capacitance of 1.5pF. For an expected pulse width of 240ps, $L_1=3.9$ nH.

C_1 and the load form a first order high-pass filter. C_1 is determined by the pulse width that sets the high-pass filter cut-off frequency. The time constant of the circuit is the combination of C_1 and the load. Pulse width of the system is equivalent to time constant of the circuit.

$$\text{Time constant} = R_L C \quad (2-6)$$

For a 200ps pulse width and 50Ω load (R_L), C_1 is 4pF.

The initial design obtained above is then optimized to achieve higher output pulse amplitude and narrower pulse width by practically tuning L_1 , L_2 and C_1 values using commercially available components and changing SRD_1 . The optimization procedure and results are described in the following Sections 2.4 and 2.5. The approach to optimization is through a sensitivity analysis of the circuit component values. Simulation is used to confirm the performance of the optimized circuit. During the manual optimization, it is observed that the output pulse amplitude is sensitive to the value of L_1 and carrier lifetime of SRD_1 ; while output pulse width is sensitive to the values of L_2 and C_1 . Pulse ringing can be controlled by careful selection of L_1 and L_2 values.

2.4 Optimization for pulse amplitude

Increasing L_1 value results in higher output pulse amplitudes and ringing. Fig. 2.4 shows the effect of L_1 on the output pulse amplitude ($L_2=12\text{nH}$, $C_1=3.9\text{pF}$). Thus L_1 will be raised until an acceptable level of ringing is reached for the optimum value. The output voltage, $V(t)$, of the single stage shunt-mode pulse generator can be determined from [28],

$$V(t) = -I_o \sqrt{\frac{L/C}{1-\zeta^2}} \exp\left(-\sqrt{\frac{\zeta^2}{1-\zeta^2}} \beta t\right) \cdot \sin(\beta t) \quad (2-7)$$

where I_o is the initial current in the inductor during the “snap”, and $\beta = \sqrt{1-\zeta^2} / \sqrt{LC}$ and $\zeta = \sqrt{L/C} / (2R_L)$. Equation (2-7) explains the effect of L_1 on pulse amplitude. An increase in L value, as shown in (2-7), increases the amplitude of $V(t)$, and increases the damping factor but lengthens the pulse envelope. The pulse width is relatively unchanged. Therefore, L_1 is dominant in the effects of the coefficient and the exponential terms of equation (2-7).

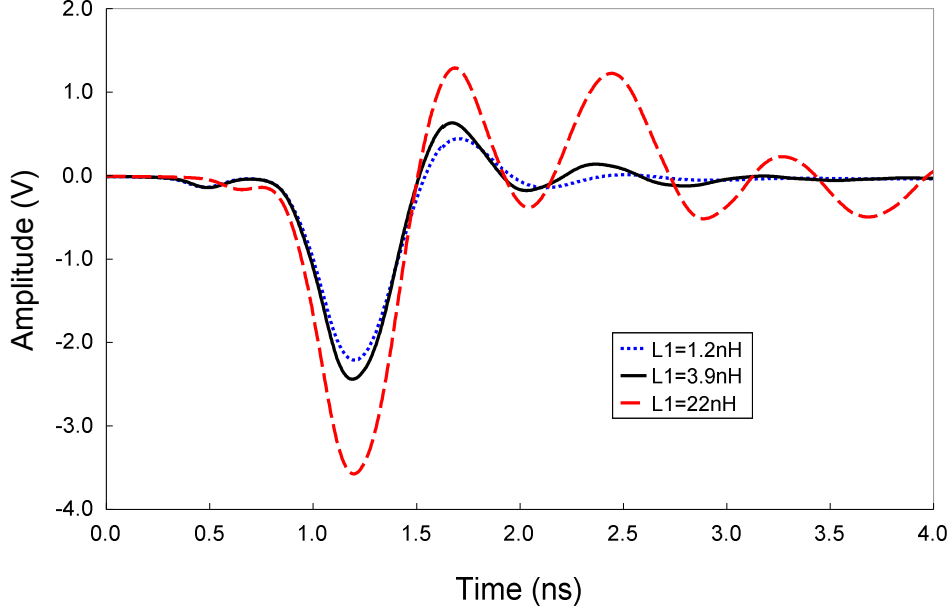


Fig. 2.4 - Effect of L_1 on output pulse ($L_2=12\text{nH}$, $C_1=3.9\text{pF}$, $V_{in}=10\text{V CW}$).

Fig. 2.5 shows the effects of changing SRD_1 . The lifetimes for the SRDs are 15ns, 30ns, 60ns and 120ns for the MP4023, MP4033, MP4043 and MP4063 respectively. Measured pulse widths are larger for longer lifetime SRDs due to the leakage of SRD_1 .

response. The amplitude is highest for SRD_1 having a lifetime that is two times of SRD_2 . Therefore the choice for SRD_1 will be one that has a carrier lifetime longer than that of SRD_2 . However, a larger difference between the lifetimes of SRD_1 and SRD_2 will reduce the output pulse amplitude for a given system pulse width. SRD_1 should have a lifetime of at least twice that of SRD_2 .

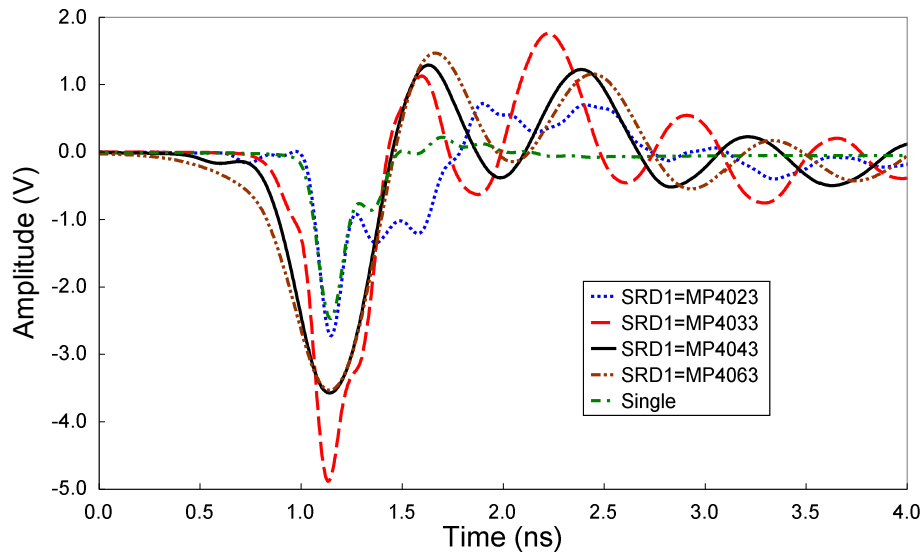


Fig. 2.5 - Effect of SRD_1 on output pulse ($L_1=22\text{nH}$, $L_2=12\text{nH}$, $C_1=3.9\text{pF}$, $V_{in}=10\text{V CW}$).

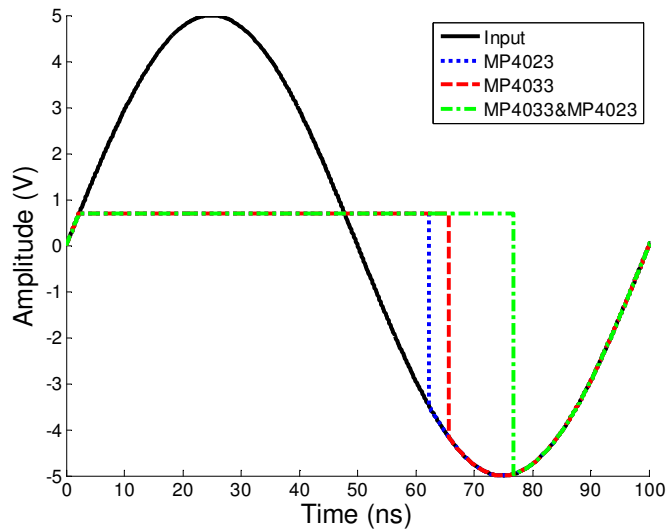


Fig. 2.6 - Simulation to compare single and cascaded stages.

To illustrate the effects of diode lifetime and the resulting output voltage at a low pulse repetition rate, a simulation is carried out using a single MP4023 shunt mode stage,

compared with a single MP4033 shunt mode stage and a design with MP4043 stage cascaded with a MP4023 stage. The input is a 10V continuous wave (CW) sinusoid at 10MHz PRF. All circuits are without C_I , thus only a step is observed. Fig. 2.6 shows the result of the simulation.

For the MP4023 single stage design, the output voltage is around -3.5V peak due to its limited charge storage capacity. The “snap”, transition, from the 0.7V contact potential to -3.5V peak step happens quickly within 50ps. However the MP4033 has a larger charge storage capacity and its resulting output voltage reaches about -4.2V peak. The transition is slower at 70ps though, thus it will generate 140ps impulses at minimum. The proposed cascaded design output voltage is -5V peak (at the maximum peak) due to the combined charge storage of the two diodes, and its transition time is still 50ps due to the last stage being the MP4023.

2.5 Optimization for pulse width

Reducing the value of L_2 shortens the pulse width. The amplitude is relatively constant, and observed to have some correlation to the damping factor. L_2 is dominant in the sine term of equation (2-7). Fig. 2.7 shows that shortest pulse width is obtained for $L_2=1.2\text{nH}$ at $L_I=3.9\text{nH}$ and $C_I=3.9\text{pF}$. Minimizing L_2 will minimize pulse width.

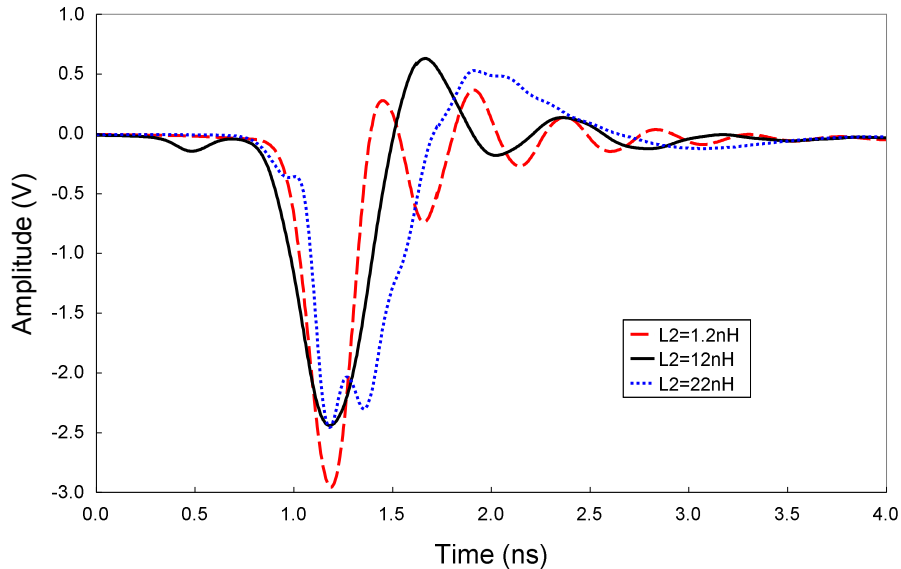


Fig. 2.7 - Effect of L_2 on output pulse ($L_I=3.9\text{nH}$, $C_I=3.9\text{pF}$, $V_{in}=10\text{V CW}$).

Referring to Fig. 2.3, C_I and load forms a first order high-pass filter. Reducing C_I shortens the output pulse width at the expense of pulse amplitude.

2.6 Performance of the optimized pulse generator

A prototype of the proposed pulse generator has been built using Rogers RO4003C™ substrate ($\epsilon_r=3.38$, $h=0.8\text{mm}$). M-Pulse Microwave MP4033 is used as SRD_1 and MP4023 as SRD_2 . L_1 and L_2 are 10% tolerance multilayer ceramic chip inductors with values of 22nH and 1.2nH respectively. A 3.9pF porcelain multilayer chip capacitor is used as C_1 . The choice for these components is for an optimized pulse with trade-off among the amplitude, pulse width and ringing considerations. Fig. 2.8 shows a photograph of the prototype housed in a metallic chassis. The dimensions of the prototype board are 25mm x 25mm.

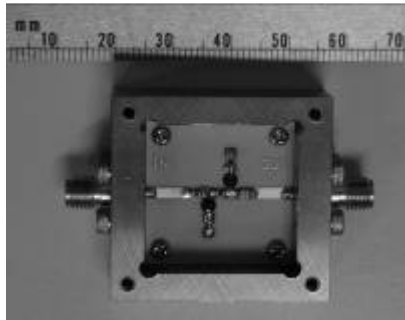


Fig. 2.8 - Photograph of the UWB radar pulse generator prototype.

The following results show that the proposed two stage pulse generator managed to generate pulses of higher pulse amplitudes (127% increase) as compared to the single stage shunt mode pulse generator, at the expense of longer pulse widths (51.5% increase). Voltage transfer efficiency (output voltage/input voltage) has improved to 56% from 25%.

Fig. 2.9 shows the output of the proposed pulse generator for a 10V peak-to-peak CW input at 10MHz PRF. It is compared with the output of the single stage shunt mode pulse generator designed using fast transition time SRD (MP4023) based on the design method outlined in [25], with $L=12\text{nH}$ and $C=2\text{pF}$. The measured outputs in Fig. 2.9 are in solid (black) and dashed (red), and simulated outputs in dot (blue) and dash-dot (brown). The simulation software used is Ansoft Designer from Ansys, with the Nexxim circuit transient simulator and non-linear microwave diode models. The measured pulse amplitude of single stage circuit (dashed line) is 2.47V and FWHM pulse width is 159ps. For the same input, the proposed pulse generator (solid line) produces a pulse of 5.6V amplitude and FWHM pulse width of 241ps. It should be noted that the current in the

inductor before the “snap” is 115mA. Simulation results predicted comparable pulse widths, amplitudes and ringing levels with the measurements. The inter-pulse ringing is a result of the choice of inductor L_2 that produces it. The simulator does not show the inter-pulse ringing due to the limited number of harmonics applied for it to converge.

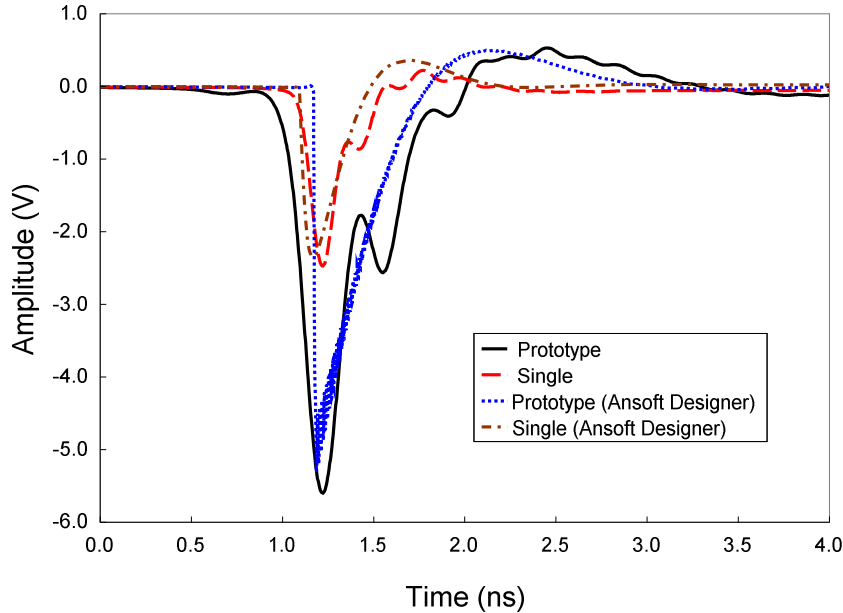


Fig. 2.9 - Outputs of prototype compared with single stage design for 10MHz CW input.

Higher amplitude ringing has been observed for the proposed pulse generator as compared to the MP4023 based single stage pulse generator. The pulses will be differentiated when radiated from the transmit antenna [8] and pulse ringing is inevitable due to the band-limited frequency response of filters, amplifiers and antennas. However, the system’s range resolution can be preserved in the presence of ringing with the use of pulse shaping filters or differentiators together with a correlation based receiver architecture.

In the second measurement, the pulse generators are fed with 10MHz PRF square wave input with 5V peak-to-peak amplitude and rise/fall time of ~4ns. The measured and simulated pulse generator outputs are shown in Fig. 2.10. For the single stage pulse generator, the measured pulse amplitude is 2.54V and FWHM pulse width is 159ps. For the proposed pulse generator, the pulse amplitude is 3.67V and FWHM pulse width is 211ps. The current in the inductor before “snap” is 75mA. The predicted amplitudes for the simulator are slightly more than the measured due to sharp rise/fall times of 0ns for the square wave generator. Pulse widths and ringing levels are predicted quite accurately in the simulations. Voltage transfer efficiency has improved from 51% to 73%.

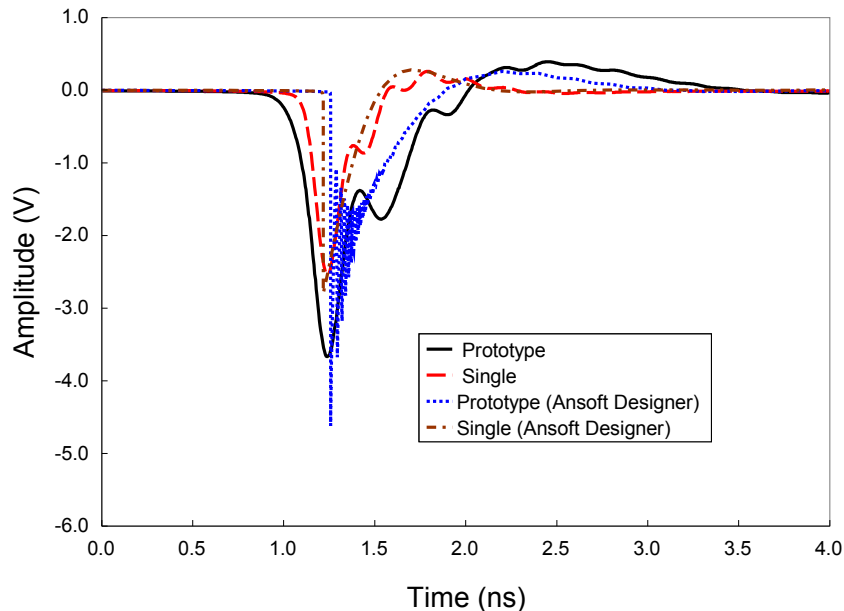


Fig. 2.10 - Output of prototype compared with single stage design for square wave input.

The main advantage of using the proposed design in the system is that the complexities of dealing with high frequency and broadband signals are reduced. The output voltage levels are high enough to be conveniently filtered or differentiated (to achieve other forms of Gaussian pulses) and transmitted without further amplification. Furthermore, the cost and considerations for low frequency narrow band amplifiers are much less than microwave broadband amplifiers. Broadband impedance matching at RF frequencies is always a challenge.

The proposed pulse generator demonstrates higher voltage than the active circuit designs reported in the literature.

The next chapter will explain how the generated narrow pulses can be made to radiate as circularly polarized UWB pulses. The high amplitude pulses from the proposed pulse generator design are able to drive the antenna array directly.

Chapter 3

Decade bandwidth circularly polarized antenna array

Circularly polarized wireless systems have been mainly used in space-borne deployments such as the Global Positioning System (GPS) [30], Satellite Communications (SatCom) [31] and Digital Radio Broadcasting (SDARS) [32] applications to mitigate the Faraday rotation of electromagnetic waves as they penetrate the Ionosphere. However, the adoption of circular polarization (CP) in Radio Frequency Identification (RFID) readers [33] and next generation wireless communication systems [34-35] are becoming prevalent due to the benefits of robustness to receiver orientation and fading. The potential benefits of CP are greater for high resolution ground penetrating radar [36] and material characterization [37] applications because of the ability to receive the reflected waves from multiple scatterers regardless of the orientation and nature of the objects. Modern radar imaging systems have very broad 10dB-return loss bandwidths in the order of multi-octave to even decade bandwidths to provide for a fine range resolution. i.e. a 7.5GHz bandwidth radar can provide a resolution of 5mm [37]. The design of a CP ultra-wideband (UWB) antenna of decade bandwidth that can support the modern pulse based radar applications is not available in the literature.

Various CP UWB antennas are implemented in slot [38-39], patch [40] and spiral [41-42] designs. The slot and patch technologies exhibit limitations in terms of 10dB return loss (RL) and 3dB axial ratio (AR) bandwidths, due to the limited bandwidths of the radiating elements and/or feeding mechanism. Reported AR bandwidths of the slot and patch designs are at most 77% [40]. The spiral antennas are frequency independent structures, thus are inherently wideband. However they are balanced antenna structures, and require equally wideband baluns to mate with the antennas. Furthermore, it is commonly known that spiral antennas are dispersive and will distort the pulse [43] during transmission and reception. The spiral designs [41-42] that have lesser dispersion, which is useful for pulse propagation, also suffer from less than a decade bandwidth.

Portions of this chapter is published in references [8, 13-14]

The proposed decade bandwidth CP antenna array design is achieved through the use of a feed network that is capable of a decade bandwidth performance. The feed network splits an input signal into four output signals with equal magnitudes but with phases of 0° , 90° , 180° and 270° over the band. The outputs of the feed network are fed to an array of four identical anti-podal Vivaldi antenna elements [44], which are sequentially rotated by 90° to radiate CP signal. The proposed decade bandwidth CP antenna array is suited for applications in high resolution microwave imaging systems.

A schematic diagram of the feed network is shown in Fig. 3.1. The splitting of the input signal into four equal amplitude signals of orthogonal phases is achieved through the cascade of a system of 90° and 180° 3dB hybrid couplers. The individual 3dB hybrid couplers are themselves novel designs to achieve the decade bandwidth performance and uniform propagation delay across the band. The following sub-sections describe the designs of the individual 3dB hybrid couplers.

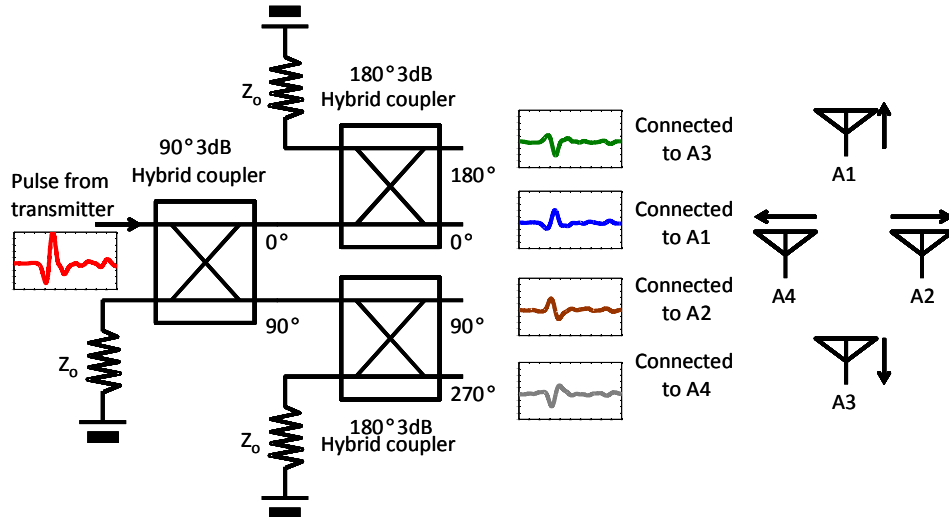


Fig. 3.1 - Schematic of UWB CP radar antenna feed network.

3.1 180° hybrid coupler

Hybrid couplers are generally 3dB directional couplers with specific phase relation between the outputs. If the phase difference is 90° then the hybrid is called quadrature or 90° hybrid, if it is 180° then that hybrid is called 180° hybrid and if the phase difference is 0° then it is called Wilkinson power divider [45]. Generally hybrids are four port networks with one port as an isolated port, but the Wilkinson power divider is a three port network and its fourth port is imbedded.

3.1.1 Types of 180° hybrid coupler

Conventional design of a hybrid is the rat-race ring hybrid [46] where bandwidths are narrow (below 30%), limited by the $3\lambda/4$ section. Improved design of the rat-race using a phase inverting $\lambda/4$ section to replace the $3\lambda/4$ [47-48] reduced its size by 75% and increased bandwidth to 90%. Various forms of microstrip to slotline transitions achieving reverse phase coupling and variations thereof [50-52] can achieve bandwidths of up to 114%. Limitations for bandwidths are mainly due to coupling capability of the structures to obtain a physically realizable design. The broadside coupled striplines provide unparalleled coupling, therefore yielding bandwidths beyond a decade (>164%) up to the limitations of the realizable widths and insertion losses as reported by [53].

3.1.2 The asymmetric tapered 8.34dB 180° hybrid coupler

Fig. 3.2 shows the schematic of a tapered coupled line 180° hybrid. This hybrid is also referred to as an asymmetric tapered coupled line coupler [46].

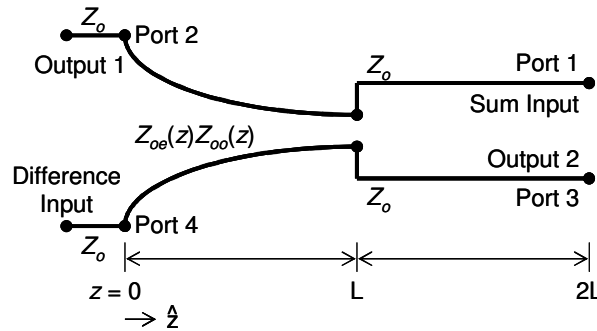


Fig. 3.2 - Schematic of tapered coupled line hybrid.

The coupler consists of two coupled lines with tapering characteristic impedance over the length $0 < z < L$. At $z = 0$ the lines are very weakly coupled so that the even and odd mode impedances are equal to the characteristic impedance of the line Z_o . While at $z = L$, the coupling is such that even mode impedance becomes Z_o/k , and odd mode impedance $Z_o k$. k is the coupling factor, which ranges from 0 to 1. The scattering parameters of an ideal tapered coupled line hybrid have been derived in [46] by using even and odd mode analysis. In this analysis the ideal conditions, like perfect impedance match between the sections at $z = 0$ and $z = L$, and very strong coupling at $z = L$ to zero

coupling immediately after $z = L$, are assumed, which are almost impossible to achieve in practical circuits.

Let the incident voltage of amplitude V be applied to port 4, the difference input (c.f. Fig. 3.2). The scattering parameter can be written as,

$$S_{44} = 0 \quad (3-1)$$

$$S_{24} = \frac{k-1}{k+1} e^{-j2\theta} \quad (3-2)$$

$$S_{34} = \frac{2\sqrt{k}}{1+k} e^{-j2\theta} \quad (3-3)$$

$$S_{14} = 0 \quad (3-4)$$

where $\theta = \beta L$. The level of isolation (S_{14}) of the hybrid coupler is one of the important parameter to be achieved. Ideally the isolation should be infinite, however in practical circuits isolation will degrade due to non-uniform transmission coefficients of even and odd modes.

The other primary reasons for poor isolation are coupling between the lines, where coupling should be zero i.e. immediately after tight coupling ($z > L+$) and fringe capacitance between the lines. One of the ways of reducing the coupling between the lines is to separate them at an acute angle with respect to each other at the transition. The bending of the lines will reduce the magnetic coupling more than electric coupling, which causes the odd mode velocity of propagation to be less than that of the even mode in the transition region. This is due to the accumulated charges at the corners of the right angled bend. Therefore, isolation in practical hybrid circuit will differ more compared to other parameters from the ideal case. The magnitude of isolation for non-ideal hybrid can be represented by

$$|S_{14}| = \frac{\sqrt{k}}{1+k} (1 - \cos \delta\theta) \quad (3-5)$$

where $\delta\theta$ is the phase difference between even/odd transmission coefficients. The scattering parameters (3-2), (3-3) show that the coupling depends on the value of k , and bandwidth depends on the matching of tapered lines. If the value of k is low, i.e. amount of mismatch at the transition (between coupled lines and uncoupled lines) is high, the reflected signal is high, and therefore coupling level is high. The variation of coupling, with respect to frequency, depends on how well the reflected signal reaches the coupled port. In ideal case, the entire reflected signal from the transition point reaches the coupled

port at all frequencies. However, in practical circuits it is not possible to match the circuit for the entire frequency band without fluctuations in reflection coefficient. One of the possible approaches for broadband matching is the use of Klopfenstein tapered coupled lines [54].

The coupling factor k can be calculated for the required coupling from (3-2).

$$k = \frac{1 - |S_{24}|}{1 + |S_{24}|} \quad (3-6)$$

The value of k (coupling parameter at transition point) will be realized through a coupling section, whose coupling coefficient at the point of transition is

$$C = \frac{1 - k^2}{1 + k^2} \quad (3-7)$$

If the coupling level ($|S_{24}|$) is high, the value of C will be close to 1, which is not possible to realize in strip or microstrip technology. The only possible solution to the problem of achieving a design with specified maximum coupling coefficient is to split the coupling into stages, and then to realize the required network for each stage [55].

3.1.3 3dB 180° hybrid coupler

Tight coupling can be achieved by connecting two couplers of weak coupling in tandem. Fig. 3.3 shows the tandem connection of two hybrid couplers.

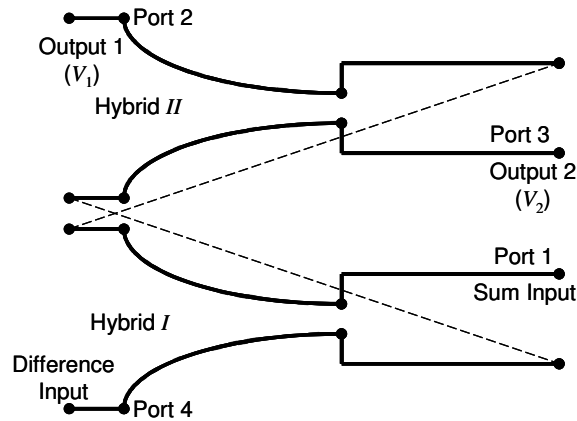


Fig. 3.3 - Tandem connection of two hybrid couplers.

The output voltages V_1 , V_2 at ports 2 and 3 respectively can be written in terms of scattering parameters of individual hybrids (c.f. Fig. 3.2 and 3.3).

$$V_1 = S_{34}^I S_{24}^{II} + S_{24}^I S_{21}^{II} \quad (3-8)$$

$$V_2 = S_{34}^I S_{34}^{II} + S_{24}^I S_{31}^{II} \quad (3-9)$$

where S_{mn}^I and S_{mn}^{II} are the S-parameters for ports m and n of hybrids I and II respectively.

By expanding (3-8) and (3-9), V_1 and V_2 can be written in terms of k_1 and k_2 .

$$V_1 = \frac{-2\left((1-k_2)\sqrt{k_1} + (1-k_1)\sqrt{k_2}\right)}{(1+k_1)(1+k_2)} \quad (3-10)$$

$$V_2 = \frac{4\sqrt{k_1 k_2} - (1-k_1)(1-k_2)}{(1+k_1)(1+k_2)} \quad (3-11)$$

It can be easily shown that $V_1^2 + V_2^2 = 1$. The values of k_1 and k_2 can be calculated for required power division between the output ports. The design can be simplified by assuming similar hybrids i.e. $k_1 = k_2 = k$, then V_1 and V_2 will be

$$V_1 = -4\left[(1-k)\sqrt{k}\right]/(1+k)^2 \quad (3-12)$$

$$V_2 = \left[4k - (1-k)^2\right]/(1+k)^2 \quad (3-13)$$

Let V_2 , be given as design parameter. Then k can be calculated from (3-13) where the solution is quadratic, and the value of k should be between zero and one. Hence the valid solution will be

$$k = \frac{3 - V_2 - 2\sqrt{2}\left(\sqrt{(1-V_2)}\right)}{V_2 + 1} \quad (3-14)$$

The hybrid coupler can be designed for uniform or non uniform power division between the output ports. The total coupling due to the individual hybrid is

$$C_T = 20 \log\left(\frac{1-k}{1+k}\right) \text{ dB} \quad (3-15)$$

For a 8.34dB hybrid, the impedance transformation ratio k is 0.446 [53]. Across the taper, the even mode impedance will be transformed from $Z_{oe}=Z_{oo}=Z_o=50\Omega$ to $Z_{oe}=Z_o/k=112\Omega$ and the odd mode to $Z_{oo}=kZ_o=22.3\Omega$, where Z_o is the characteristic impedance of the striplines at all the ports. Return loss at the input and output ports will remain matched as long as $Z_o = \sqrt{Z_{oe} Z_{oo}}$ along the length of the taper. A Klopfenstein taper is used for the impedance transformation, and the resulting even and odd impedances along the length x with total length l of the taper can be determined by [54]

$$Z_{oe}(x) = \frac{Z_o}{\sqrt{k}} \exp \left\{ \frac{\rho_o}{\cosh(A)} \left[A^2 \varphi \left(\frac{2x}{l}, A \right) + U \left(x - \frac{l}{2} \right) + U \left(x + \frac{l}{2} \right) \right] \right\}, |x| \leq \frac{l}{2} \quad (3-16)$$

$$Z_{oo}(x) = Z_o \sqrt{k} \exp \left\{ \frac{-\rho_o}{\cosh(A)} \left[A^2 \varphi \left(\frac{2x}{l}, A \right) + U \left(x - \frac{l}{2} \right) + U \left(x + \frac{l}{2} \right) \right] \right\}, |x| \leq \frac{l}{2} \quad (3-17)$$

where $\rho_o = (1-k)/(1+k) = 0.383$ is the zero frequency reflection coefficient of the even mode, $A = \beta l$ for $\beta = 2\pi/\lambda_m$ and λ_m is the wavelength of the lowest (cut-off) operating frequency of the coupler, $U(z)$ is the unit step function at position z , and φ is a function given by

$$\varphi(z, A) = -\varphi(-z, A) = \int_0^z \frac{I_1(A\sqrt{1-y^2})}{A\sqrt{1-y^2}} dy, |z| \leq 1 \quad (3-18)$$

I_1 is the modified first order Bessel function of the first kind.

The length l of the coupler is determined when the maximum passband ripple ρ_{om} and lower cut-off frequency of the design is set. For a passband ripple of 0.01 (i.e. 20dB return loss) and cut-off frequency of 1GHz ($\lambda_m = 163mm$), the length l can be obtained from

$$l = \frac{\lambda_m \cosh^{-1}(\rho_o/\rho_{om})}{2\pi} \quad (3-19)$$

The calculated l for the prototype design is 112mm.

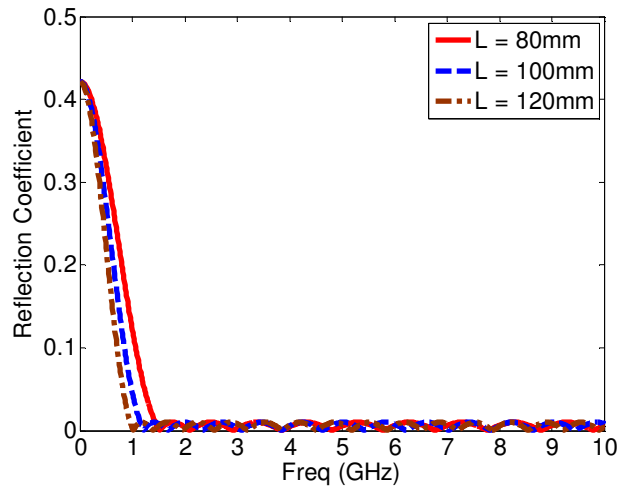


Fig. 3.4 - Reflection coefficient of the coupled lines for various lengths.

Fig. 3.4 shows the variation of reflection coefficient of the coupled lines with respect to frequency for a maximum ripple of 0.01 in the pass band. The length of the coupled line can be reduced with increase in reflection coefficient. The reflection coefficient shows a high-pass behavior, i.e. no limit on upper frequency of matching. The length of the coupling section controls the lower frequency of matching at a given allowable reflection coefficient.

The equation that determines the condition for tightest coupling in [56] is

$$\frac{k^2 - s}{k} = \frac{\sqrt{\epsilon_r} Z_o}{60\pi^2} \ln(4) \quad (3-20)$$

where s is the normalized thickness of the middle substrate and ϵ_r is the relative permittivity of the substrates. Low cost Rogers RO4003C™ microwave substrates ($\epsilon_r = 3.38$) with 17.5μm thick copper cladding are used for the design implementation. Equation (3-20) is used to determine the substrates thicknesses of the hybrid. The available thicknesses of the Rogers RO4003C™ substrates are limited. With the choice of top and bottom substrates to be the thickest available at 1.5mm, the closest available thickness for the middle substrate to meet the condition in (3-20) is 0.3mm.

With the calculated values for the even and odd impedances along the length of the coupling section obtained from (3-16) and (3-17), a plot versus normalized length is given in Fig. 3.5. The width and offset of the tapering coupled line can be predicted from the set of equations given in [56]. The set of loose coupling equations gives a better accuracy for this design. The widths and offsets are calculated using MATLAB at 0.25mm intervals along the hybrid length and plotted in Fig. 3.6.

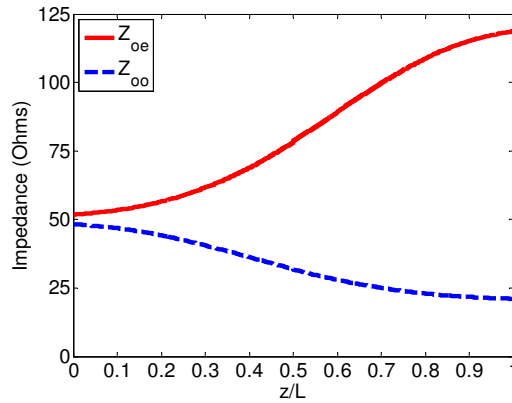


Fig. 3.5 - Even and odd mode impedances of the coupled lines.

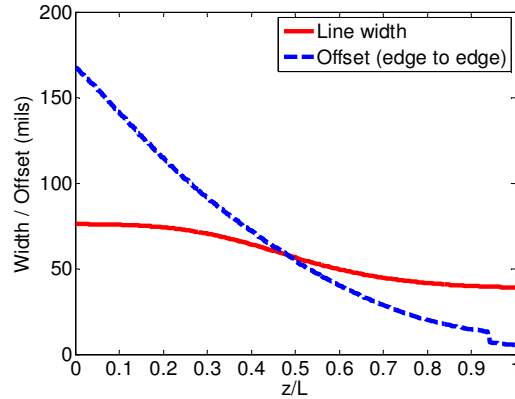


Fig. 3.6 - Dimensions of the coupled lines along the coupling section.

The layout of the designed hybrid is shown in Fig. 3.7. Size of the coupler is 13.5cm by 7.6cm. The patterns in red correspond to the upper striplines, and the blue lines are the lower. Grey structures are the grounds and white spaces are areas filled with the RO4003C™ dielectric.

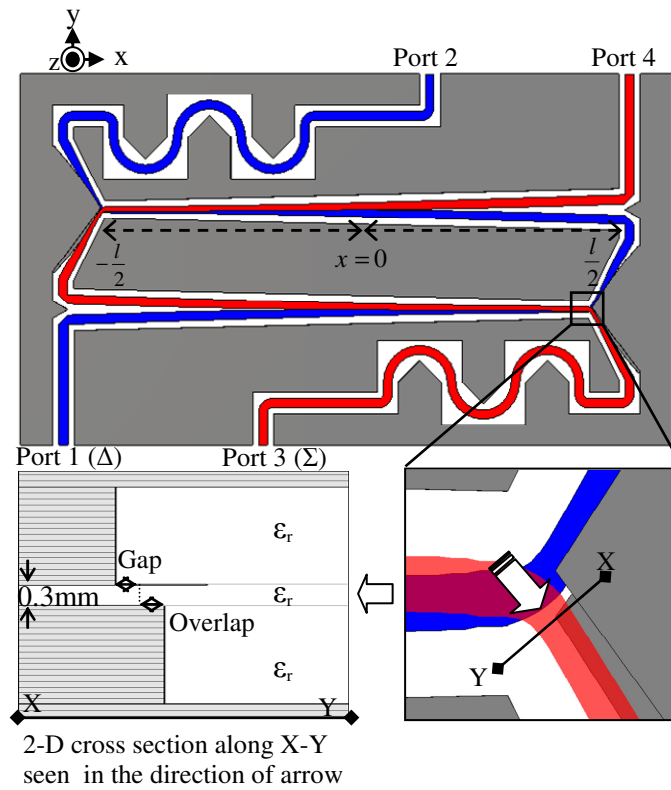


Fig. 3.7 - Structure of the 180° hybrid with gap and overlap grounds.

An important parameter in the performance of any hybrid coupler is its isolation characteristic. A higher isolation will ensure that most of the input power is transferred to the desired output ports and a minimal signal is leaked to the isolated port as noise. Ground structures are added at the coupled striplines transition to improve the isolation performance through the forced termination of coupled fields onto the grounds. The presence of grounds in the vicinity of the stripline alters its characteristic impedance, thus the width of the lines have to be adjusted for impedance matching.

The proposed addition of offset ground patterns at the transition of the coupled lines are shown in greater detail at the bottom of Fig. 3.7. An expanded view of the area is given in the figure on the right with the top layer stripline made partially transparent to show the overlapping ground below it, and the two-dimensional cross-section diagram along the cut-line X-Y is shown on the left. The width of the stripline for 50Ω characteristic impedance with the presence of gap and overlap-ground patterns can be found using the Method of Moments (MOM) [57]. The characteristic impedance for the stripline can be defined as

$$Z_o = \frac{1}{v \cdot C_l} \quad (3-21)$$

where $v = 1/\sqrt{\mu\epsilon}$ is the speed of wave propagation in the dielectric, and C_l is the capacitance per unit length due to the fixed potential (V_i) placed on the stripline conductor. The capacitance per unit length can be solved using

$$C_l = \sum_{j=1}^n \frac{\rho_j \cdot \delta}{V_i} \quad (3-22)$$

where ρ_j is the surface charge density of sub-length section j when the stripline is discretized into n sections of δ length. This is equivalent to the total charge per unit length of the two-dimensional cross-section over the potential difference across the surfaces. Here the unknowns are ρ_j , and can be solved using the Method of Moments.

A set of stripline widths for 50Ω characteristic impedance is solved for various gap and overlap grounds values using MATLAB and plotted in Fig. 3.8. A δ of 0.05mm is used for this calculation. The predicted solution is then used to develop the section of stripline that joins with the meandered lines without overlapping ground.

The meandered lines at the coupled output ports are added to shift the through port wave to align with the backward coupled wave such that the phase difference between them will be the desired 180°.

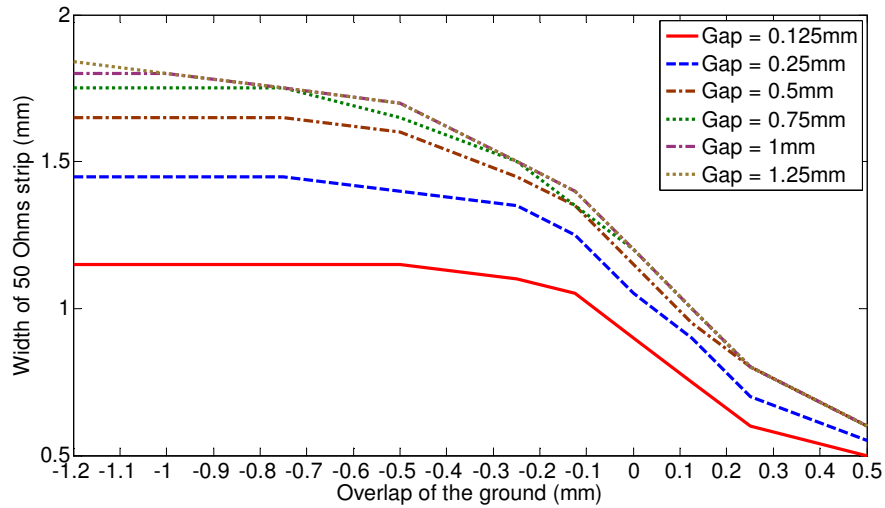


Fig. 3.8 - Line widths for various gaps and overlaps of grounds.

3.1.4 Results

The complete structure is simulated using CST MICROWAVE STUDIO® and the prototype design is built and measured. Return loss of the input port (S_{11}) and isolation (S_{31}) performance of the design are shown in Fig. 3.9. Measured results using an Agilent 20GHz bandwidth Vector Network Analyzer closely match with the simulated. Decade bandwidth operation is verified and isolation is better than 18dB. The performance target of 15dB worst case isolation is met. The through (S_{21}) and coupled (S_{41}) ports results are plotted in Fig. 3.10. Amplitude is equally split between the output ports and the amplitude balance is within ± 1.75 dB. The slope in the amplitude response is attributed to the substrate and conductor losses (insertion losses) that dominate in the upper frequencies. The design achieved a target of less than 5dB insertion loss. Phase response shown in Fig. 3.11 has a $\pm 22^\circ$ imbalance due to the phase equalization line for the through port being slightly short as seen in the time-domain results of Fig. 3.12, which has a 13ps time difference between the ports 2 and 4 output peaks. Thus it is correctable with proper lengthening of the meandered line, as proven with the following simulation result. The simulation in Fig. 3.13 shows that lengthening the meander line will compensate for the phase error. Even though the phase error is not within a targeted $\pm 10^\circ$ imbalance in absolute phase, the integrated feed network still managed to achieve a

decade bandwidth performance due to the tolerance of the inter-port quadrature phase maintained within the $\pm 10^\circ$ target limits across the decade bandwidth.

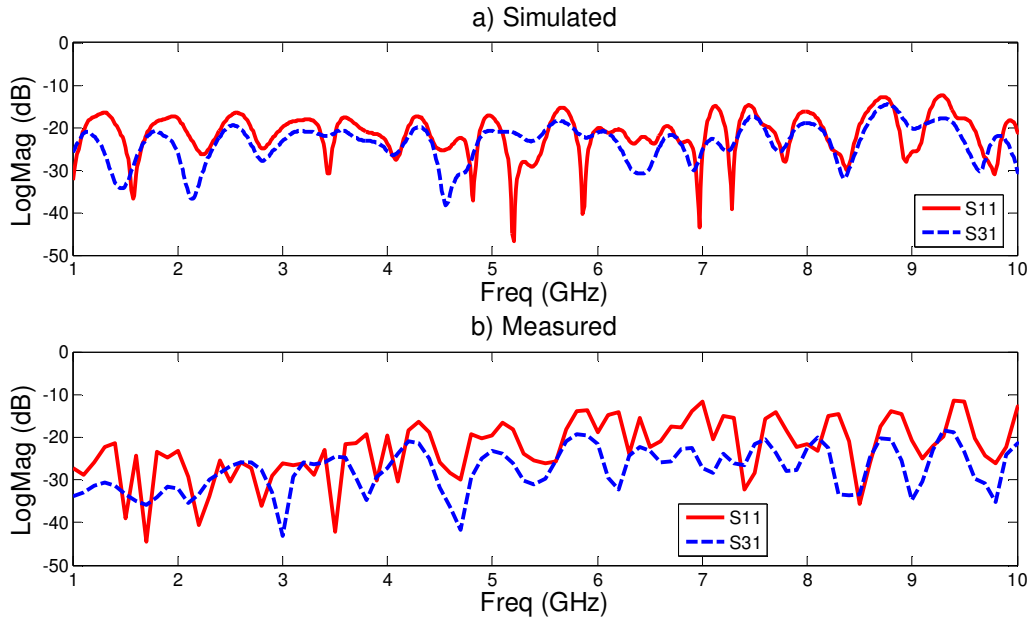


Fig. 3.9 - Input port return loss (S_{11}) and isolation (S_{31}) responses.

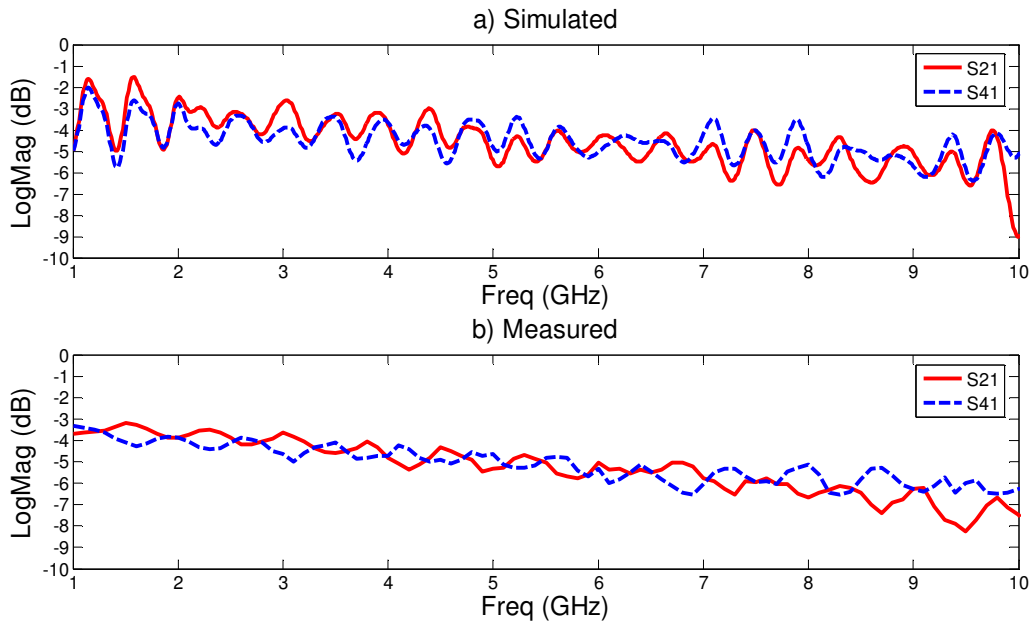


Fig. 3.10 - Through (S_{21}) and coupled (S_{41}) ports responses.

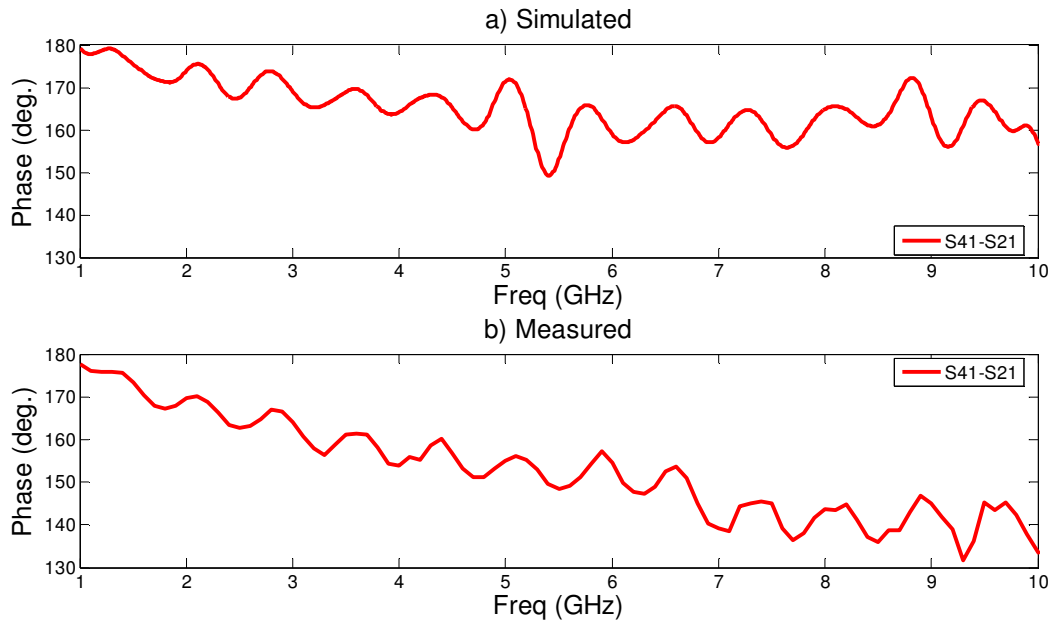


Fig. 3.11 - Phase difference between the coupled and through ports of the prototype 180° hybrid.

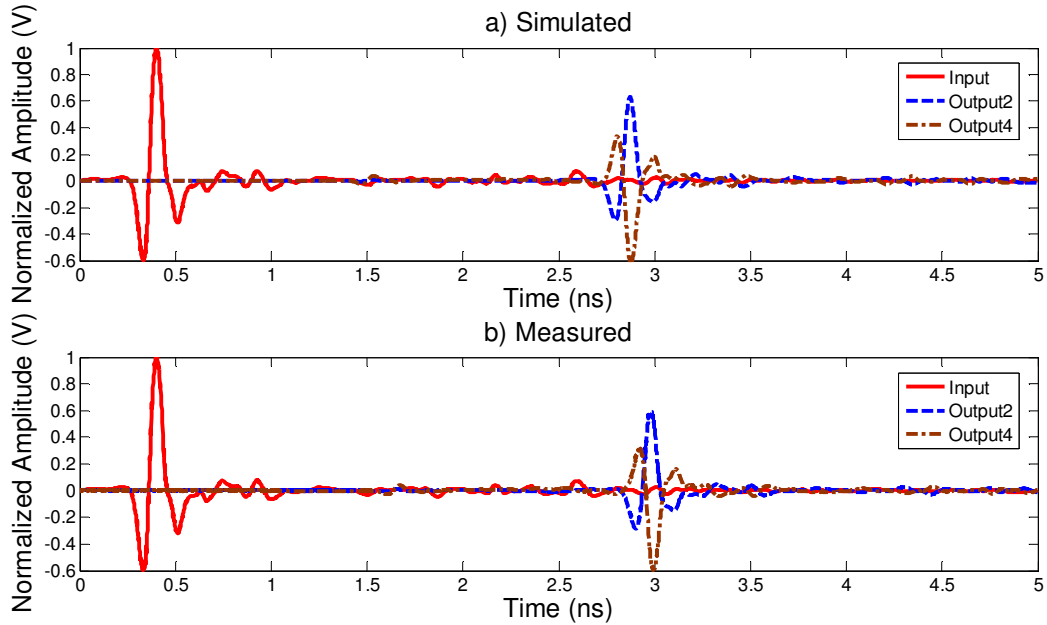


Fig. 3.12 - Time-domain input and outputs for the proposed 180° hybrid.

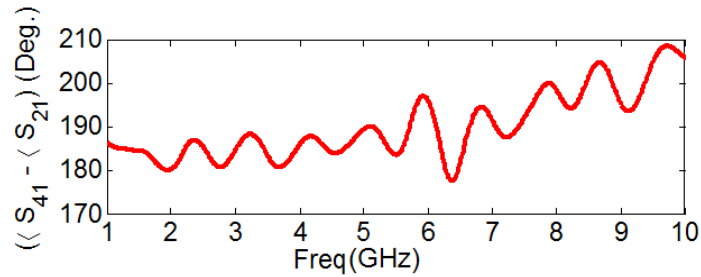


Fig. 3.13 - Simulation result of hybrid with lengthened meander line to correct for phase error.

For time domain measurements, the setup shown in Fig. 3.14 is used. The AVTECH pulse generator outputs 50ps rise time steps that are being passed through cascaded Picosecond impulse forming networks (IFNs) to generate second derivative Gaussian pulses of 65ps full width at half maximum (FWHM) pulse widths. The pulses are input to the hybrid coupler and the desired output measured using an Agilent sampling oscilloscope with 18GHz bandwidth. While the desired output port is being measured, the remaining ports are terminated with matched loads. The sampling oscilloscope is triggered by an external trigger from the AVTECH pulse generator for synchronization. The captured input pulse from the measurement is also used as the simulation input pulse in CST transient solver. The 0.2ns difference between the simulated and measured time-domain outputs is from the additional connectors and adapters attached to the prototype design during the measurements.

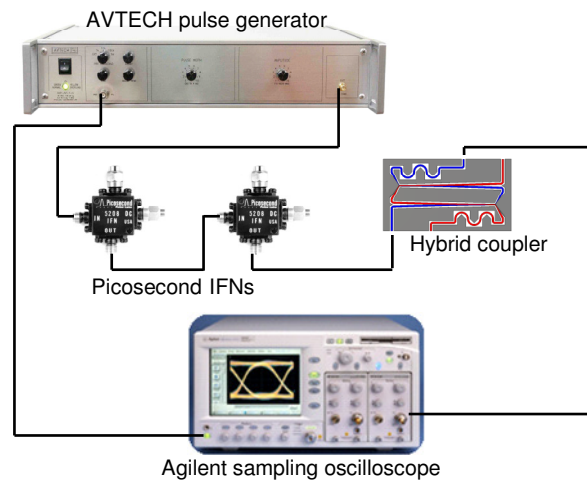


Fig. 3.14 - Time domain measurement setup.

A design without the gap and overlap grounds is simulated for isolation, and a comparison of the simulation results without and with the gap and overlap ground structures for isolation are shown in Fig. 3.15. The worst case isolation performance with the gap and overlap ground structures is at least 5dB better than without the gap and overlap grounds.

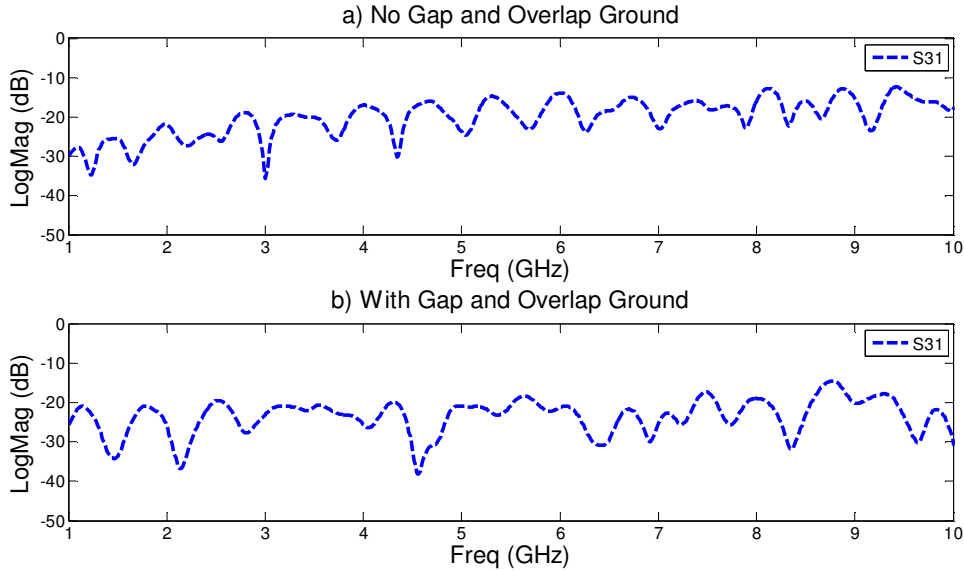


Fig. 3.15 - Simulation results of hybrid without and with offset grounds.

3.2 Quadrature hybrid coupler

The quadrature hybrid coupler will provide the necessary 90° phase angles to the antenna feed network. The coupler is required to have an equal power division (-3dB) to the output ports.

3.2.1 Types of quadrature hybrid coupler

Wideband quadrature hybrid designs are limited to multi-branch topology [58] and slot coupled striplines [59] yielding up to 110% bandwidth. However these structures do not lend themselves to be easily integrated with the decade bandwidth 180° hybrid proposed in Section 3.1. The design presented by [60] however is compatible with the triplate broadside coupled stripline configuration and can also achieve more than a decade bandwidth.

3.2.2 The symmetric 3dB quadrature hybrid coupler

For the design proposed by Rao [60], a symmetric 8.34dB multi-section coupler adopted from [61] was cascaded to form a 3dB quadrature hybrid coupler. The coupler by Cristal *et al.* [61] is developed using an optimization procedure to synthesize the insertion loss polynomials to fit the equi-ripple response for a given coupling level using cascaded fixed-length TEM-mode transmission lines. Cristal *et al.* developed tables of normalized even mode impedances for the 3, 5, 7 and 9 sections equi-ripple symmetric hybrid couplers.

Table 3.1
Impedances and dimensions of the nine section symmetric quadrature hybrid

Sections	Z_{oe} (Ω)	Z_{oo} (Ω)	Width (mm)	Offset (mm)
1 and 9	51.38	48.66	2.3	3.9
2 and 8	53.55	46.69	2.2	3.8
3 and 7	57.81	43.24	2.0	3.5
4 and 6	67.31	37.14	1.7	2.9
5	111.64	22.39	1.0	0.9

Table 3.1 gives a set of even and odd mode impedances calculated from the tables given in [61] for a 9 sections 8.34dB symmetric coupler with a 0.25dB ripple from the mean coupling. The nine section design is selected to meet the decade bandwidth requirement and to have more degrees of freedom than a design with a lesser number of sections that can meet the same bandwidth requirement (e.g. five or seven) for the design optimization. The tri-plate broadside coupled stripline configuration with same material and thicknesses as the 180° hybrid is adopted such that integration is possible. With the even and odd impedances for each section obtained, [56] is used to determine the widths and offsets for each section. The computed values using the tight coupling equations are given in Table 3.1. Section line lengths are a quarter-wave long at the centre frequency of 5.5GHz, which is 7.41mm. Two 8.34dB couplers are connected in tandem to realize the 3dB design.

The dimensions in Table 3.1 are used as initial values to design the quadrature hybrid. The design for a tandem 3dB quadrature hybrid is drawn in CST MICROWAVE STUDIO® and simulated. The diagram of the structure is displayed in Fig. 3.16. The top stripline is in red, the bottom in blue, the grey patterns are ground and white spaces are Rogers RO4003C substrate.

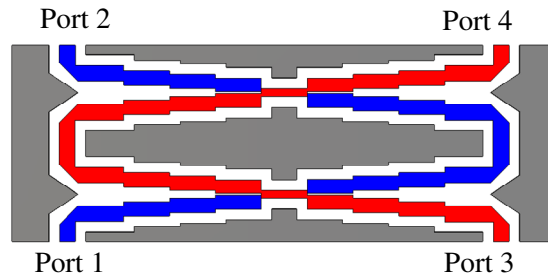


Fig. 3.16 - Structure of the nine section symmetric quadrature hybrid.

3.2.3 Optimization of the symmetric coupler design

A modification is made to smooth the step discontinuities at the transitions of each section by forcing the start points of the next section to be the end points of the previous section, while allowing the widths, offsets and lengths of each section at the start points to be optimization parameters; the exception is the middle section 5 which has a fixed offset set to 0 and an optimized width for both its end points. The modification is done to synthesize iteratively a continuous taper design, while preserving its bandwidth. Since the structure is symmetric, only five sets of widths and lengths are required with four sets of offsets (total 14 parameters) to optimize. The global Genetic Algorithm (GA) optimizer [62], with goal functions for coupling and return loss set at 3dB and 15dB respectively, is used to obtain a minimum error function. Multiple iterations of the global optimizer are carried out, and then the Nelder Mead Simplex Algorithm local optimizer [63] is used to refine the search for optimal dimensions for the set goals. Optimized widths, lengths and offsets of the sections for the prototype design are shown in Table 3.2.

Through an analytical procedure (using LineCalc [64] which uses the reverse of [56]), the characteristic, even and odd mode impedances across the optimized taper length are obtained from Table 3.2 data, and the results are plotted against the normalized length for half the structure as shown in Fig. 3.17.

Table 3.2
Optimized design dimensions for the proposed quadrature hybrid

Sections	Length (mm)	Width (mm)	Offset (mm)
1 and 9	4.0	1.6	3.4
2 and 8	4.3	1.8	3.9
3 and 7	4.1	1.4	2.1
4 and 6	3.0	1.5	2.0
5	2.9	0.7	0

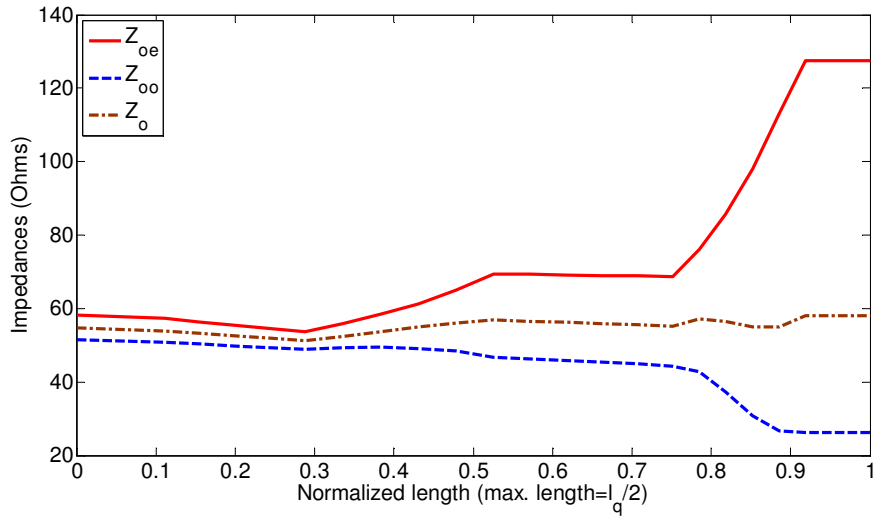


Fig. 3.17 - Impedances versus normalized length for the optimized quadrature hybrid.

The length l_q of the structure is expressed as

$$l_q = 1.128\lambda_c \quad (3-23)$$

where λ_c is the wavelength of the centre frequency.

For synthesizing the optimized structure, the graph of Fig. 3.17 can be broken into piece-wise linear segments for realization, or sample points may be taken and evaluated. It should be noted that performance is dependent on the choice of substrate materials (also limited by (3-20)), especially for losses that can dominate at higher frequencies.

Structure of the optimized coupler with dimensions given in Table 3.2 is shown in Fig. 3.18. The total size is 4cm by 2cm.

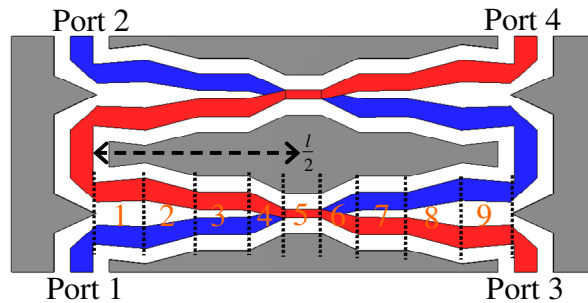


Fig. 3.18 - Structure of the proposed quadrature hybrid coupler; red is top stripline, blue is bottom stripline, gray is ground patterns and white space is substrate.

3.2.4 Results

The prototype design is assembled and measured results are compared against simulated as shown in Figs. 3.19 to 3.22. The measured results agree closely with the simulated, verifying the operation of the prototype design. Isolation is better than 15dB, amplitude balance within 2dB and phase balance within 5° across the decade bandwidth. These all meet the performance targets of 15dB isolation, 3dB amplitude imbalance, 5dB insertion loss and $\pm 10^\circ$ phase imbalance. Again the 0.1ns time difference between the simulated and measured time-domain outputs is due to additional connectors and adaptors used in the measurement.

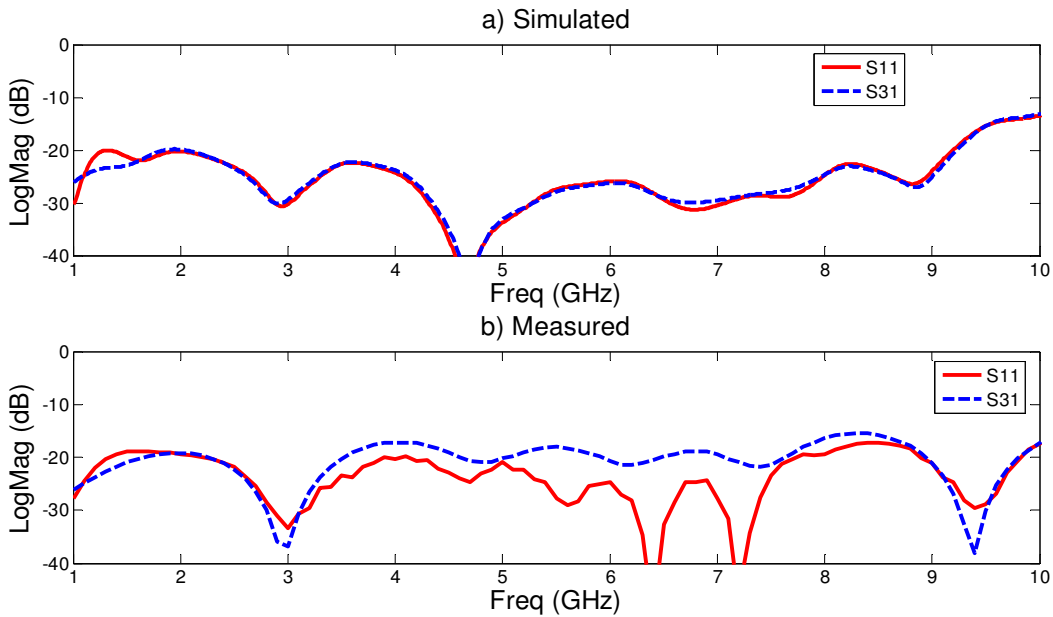


Fig. 3.19 - Input port return loss (S_{11}) and isolation (S_{31}).

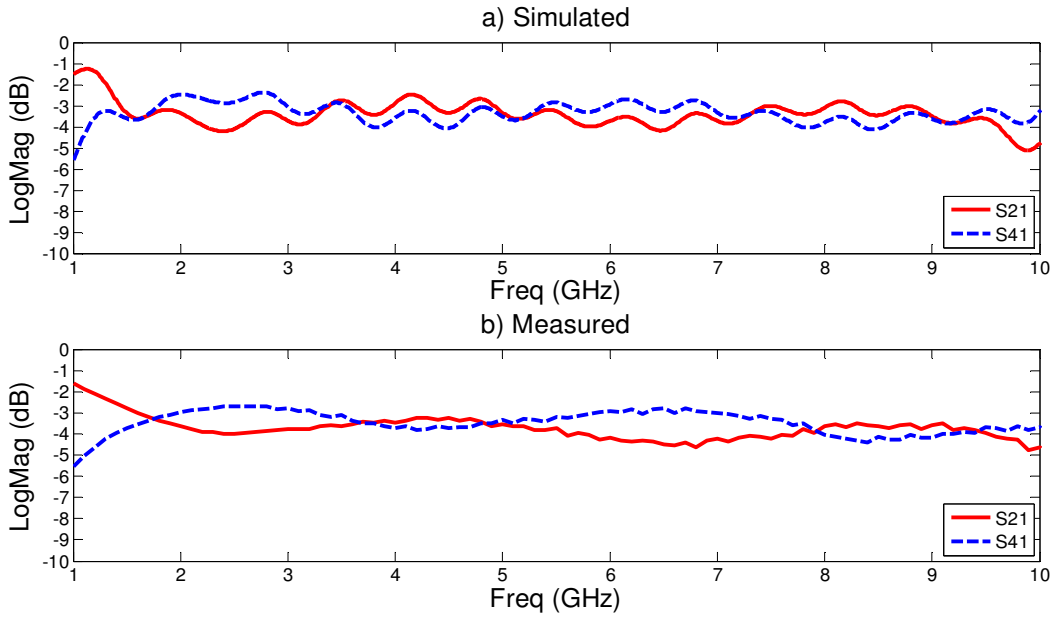


Fig. 3.20 - Through (S_{21}) and coupled (S_{41}) ports.

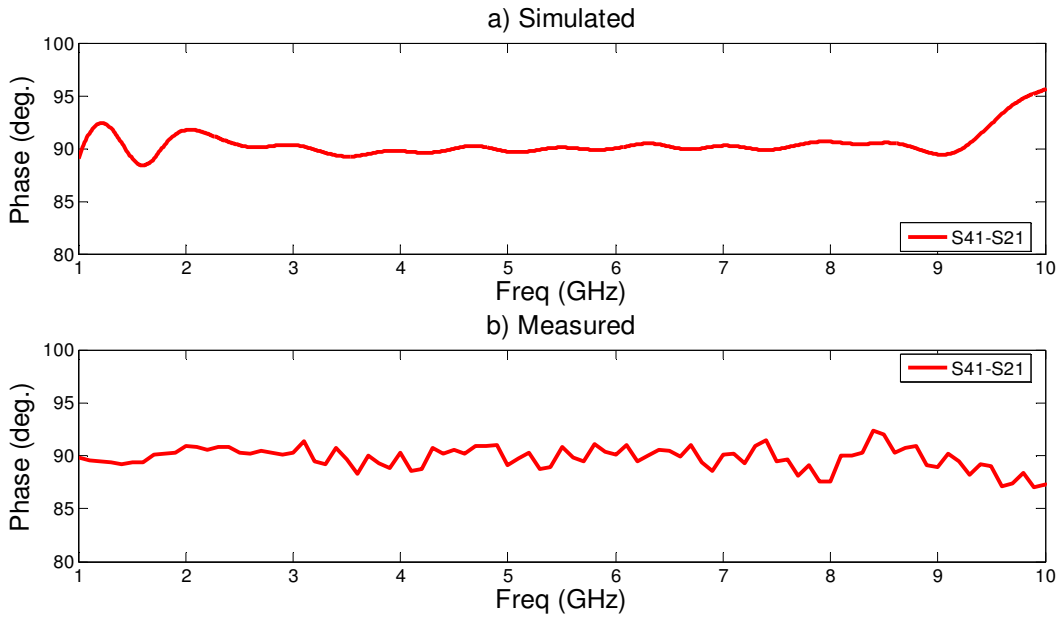


Fig. 3.21 - Phase difference between coupled and through ports.

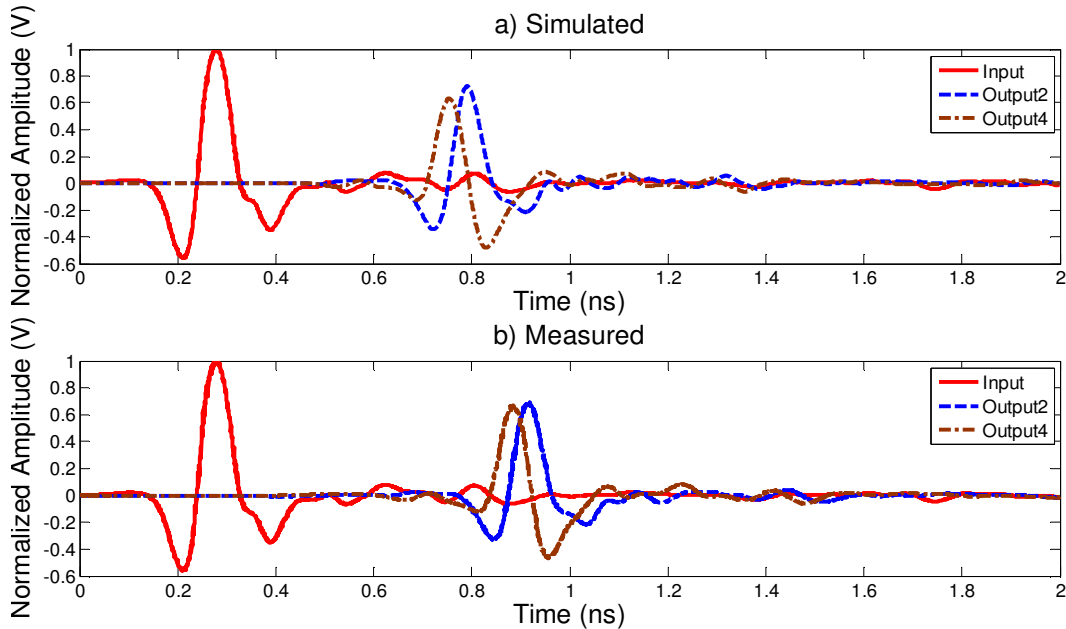


Fig. 3.22 - Time-domain input and outputs for the proposed quadrature hybrid.

3.3 Integrated feed network

The 90° hybrid is combined with two 180° hybrids according to the configuration described by Fig. 3.1, and integrated into a single structure to form the antenna feed network.

3.3.1 Design

The cascade will not work if the bandwidths of the elemental hybrids are not equally wide. The interconnecting lines from the quadrature hybrid outputs to the two 180° hybrids have to maintain length symmetry to preserve phase and amplitude balance (due to insertion losses). A diagram of the combined design showing the ports, top (red) strip, bottom (blue) strip and ground (grey) structures is given in Fig. 3.23. Total size is 30cm x 10cm. The input pulse is fed into port 1. Ports 5 through 8 are the 0° , 90° , 180° and 270° outputs respectively. Isolated ports are 2 to 4 that have to be terminated with 50Ω loads. A photograph of the prototype middle layer (0.3mm) substrate design with connectors attached is shown in Fig. 3.24.

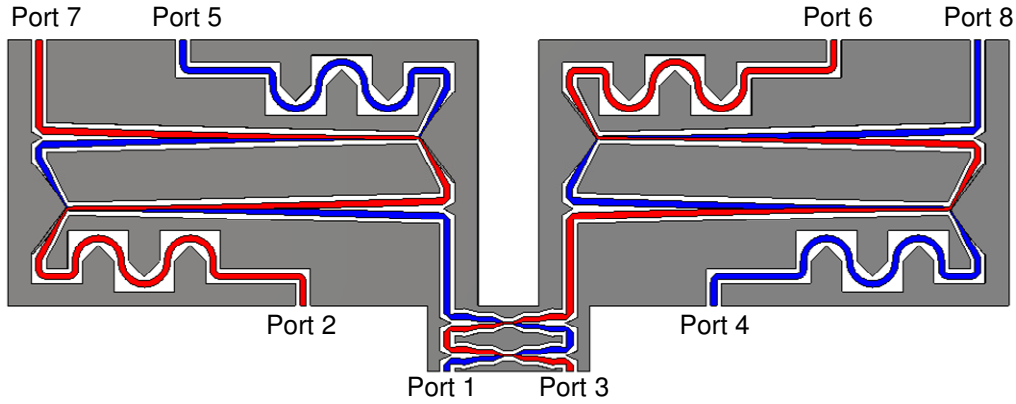


Fig. 3.23 - Structure of the proposed integrated feed network.

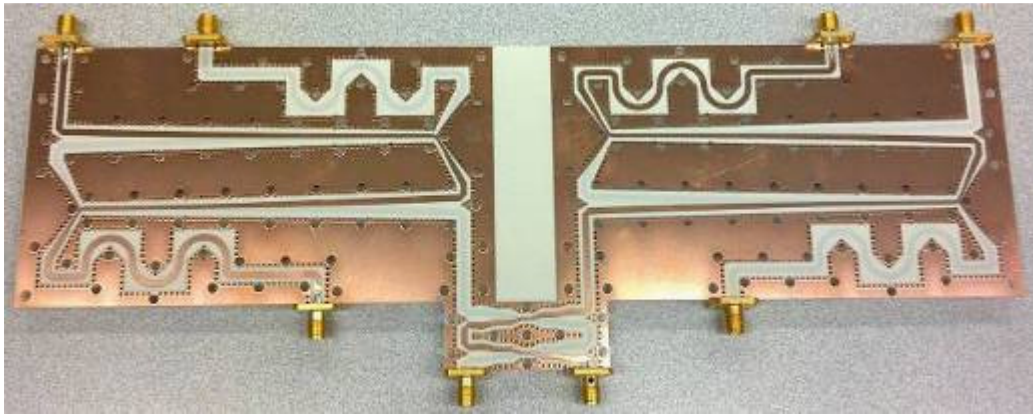


Fig. 3.24 - Photograph of the middle substrate layer with connectors.

3.3.2 Results

Verification of the device operation is confirmed from simulation and measurement results given in Figs. 3.25 to 3.29. The ripples in the outputs for the simulation results are due to non-unity energy balance for the transient simulator after it converged to the required accuracy. The measured amplitude balance for the output ports however is within 2dB. Maximum insertion loss is 4dB. Pulse shapes of the output ports given in Fig. 3.29 clearly show the proper function applied to the input pulse. The overall system meets the performance targets for 3dB amplitude imbalance and 5dB insertion loss. Though isolation for the quadrature port is 2dB worse than the target of 15dB, the coupled port response is not affected. Inter-port phases maintained within $\pm 10^\circ$ of quadrature phase.

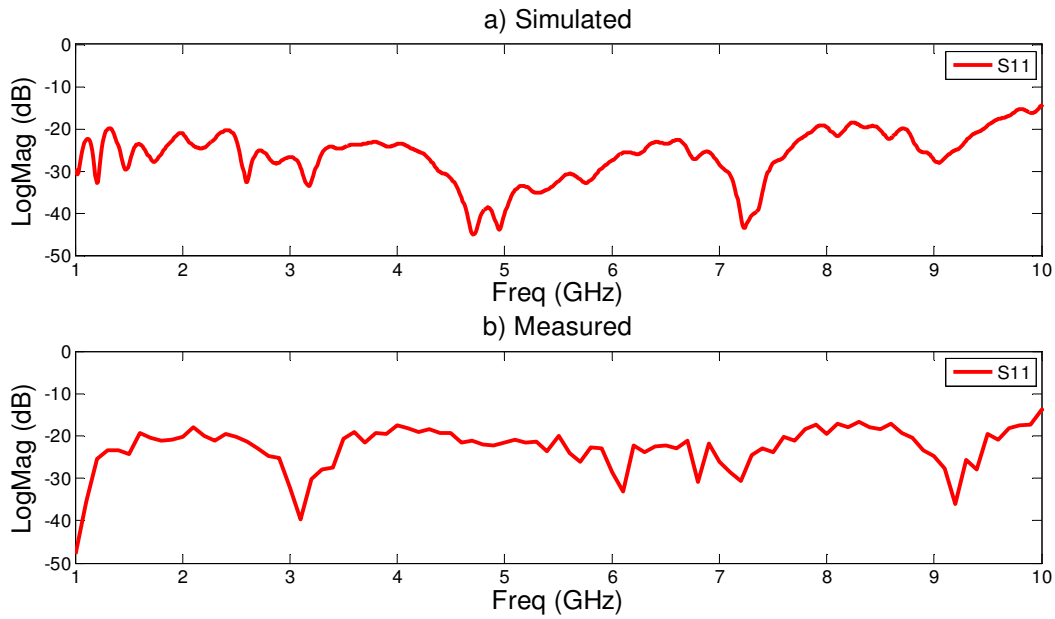


Fig. 3.25 - Input port return loss (S_{11}).

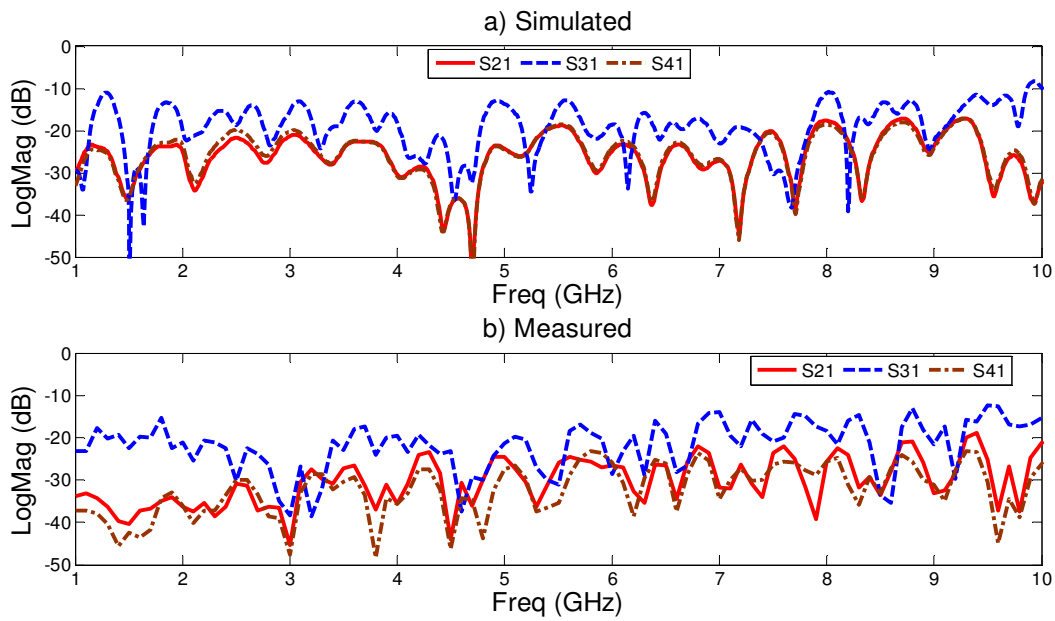


Fig. 3.26 - Isolated ports (S_{31} – 90° hybrid, S_{21} and S_{41} – 180° hybrid).

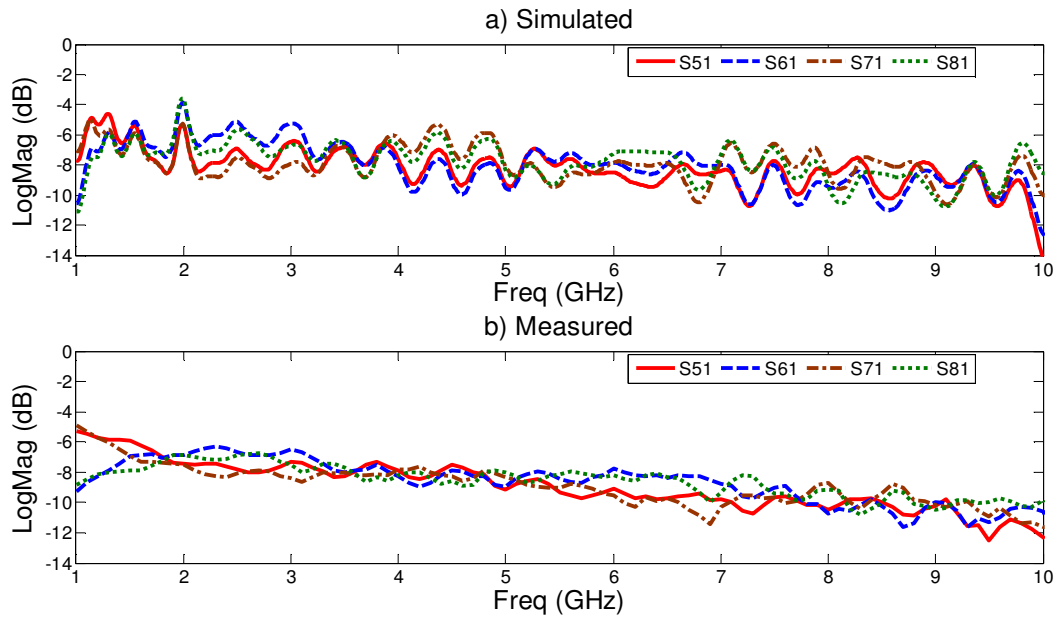


Fig. 3.27 - Through (S_{51}) and coupled ports (S_{61} , S_{71} , S_{81}).

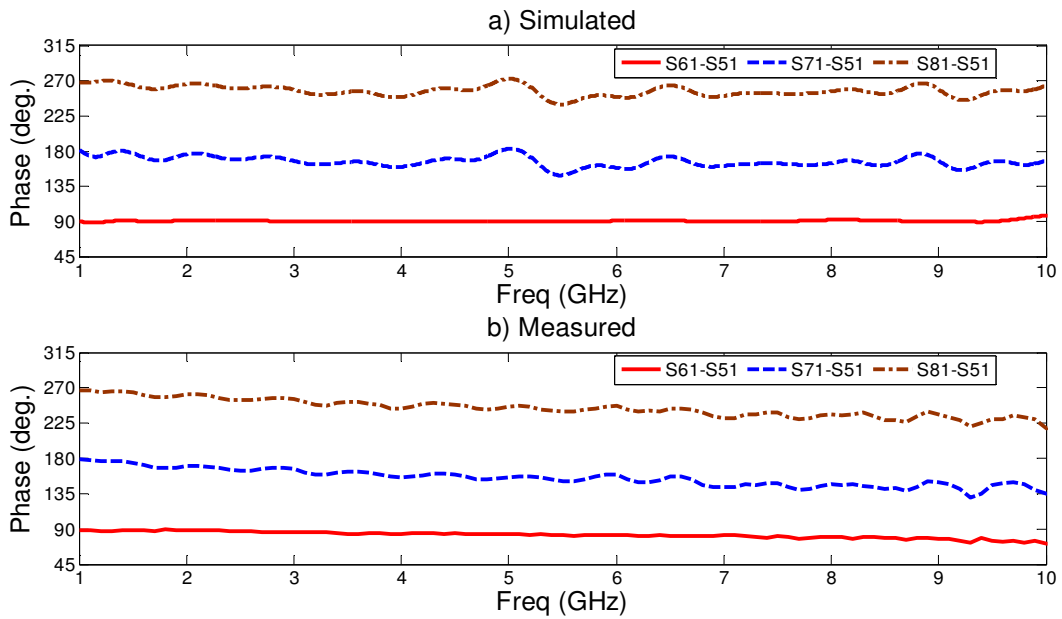


Fig. 3.28 - Phase differences between coupled and through ports.

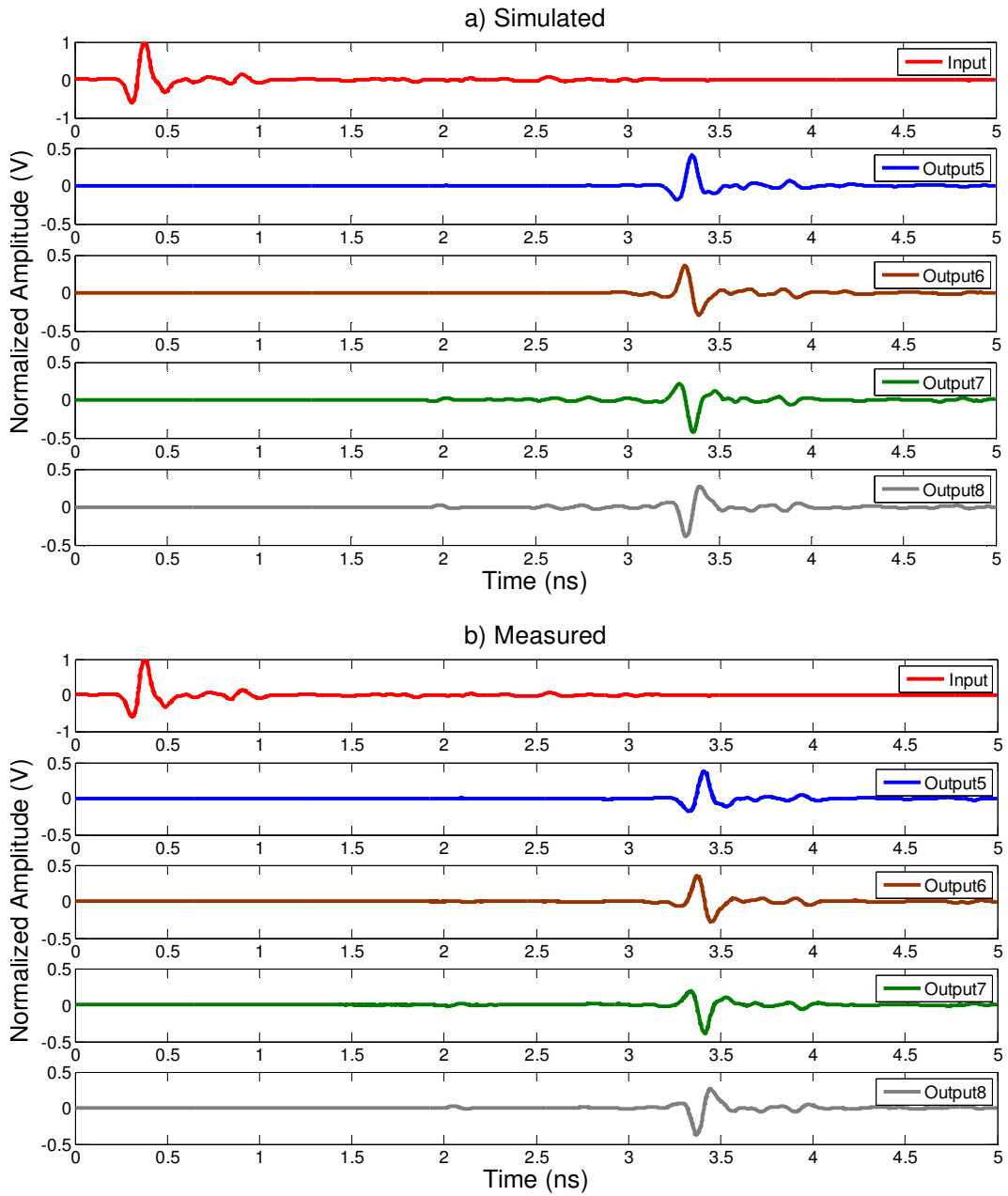


Fig. 3.29 - Time-domain input and output pulses for the proposed integrated feed network.

3.4 Circularly polarized antenna array

An array of four linearly polarized ultra-wideband (UWB) antennas rotated sequentially [65] by 90° are fed with the outputs of the feed network. The UWB antenna elements are scaled versions of the antipodal Vivaldi antenna [44] having a cut-off frequency of 1GHz. The leaves of the dual elliptical tapers and curved terminations are scaled up by a factor of 2.7 times to reduce the cut-off frequency from 2.7GHz to 1GHz. The antenna element dimensions are given in Fig. 3.30, and implemented using the RO4003C substrate of 0.8mm thickness. The red is top layer pattern, blue is bottom layer pattern, black outline is board dimensions and white space within the board outline is the dielectric material.

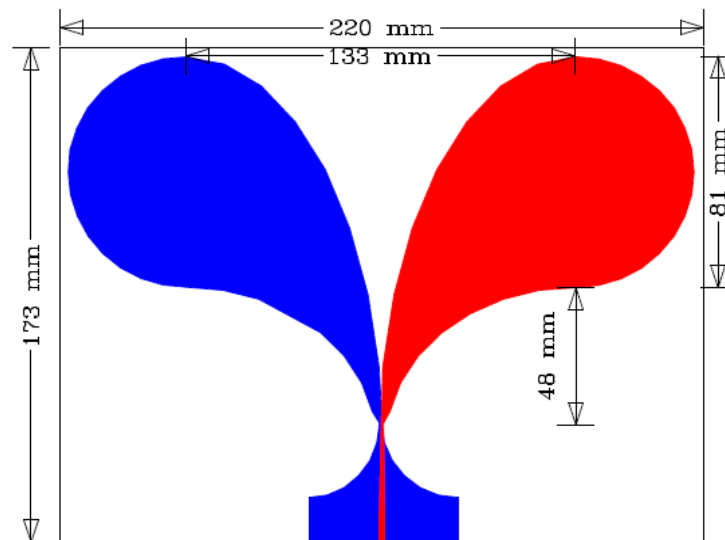


Fig. 3.30 - Dimensions of the antenna array element.

The elements are arrayed such that each edge of an antenna is aligned to the edge of its adjacent rotated element as shown in Fig. 3.31. A left-hand circularly polarized (LHCP) radiation is realized by feeding the left element with the leading phase output (270°) of the feed network with reference to the top element fed with the 0° output. The remaining feed network output ports are fed to their sequentially rotated antenna elements respectively. The isolated ports are connected to 50Ω terminations. A photograph of the antenna array with the feed network (partially obscured) mounted on a cylindrical near-field antenna measurement system is shown in Fig. 3.32.

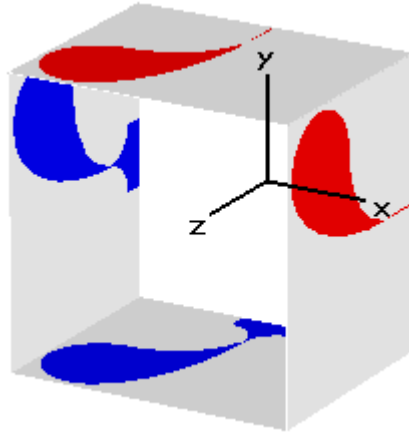


Fig. 3.31 - Circularly polarized antenna array arrangement.



Fig. 3.32 - Photograph of the antenna array mounted on antenna measurement system.

Fig. 3.33 shows the reflection coefficient of the antenna element having a lower cut-off frequency starting from 1GHz. After arraying through the feed network, the reflection coefficient of the antenna array maintained a decade impedance bandwidth as seen from the reflection coefficient curve plotted in Fig. 3.33. The inter-element mutual coupling is found not significant. The feed network together with the orientation of the elements minimizes the effects of mutual coupling.

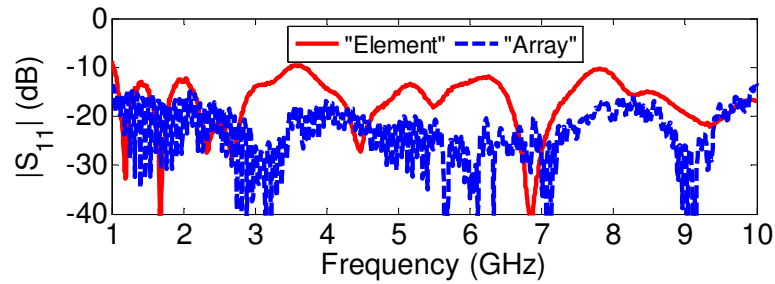


Fig. 3.33 - Reflection coefficient of the element and antenna array.

The normalized azimuth and elevation plane radiation patterns for the antenna array are given in Fig. 3.34. The left plots are for the azimuth planes and right side plots are the elevation planes. Fig. 3.34(a) and 3.34(b) are plots for 1GHz frequency (lowest frequency), 3.34(c) and 3.34(d) are 5.5GHz (mid-band), 3.34(e) and 3.34(f) are 10GHz (highest frequency). The simulation and measurement results are in agreement to within 2dB in the half-power beam-width.

Achieving a decade bandwidth 3dB axial ratio for a circularly polarized UWB antenna is a known challenge. The proposed antenna array achieves a decade bandwidth axial ratio (measured in the boresight (0°) direction) as shown in Fig. 3.35. The combination of the use of a decade bandwidth feed network and the sequential rotation of UWB antennas provide for such a superior performance.

The simulated gain of the antenna array is plotted in Fig. 3.36. The gain response peaks at 14.7dBi at 7GHz and remains stable around 14dBi to 10GHz.

The phase center of the antenna is determined to be the spatial position whereby the radiation originates, and is estimated by altering the source location and observing the phase patterns in the far-field over a predetermined beamwidth (e.g. 3dB beamwidth). The source location that causes the phase pattern within the beamwidth to be maximally flat (i.e. constant) is called the phase center. The phase center of the proposed antenna array (from the origin of structure in Fig. 3.31 along the z-axis) is presented in Fig. 3.37 (red solid line). This is confirmed in the measurement of the propagation delay for a pair of antenna separated over a distance of 1m. The group delay is measured with a vector network analyzer and the contributing delays (with respect to frequency) of the feed network, wave propagation for 1m and cables are removed from the measured total delay, leaving the delay due to the antenna array plotted in Fig. 3.37 (blue dashed line). A set-up of the phase center measurement is shown in Fig. 3.38.

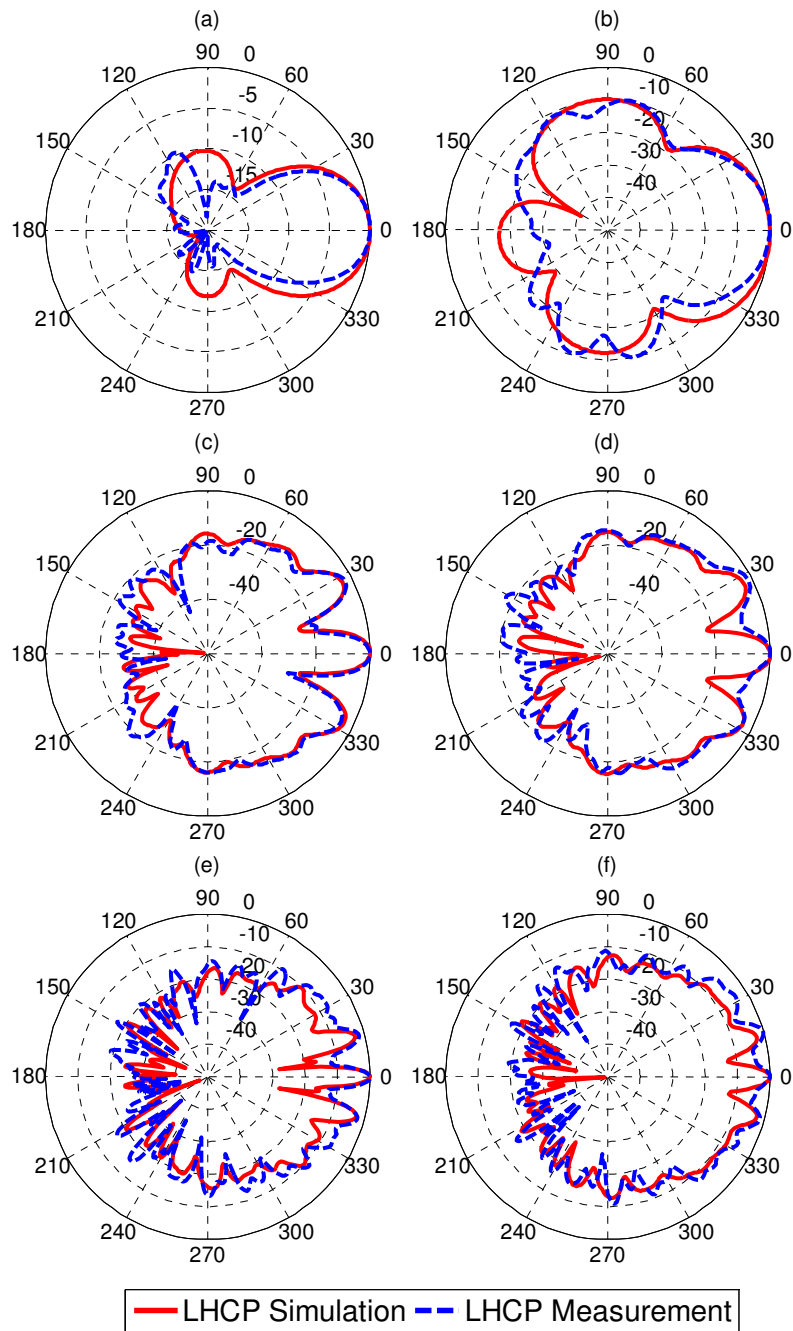


Fig. 3.34 - Radiation patterns; (a),(b): 1GHz, (c),(d): 5.5GHz, (e),(f): 10GHz; azimuth (left) and elevation (right).

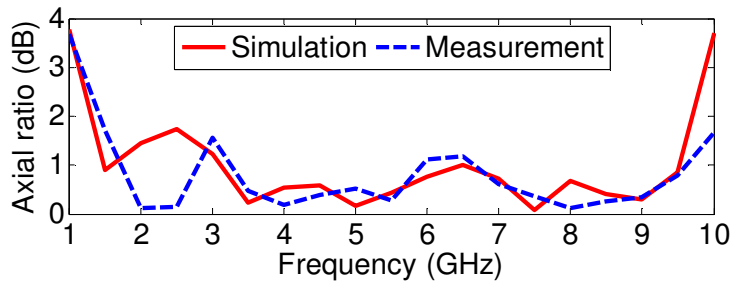


Fig. 3.35 - Axial ratio for CP antenna array.

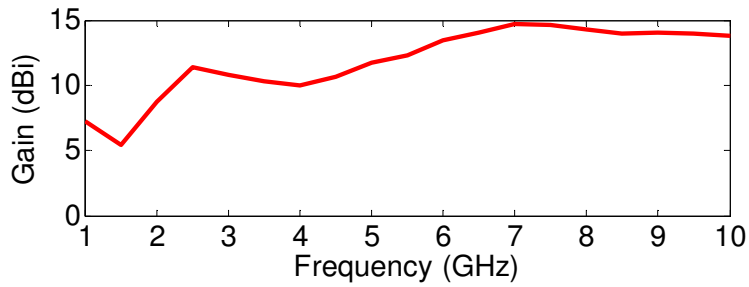


Fig. 3.36 - Simulated gain as a function of frequency.

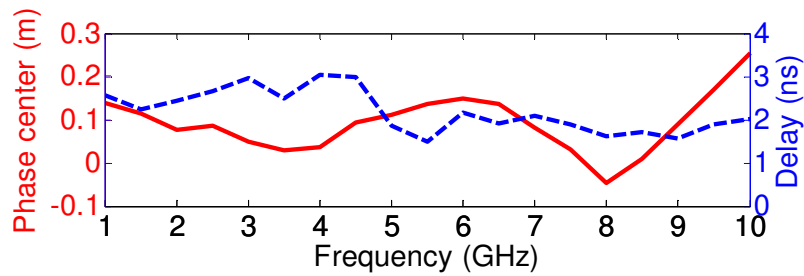


Fig. 3.37 - Phase center and propagation delay of the antenna array.

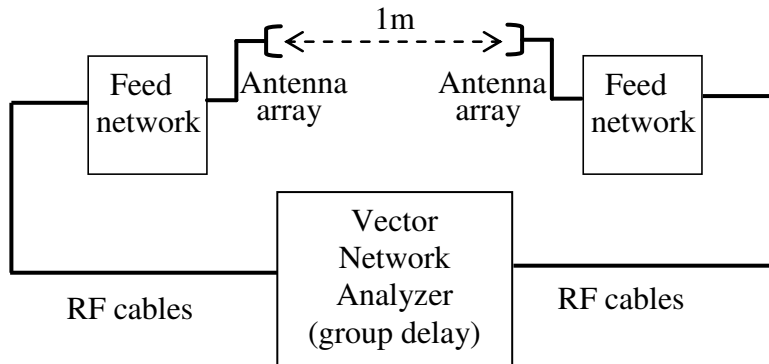
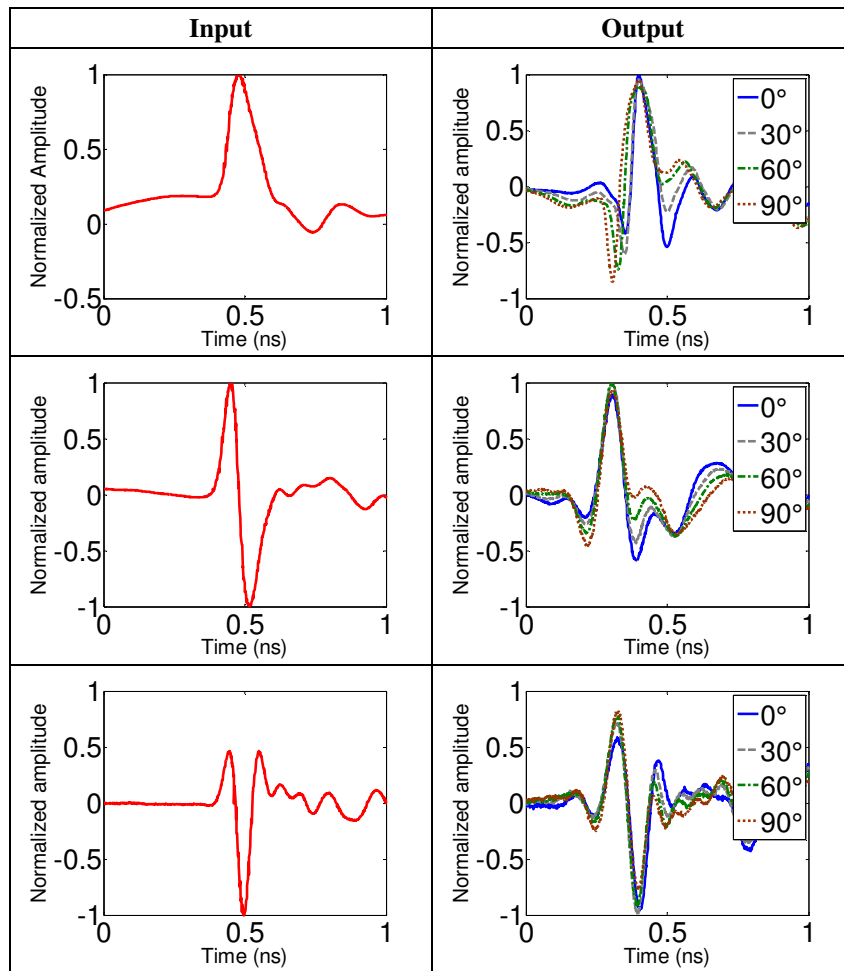


Fig. 3.38 - Phase center measurement set-up.

To further exhibit the robustness in pulse reception for CP, the pulse propagation of various Gaussian pulse shapes with a rotation of the antenna along the z-axis (c.f. Fig 3.31) is summarized in Table 3.3. Gaussian, first derivative Gaussian and second derivative Gaussian pulses with 200ps FWHM pulse widths are fed into a linearly polarized transmit antenna as input signals (left column). The received pulses using the proposed circularly polarized antenna array are recorded at rotation angles of 0° , 30° , 60° and 90° and overlaid on the same plots in the column on the right.

Table 3.3
Received pulses with antenna rotation



From Table 3.3 results, it can be observed that the received pulse amplitudes remain constant with the rotation angles. The received pulse shapes for the antenna pairs are differentiated forms of the input pulses which are expected according to theory [66]. With angular rotation, the received pulse shapes have limited distortions; less than 36% for

Gaussian input, less than 24% for first derivative Gaussian and less than 17% for second derivative Gaussian. Pulse distortion is determined using a cross-correlation analysis of the received pulses at various rotation angles as compared with the received pulses at 0°. The received pulse results in Table 3.3 demonstrate the robust performance of the antenna array in reception regardless of the polarization angle.

The goal of the thesis for system robustness has been achieved through the successful design of the decade bandwidth circularly polarized antenna array. The main contribution of this thesis is the demonstration of decade bandwidth circular polarization which is reported for the first time in literature. The feed network design incorporates a gap and overlap ground feature that improves isolation performance by more than 5dB as compared to existing designs. The completion of fabrication and characterization of the antenna system enables its use in vital signs monitoring, as described in the next chapter.

Chapter 4

Robust contactless sensor for real-time vital signs monitoring

Traditional vital signs monitors adopted in the health-care industry use contact-based methods, such as electro-cardiographs (ECG) and pulse oximeters [67]. Though proven and time-tested, these systems require the patients to wear the sensors constantly for measurements. Contactless methods for vital signs measurement can offer significant advantage over the existing practices, especially when an unobtrusive and seamless solution is required. This technology could be a game-changer in terms of flexibility, safety, and has an ability to enhance both new and existing applications.

Contactless sensors for vital sign monitoring and their networking with the central medical facilities are very important for the following requirements: (i) controlling the spread of contagious diseases such as H1N1, avian influenza, and severe acute respiratory syndrome risks to health workers, who monitor the patients in close proximity using electrode-based life sign monitoring and diagnostic tools, (ii) to improve the efficiency of hospitals by providing automated medical services in intensive care units, for example round the clock patient observation, (iii) to reduce the errors in vital sign measurements due to the clinical anxiety in patients, especially in the case of children undergoing the wiring and strapping of electrode-based devices, (iv) to reduce the overall expenditure of patient care and improve the efficiency of health care staff and its management.

At present, there are relatively few heart beat and breathing rate monitoring radars being developed. Two main approaches are adopted in the implementation of remote vital signs monitors; impulse response radar and Doppler radar techniques. The first heart beat and breathing rate monitoring radar was built in 1994, by T.E. McEwan, at Lawrence Livermore National Lab, USA [68]. Based on McEwan's impulse response radar design, prototypes [69, 70] have been developed over the years, demonstrating the capabilities of the ultra-wideband (UWB) radar in detecting human heart beats and breaths. Recent research progress includes using the deconvolution of system response [71] to improve the ability to detect the weak heart beat signals, and the cancellation of the breath

Portions of this chapter have been published in reference [15]

harmonics using a Moving Target Indicator (MTI) filter [72] that increased the accuracy of the heart beat rate prediction. On the other hand, a heart beat and breathing rate radar has also been developed using a 24.1GHz narrow-band Doppler radar technology [73]. The radar is capable of detecting human breathing and heart beating at a distance of 10 meters. Since then, Doppler radars have also advanced by employing phase- and self-injection locking in the oscillator design to remove clutter DC offsets [74], and miniaturized into a semi-conductor chip for low cost operation [75]. A dual-channel technique is also proposed to compensate for noise due to movements of the body [76]. However, all the present designs suffer from fading radar cross-section (RCS) due to the random orientation of human and bodily movements.

Superior imaging accuracy capabilities of UWB radars, in the order of few millimeters [37], paved the way into the medical industry as a better alternative to function as diagnostic and vital sign monitoring tools. In this thesis, we propose the design of a robust UWB radar system for contactless vital signs monitoring.

The fading RCS problem in a radar system is due to the use of linearly polarized (LP) antennas for transmission and reception. Electromagnetic scattering in LP systems for naturally occurring objects, which often have multiple boundaries of different materials, thicknesses, shapes and sizes, tend to have a rotation of electric vector (polarization) at the interfaces. Hence, the receiver antenna does not have a natural alignment to the polarization angle of the scattered wave. Furthermore, moving objects create a time-varying RCS that worsen the stability of the system. Therefore, to realize a robust UWB radar system, circular polarization (CP) is implemented such that reception from any polarization angle can be maintained, thus stabilizing RCS over time.

Recent CP UWB antennas yielded axial ratio bandwidths from 6.37 to 10GHz [77] using a quasi-spiral structure, from 5 to 7GHz [78] and 3 to 5GHz [79] adopting loaded square slot methodologies. It is a known challenge to achieve wideband CP bandwidth covering the FCC approved UWB band from 3.1 to 10.6GHz.

4.1 System design

Fig. 4.1 shows the schematic of the proposed circularly polarized UWB radar system. It is based on stored reference correlation receiver architecture [80] for its high sensitivity and ease of implementation. A time expansion [81] method is adopted in the correlation receiver such that baseband analog-to-digital sampling can be done at the

kilo-Hertz range due to bandwidth reduction, thus saving substantial cost and power of the system while preserving real-time operation. Signal processing computation of the baseband signals can be carried out using a budget personal computer (PC) or micro-controller, and the low power consumption allows for battery operation.

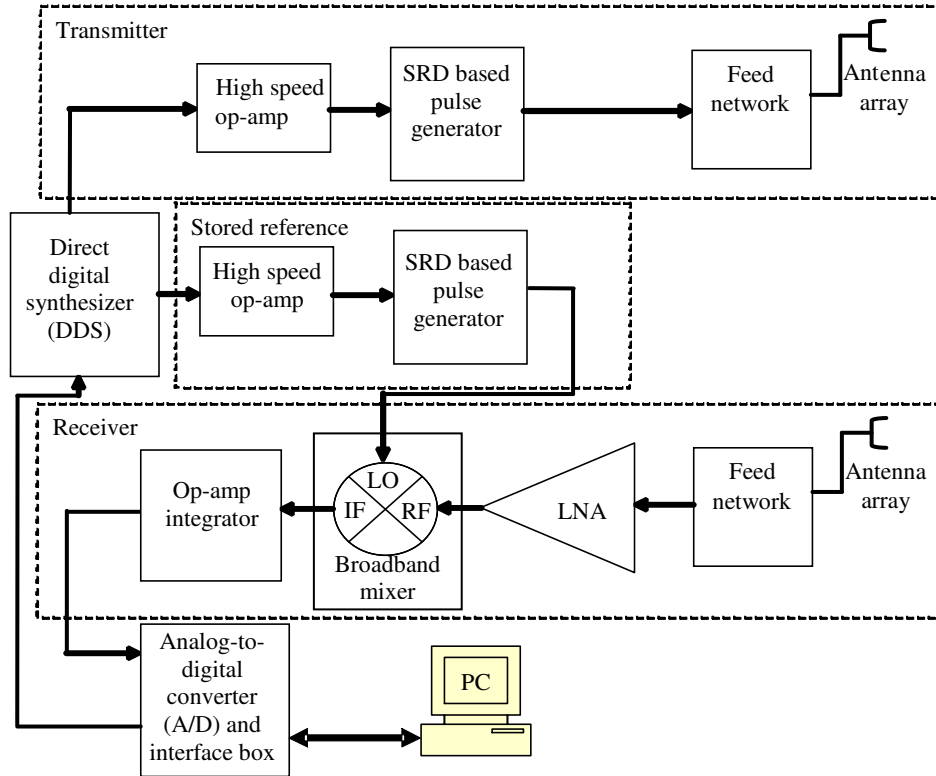


Fig. 4.1 - Schematic of the UWB radar system.

The pulse repetition frequency (PRF) of the UWB radar is controlled through commands from the PC to an Analog Devices AD9959 direct digital synthesizer (DDS), which is capable of generating sinusoids up to 250MHz at 0.1Hz frequency tuning resolution. The DDS has four channels; one channel is used for the transmit pulse and another for the stored reference pulse. The transmit PRF for the UWB radar system is set at 50MHz, that allows for a maximum round trip distance of 6m. Even though range of the radar can be changed by changing the PRF, due to low power operation (low signal-to-noise ratio) the range of the radar is limited to 3m.

The outputs from the DDS are amplified via high speed op-amps (Texas Instruments OPA699) and fed to step recovery diode (SRD) based pulse generators [12]. The cascaded shunt mode SRD with decreasing lifetime method of pulse generation produces

high amplitude pulses of $\sim 3\text{Vp-p}$ at low PRFs (MHz range), thus the pulse generator can directly drive the antenna sub-system saving the need for expensive broadband power amplifiers. The generated pulses are first derivative Gaussian pulses of $\sim 200\text{ps}$ FWHM pulse width having frequency content from 2 to 10GHz for a 10dB bandwidth. The spectral plot of the pulse is shown in Fig. 4.2. Although the pulse bandwidth exceeds the FCC approved band, a band pass filter placed before the antenna sub-system can ensure compliance to the mask limits. This prototype shows that the system is capable of circular polarization across the full FCC approved band.

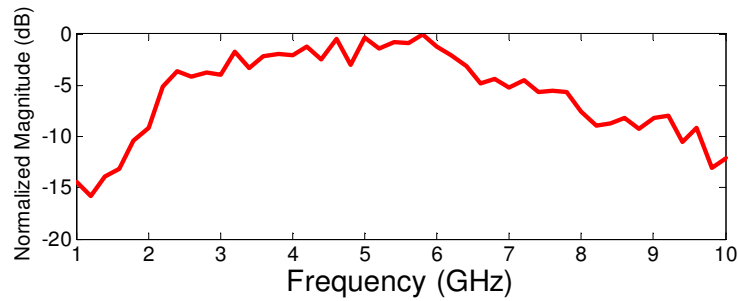


Fig. 4.2 - Spectrum of the output pulse.

The basic concept of time-expansion is to generate an expanded version of a periodic time-domain waveform, using multiple periods as determined by the expansion factor (F). A pre-requisite for this technique is periodicity of the waveform. A broadband mixer is used as the time-domain correlator. The time expansion is carried out by applying a slightly lower PRF for the reference pulses at the LO port (PRF_{LO}) as compared to the PRF at the RF port (PRF_{RF}). The required PRF_{LO} for a given time expansion factor F is determined by:

$$PRF_{LO} = \frac{F}{F+1} \times PRF_{RF} \quad (4-1)$$

A time expansion factor (F) of 2,000,000, meaning the 200ps pulse is expanded to a 400 μs pulse, is chosen such that the bandwidth of the baseband signal is reduced to 2.5kHz. The time expanded signal is sampled at 100kHz, which can be handled easily by low cost solutions. The resultant frame rate of the time expanded 50MHz PRF is 40ms, which is a tolerable delay for real-time vital signs monitoring.

The time expansion is carried out by setting the PRF of the stored reference pulse generator to be 49.999975MHz. A broadband mixer (Mini-circuits ZX05-C60) is used for the correlation between the received and reference pulses. The time expanded pulses are amplified through an op-amp integrator, which integrates the pulse energy, before being fed to an analog-to-digital (A/D) converter. The time constant of the op-amp integrator has to be set to match the bandwidth of the time expanded signal.

A photograph of the implemented hardware is shown in Fig.4.3. The overall system consumes less than 1W of power.

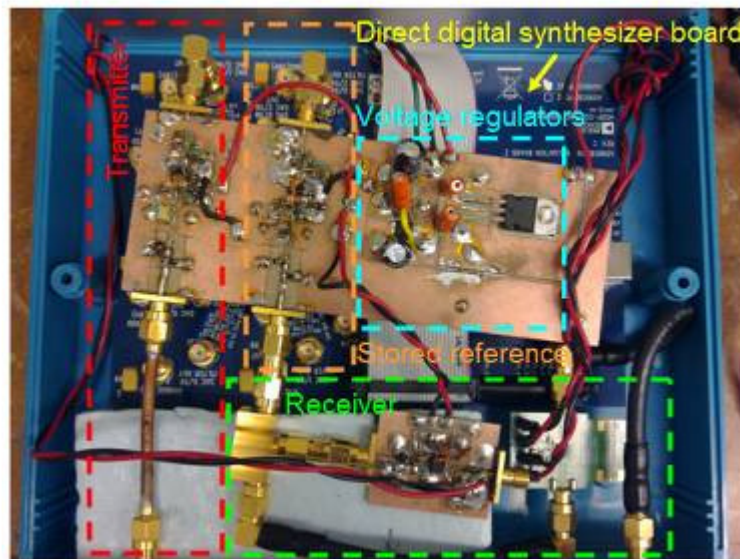


Fig. 4.3 - Photograph of the UWB radar hardware.

The CP antenna consists of a decade bandwidth feed network that produces orthogonal pulses with phases of 0° , 90° , 180° and 270° , and an array of linearly polarized UWB antennas arranged in a sequential rotation manner [82]. This method of generating CP preserves the axial ratio (AR) performance over the UWB band in the boresight direction, resulting in superior AR bandwidth.

4.2 Time expanded correlation receiver

This section will describe the concept and operation of a time expanded correlation receiver. The time expansion concept was introduced by Wochar *et al.* [81] as a method to use low bandwidth samplers to capture high bandwidth periodic pulses.

In order to process the received radar signals for the extraction of vital signs information, it is necessary to digitize the pulses detected by the receiver. Nyquist criterion has to be satisfied for the Analog-to-Digital Converter (ADC) such that aliasing will be prevented. The digitization of a 200ps FWHM pulse requires a sampling frequency in excess of 20GHz, thus data processing for real-time applications become impractical.

For UWB receivers, the correlation based architecture is a simple and cost effective method for pulse detection. A broad-band mixer is a necessary component in the correlation UWB receiver. The block diagram of a stored reference correlation UWB receiver is shown in Fig. 4.4. As the block diagram implies, the sampling speed of the ADC depends on the time-constant of the integrator. Therefore the sampling frequency will be much less than 20GHz.

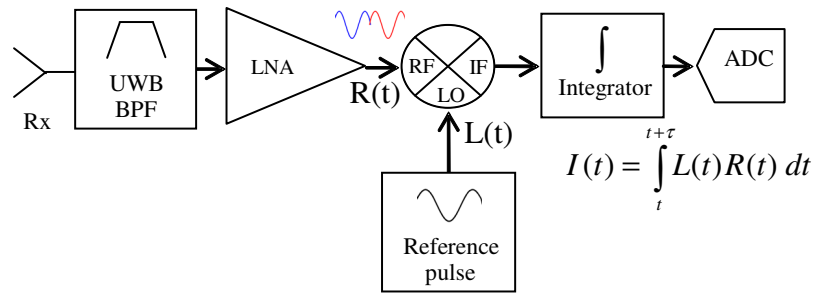


Fig. 4.4 - Block diagram of stored reference correlation receiver.

In UWB radar applications, the received pulse shape is an important parameter [8]. Thus merely detecting the presence of pulses is insufficient. The ability to quantitatively determine a low rate sampling frequency (~MHz) and pulse shape preservation become motivations to propose the time-expansion scheme using the correlation based architecture.

The basic concept of time-expansion is to generate an expanded version of a periodic time-domain waveform, using multiple periods determined by the expansion factor. The schema is illustrated in Fig. 4.5 for an expansion factor of 1000 as an example. Another term commonly used to describe time-expansion is equivalent-time sampling [83].

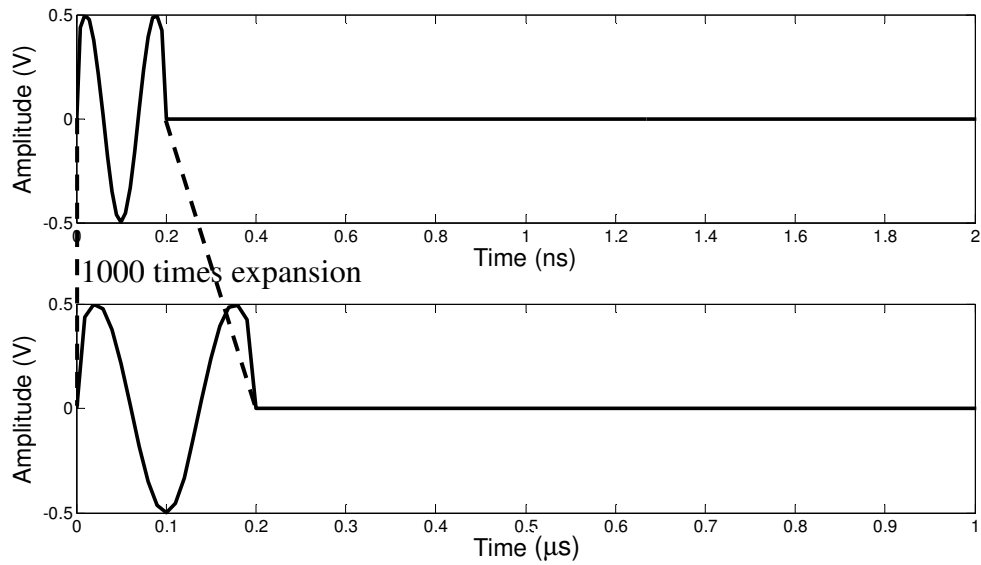


Fig. 4.5 - Example of a 1000 times expanded waveform.

Fig. 4.6 shows the example of a UWB radar system operating with a pulse repetition frequency (PRF) of 10MHz illuminating a target at 1m distance. The pulse repetition interval (PRI) is 0.1μs. The radiated pulses are 200ps time-gated sinusoid of 6.5GHz center frequency. Fig. 4.7 shows the undistorted waveforms (ignoring antenna, channel and target dispersion effects) observed at the output of the receiving antenna with normalized amplitudes.

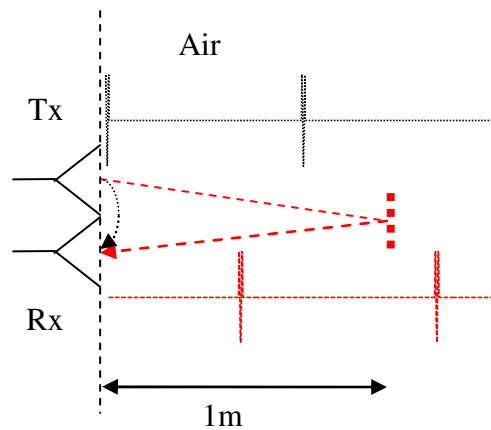


Fig. 4.6 - Example UWB radar system with target at 1m.

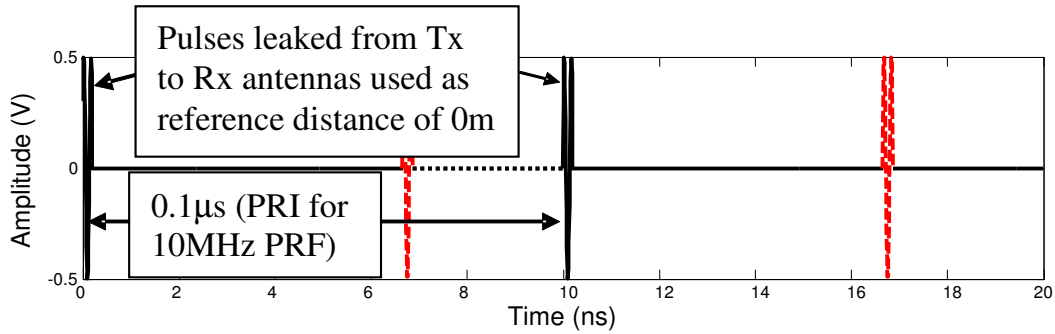


Fig. 4.7 - Received 10MHz PRF pulses of target at 1m.

When the received pulses reach the broadband mixer (c.f. Fig. 4.4), the pulses get cross-correlated in real-time with reference pulses of the assumed same pulse shape for maximum likelihood detection (matched filtering). The time positions of the reference pulses therefore determine the outcome (DC value) of the cross-correlator (mixer IF output). The concept of the mixer cross-correlation is demonstrated in Figs. 4.8 to 4.10. A single received pulse of the target at 1m is input to the RF port; a single reference pulse with its time position aligned at various delays with respect to the RF port pulse is input to the LO port; and the corresponding IF port outputs are shown as an illustration.

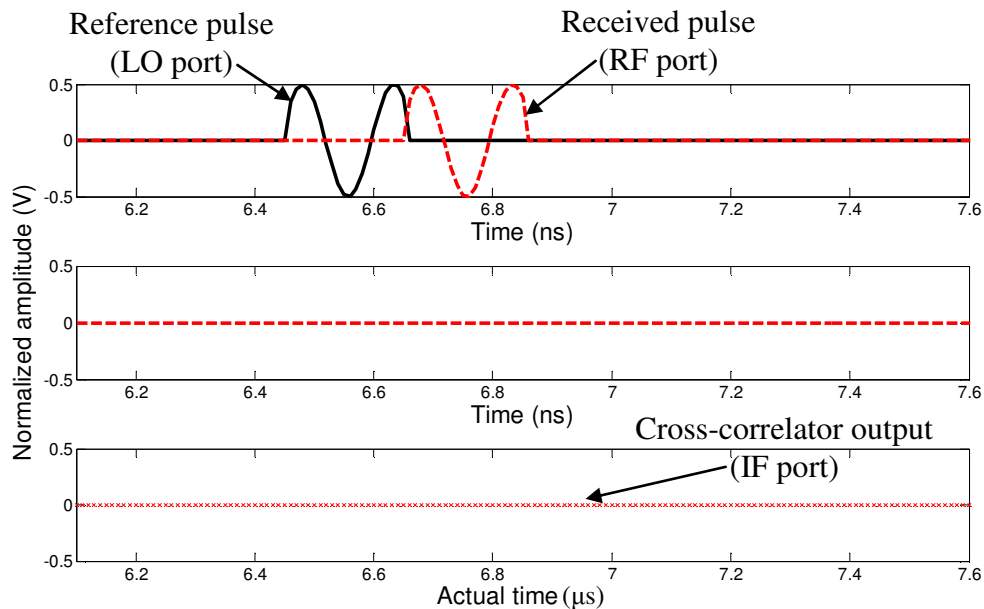


Fig. 4.8 - Non-overlapped reference pulse.

The top graph of Fig. 4.8 shows a situation when the LO reference pulse (black solid line) is not overlapped with the RF input pulse (red dashed line). The red dashed line in the middle graph are the normalized cross-correlated energies for the LO and RF pulses. Since the LO and RF pulses have no overlapping energies, the output at the IF port (instantaneous DC) as depicted by the bottom graph with red crosses is at 0V.

However when the LO pulse is delayed by 100ps with respect to the reference pulse of Fig. 4.8, the overlapping energies between the LO and RF pulses show as the cross-correlation output (middle plot of Fig. 4.9). The IF port output (bottom) is the sum of the cross-correlated energies, and the result is a negative DC value. If we trace the IF output as a function of delay, we find that a replica of the received pulse shape is reproduced with two additional “side-lobes” shown in Fig. 4.10.

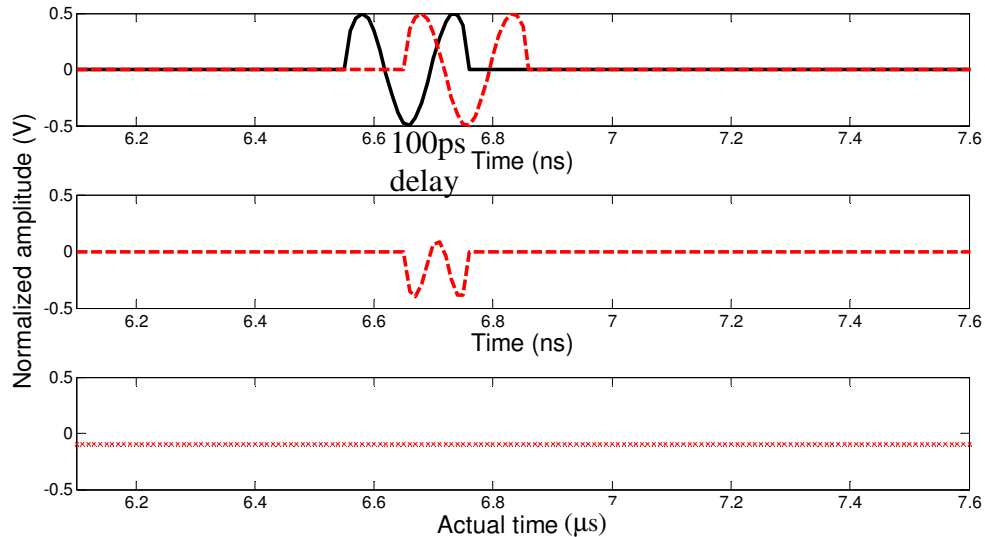


Fig. 4.9 - Reference pulse delayed by 100ps.

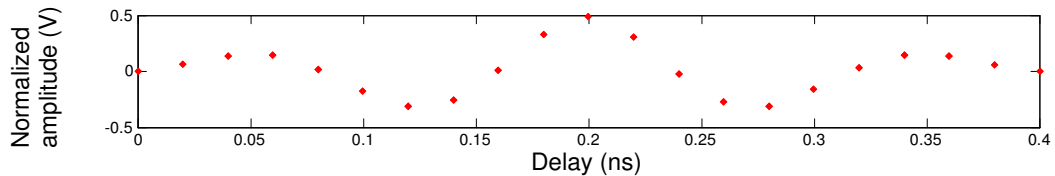


Fig. 4.10 - IF output with respect to delay of reference pulse.

Theoretically, the original pulse shape (e.g. received pulse at RF port) can be reproduced only by an “ideal sampler” using zero-width impulses as the reference pulse (at the LO port). This is shown in Fig. 4.11 where the LO port pulse is a normalized amplitude impulse and the output of the IF port with respect to swept delay showed the RF port image being traced by the Dirac-delta impulse. However impulses are not practical and the broadband mixer (cross-correlator) has a limited frequency response that cannot accommodate impulses. Furthermore, in a matched filtering and pattern recognition perspective, identical pulse shapes for cross-correlation will produce the largest amplitude output. Hence the desired choice of the LO port pulse shape is one that has the same pulse shape as the one received at the RF port.

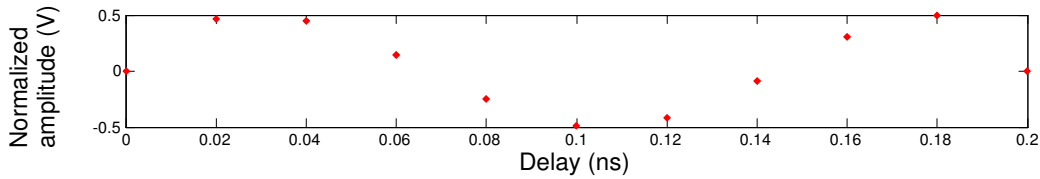


Fig. 4.11 - IF port output with respect to delay of dirac-delta impulse at LO port.

With the concept of cross-correlation that occurs at the mixer stage described, the operation of a pulsed-based radar system can be visualized. A swept delay reference pulse technique can be used to determine the presence of targets at ranges where the IF output (with energy aggregated over multiple PRI via the integrator) exceeds a pre-determined threshold above the system noise floor. This is one way of implementing the UWB radar receiver.

The time-expansion receiver using the same hardware architecture is an alternative method. A time expansion factor has to be determined first, to expand the received pulse-width to fit the ADC bandwidth. An example for expansion factor of 1000, the 200ps pulses can be sampled at 20MSa/s. The time expansion is carried out by applying a slightly lower PRF for the reference pulses at the LO port as compared to the PRF at the RF port. For UWB radar operating at 10MHz PRF, the required PRF for the LO port is determined as follows:

$$T_d = PRI / F \tag{4-2}$$

where T_d is the additional time delay for each consecutive PRI and F is the expansion factor. For PRI of $0.1\mu s$ and F of 1000, T_d is 100ps.

$$PRF_x = \frac{1}{(PRI + T_d)} \quad (4-3)$$

where PRF_x is the time expanded PRF for the LO port. The required PRF_x is 9.99000999MHz.

When the PRF of the LO port is set to 9.99000999MHz, Figs. 4.12 and 4.13 show the output of the integrator for two consecutive PRIs of the RF port after 65 PRIs have elapsed. The integrator output x-axis is the actual time from the start of an expanded time frame (PRI #0), while the x-axis for the top graph containing the LO and RF port pulses are the time offset from the antenna leakage pulse for its respective PRI. Because the PRF of the LO port is set lower than the RF port, the LO pulse will be delayed by 100ps with each PRI.

When seen for multiple PRIs, the integrator output traces the RF pulse to create an expanded replica as observed in Fig. 4.14. Finer resolution can be obtained with higher expansion factors, but with trade-off of a longer expanded time frame. This is the methodology of the time-expansion mechanism.

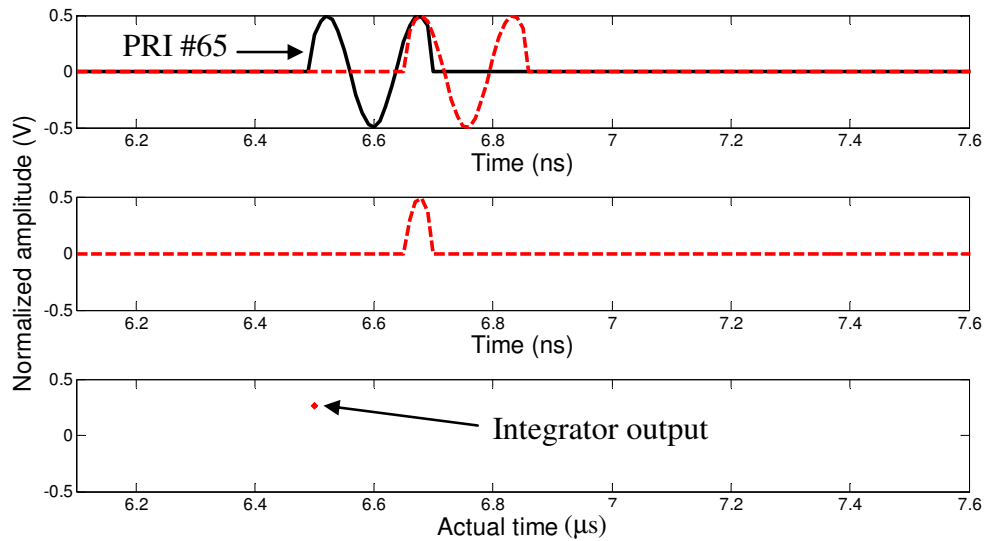


Fig. 4.12 - LO and RF pulses and integrator output at PRI #65.

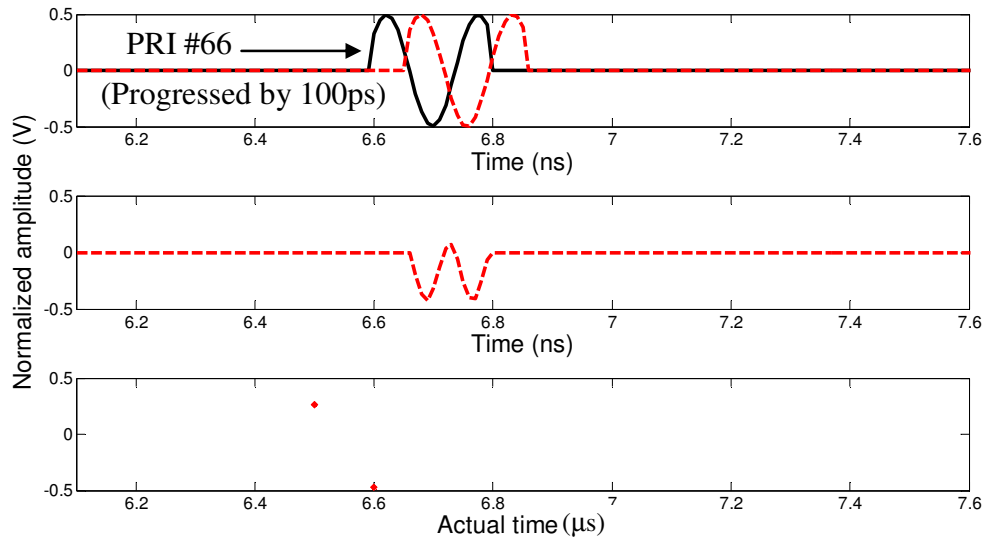


Fig. 4.13 - LO and RF pulses and integrator output at PRI #66.

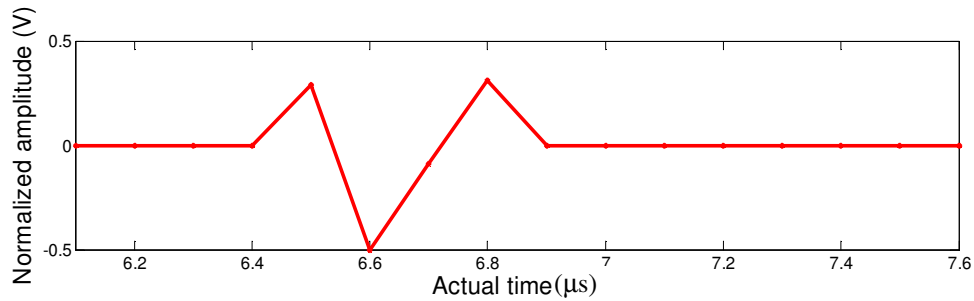


Fig. 4.14 - Interpolated time-expanded waveform from integrator output.

4.3 Circularly polarized antenna

The proposed CP antenna is constructed using an array of four LP dual elliptically tapered antipodal slot antennas (DETASA) [44]. The antenna elements are arranged in a sequential rotation manner with 90° rotations. The DETASA has a lower operating frequency of 2.7GHz. The substrate used for the design is 0.8mm thick Rogers 4003C and size of the antenna is 9cm x 9cm. The sequentially rotated array is fed with the orthogonal pulses output from the proposed feed network introduced in Section 3.3. Two configurations for the arrangement of the LP antenna elements are considered; the “cross” and “box”. The “cross” arrangement has the first element aligned vertically, and for the “box” arrangement aligned horizontally. The arrangements are shown in Fig. 4.15.

For left-hand circularly polarized (LHCP) radiation, the first rotated element (2) is fed with the -90° phase output of the feed network (port 8), and for right-hand circularly polarized (RHCP) radiation $+90^\circ$ output (port 6). The remaining elements are fed with their sequentially rotated phases respectively. LHCP radiation is chosen due to lesser interference from the existing wireless systems within the band. The “cross” arrangement result in an overall size of 18cm x 18cm x 9cm, and the “box” 9cm x 9cm x 9cm.

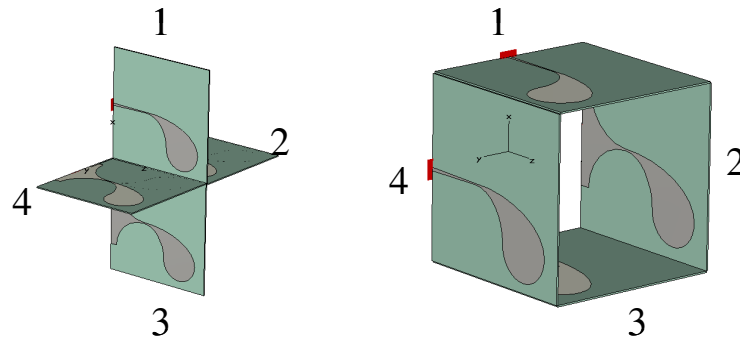


Fig. 4.15 - a) “Cross” structure

b) “Box” structure

Measured return loss of the CP antennas connected to the feed network is shown in Fig. 4.16. The inter-elements coupling did not degrade the return loss of the decade bandwidth feed network.

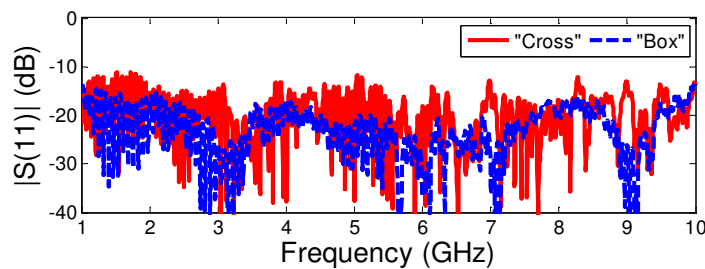


Fig. 4.16 - Return loss of combined feed network and antenna array.

Simulation and measurement results of the two antenna configurations are shown in Fig. 4.17. The “cross” antenna has a 3dB axial ratio bandwidth from 3 to 8.5GHz, and the “box” antenna from 3 to 10GHz. The axial ratio is measured at boresight. Axial ratio beamwidth for the “cross” antenna spans from 8° at 8GHz to 17° at 3GHz, and the “box” antenna from 5° at 10GHz to 14° at 3GHz. Therefore, the proposed CP UWB antenna has

superior axial ratio performance as compared to its counterparts reported in the literature. Discrepancies between simulations and measurements at higher frequencies are due to the lower signal to noise ratios at those frequencies for measurements. The symmetry of the four antenna array structure preserves the axial ratio and maintains polarization purity as compared to a non-symmetrical two antennas sequential rotation CP design.

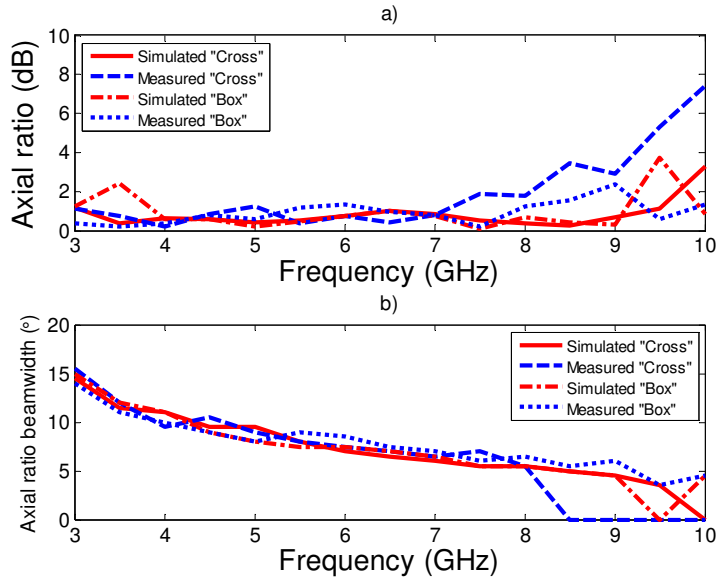


Fig. 4.17 - Axial ratio performance of the CP antenna.

4.4 Vital signs monitoring application

A photograph of the implemented proposed CP UWB radar system is shown in Fig. 4.18.

The sampled signals have a 40ms frame rate due to time expansion. The peak voltage of each frame is recorded and accumulated for 20s. Multiple targets captured by the same radar unit (within antenna beamwidth) can be discriminated from individual voltage peaks at different time delays (due to the time-of-arrival of different target distances for pulse radar), and each target's corresponding voltage peak tracked separately. During the rolling 20s period, movements from the chest and heart are captured as amplitude variations of the recorded peak voltages. The movements correspond to positional change of the body and time-varying RCS that cause phase change [84] of the reflected pulse with respect to the reference pulse, therefore causing

the peak voltage of each frame to change accordingly. A fast Fourier transform (FFT) is performed on the rolling 20s period to derive its spectral content. A sample spectral and time-domain plot of the signal processing software for one target is shown in Fig. 4.19. The bottom graph shows the rolling 20s collected peak voltages versus time, and the graph above is its frequency spectrum. The time-domain plot contains both the breathing and heart beat signals, which are difficult to separate. However in the frequency domain, as the heartbeat is usually higher than breathing rates, the signals are separated using band pass filtering. Harmonic cancellation of the breath signal [72] can further reduce noise in heart beat rate prediction. The amplitude difference between the two signals is due to the movement of the chest cavity during breathing being larger than the movement for heart beating [85]. The peak in the frequency spectrum shown in Fig. 4.19 at 0.15Hz corresponds to the breathing rate and the smaller peaks at 0.45Hz and 0.7Hz are its odd harmonics (the breathing waveform is like a triangle wave). Thresholds of 10dB above the noise floor (no targets) are used to determine the breathing and heart beat rates. The heart beat signal is the peak at 0.95Hz and its third harmonic is visible at 2.8Hz. Upper and lower limits of the breathing and heart beat rates can be set as threshold for generating alarms.



Fig. 4.18 - Photograph of CP UWB radar system for vital signs monitoring.

Through visual inspection, the breathing rate measured by the radar system is found to be 100% accurate; comparing the voltage waveform as the chest rises and falls. For

heart beat rates, when compared to an electrode based heart beat sensor, the accuracy is determined to be within +/- 2 beats per minute.

Table 4.1 gives the vital signs measurements for combinations of human orientation and radar polarization conducted with three trials (averaged) over a period of ten minutes for one test subject. F represents the person standing with the front facing radar and S for side facing the radar. LPH represents linearly polarized antennas horizontally oriented and CP represents circularly polarized. Horizontal (LPH) polarization is chosen for the experiment to depict the worst case scenario where the person's orientation is not matched to the antenna's polarization. For LPH, the Vivaldi antennas are placed in a horizontal alignment for both the transmit and receive antennas. In the user scenario, the radar should operate regardless of person's orientation. The heart beat rate of the person at the time of test is 55 beats per minute. For the F-LPH measurement, the breathing rate is accurate, but the heart beat rate is noisy due to fading RCS. The S-LPH combination shows no reception, due to cross-polarization and minimal RCS. When CP antenna is used for the human orientation in either the front (F) or side (S), the breathing and heart beat rates show more accurate results.

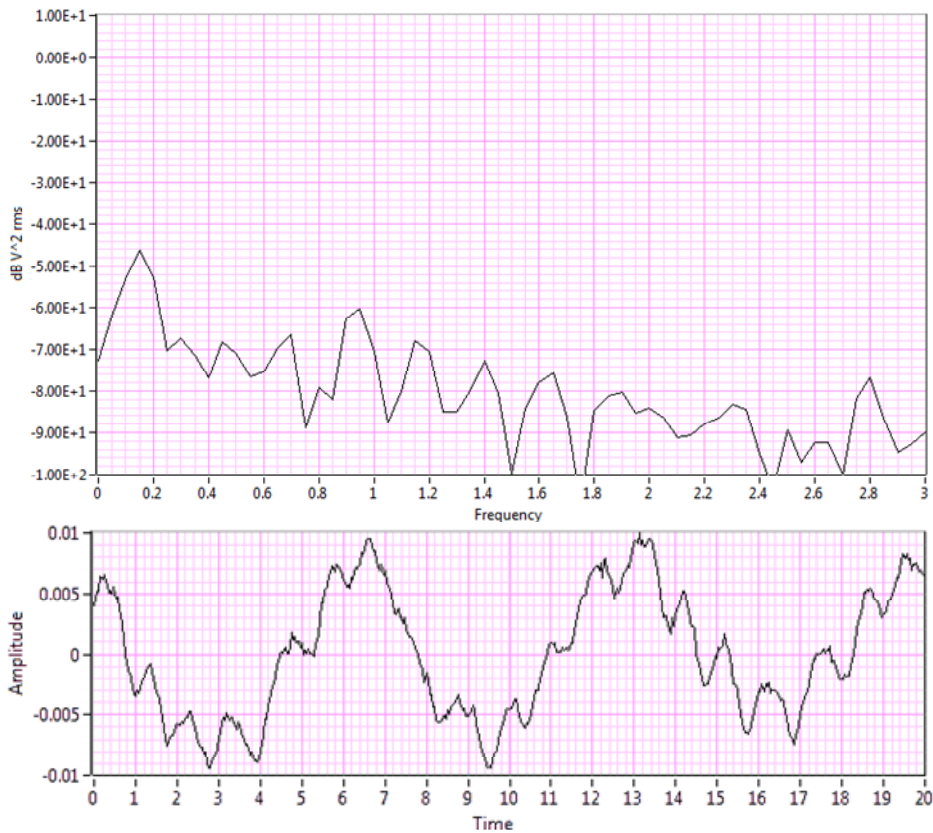


Fig. 4.19 - Spectral and time-domain plots of radar system measurements.

Table 4.1
System measurements of various polarization configurations

Human orientation - Radar polarization	Breaths (per min.)	Heart beats (per min.)
F - LPH	12	42
S - LPH	0	0
F - CP	12	54
S - CP	12	57

Table 4.2 summarizes the comparison between the various radar designs for vital signs monitoring.

Table 4.2
Comparison of radars for vital signs monitoring

Reference	Radar type	Frequency of operation	Detection distance	Polarization	Imaging capability
This work	UWB	3-10GHz	3m	Circular	Yes
[71]	UWB	3.1-10.6GHz	Not stated	Linear	Yes
[72]	UWB	3.1-10.6GHz	1m	Linear	Yes
[74]	Doppler	2.4GHz	4m	Linear	No
[75]	Doppler	5.8GHz	>2m	Linear	No
[76]	Doppler	2.46GHz & 2.51GHz	0.5m	Circular	No

The CP UWB radar system is more robust in vital signs monitoring as compared to its linearly polarized counterpart. The goal of robust contactless vital signs monitoring has been achieved.

The following chapter will describe the use of the same time domain radar system being extended to material characterization applications that enables fat localization and identification.

Chapter 5

Dielectric material characterization using time domain RCS: A feasibility study for fat characterization

Dielectric materials are characterized by their relative permittivity and loss tangent at various frequencies. These parameters can be measured using either destructive or non-destructive methods. The measurement procedure involves different technologies depending on sample dimensions, frequency bandwidth and applications [86]. Examples of material characterization methods include (i) transmission line based methods: implemented in planar technology, namely microstrip [87, 88], stripline [89] and coplanar waveguide [90], or waveguide structures such as co-axial [91, 92] and metallic transmission waveguide [93] (ii) open ended co-axial probe methods [94-96] (iii) resonant cavity based methods [97, 98] (iv) free space methods [37, 99-100]. Each of these methods has its merits and limitations, for example resonant cavity based method provides accurate measurements; however the measurements are narrow band and the sample needs to be shaped.

Industrial applications of material characterization are for the measurement of the dielectric constant for high frequency printed circuit board substrate material [101], the quality assurance of food products [102], the scanning of road surfaces for vehicular safety [103] and human tissue characterization for tumor detection [104] to name a few. An accurate, broadband, non-contact and non-destructive method is desired for rapid measurement and convenience. The free space material characterization methods can be developed through analytical [105, 106] or numerical techniques [107]. Network analysis and parametric estimation are required in the free space methods. This thesis proposes a new non-contact method for free space material characterization that does not require

Portions of this chapter have been published in reference [9]

network analysis, parametric estimation, or sample preparation. The proposed method uses time domain radar measurements as the basis for material characterization.

Time domain radar cross section (RCS) has been investigated in [108] for the characterization of the pulse shapes for metallic plates and synthesized material to identify objects. The pulse shape for boresight illumination has a correlation to the object shape and material property. Therefore, the reflected pulse contains information regarding the electrical property of the material. Comparing the boresight reflected pulse from an object with that of a metal plate as a reference, the material characteristics of the object can be extracted. The proposed method is non-contact and only requires the metal plate standard for calibration. This method has the ability to measure the relative permittivity of arbitrarily shaped objects provided the RCS of a metal object with the same shape is known. This method can be easily adopted to measure the dielectric constant of internal organs, analyze different fat conditions, and localization of body fat. The measurement procedure is simple that requires no special skills to operate the sensor. The material characteristic extraction algorithm can be automated to allow real-time operation. The signal processing methodology uses only basic mathematical functions and integration or Fourier transform to achieve the solution.

5.1 Methodology

5.1.1 Theory

The approach of the proposed method of material characterization is to exploit the relationship between the radar cross section (RCS) and the reflection coefficient of a material under test (MUT). A solution to the monostatic RCS of an arbitrary shaped dielectric object with respect to its reflection coefficient is stated as:

$$\sigma_{MUT} = \sigma_{\infty} |\Gamma_{MUT}|^2 \quad (5-1)$$

where σ_{MUT} is the RCS of the MUT, σ_{∞} is the physical optics (P.O.) approximated RCS [85, 109] of a perfectly conducting object with the same shape and size as the MUT, and Γ_{MUT} is the reflection coefficient of the MUT. For radar measurements,

$$\Gamma_{MUT} = \frac{\eta_{MUT} - \eta_x}{\eta_{MUT} + \eta_x} \quad (5-2)$$

where η_{MUT} and η_x is the intrinsic impedance of the MUT and the medium prior to the MUT respectively. For non-magnetic objects (i.e. $\mu_r=1$),

$$\eta = \frac{\eta_0}{\sqrt{\epsilon_r}} \quad (5-3)$$

where η_0 is the intrinsic impedance of free space ($\sim 377\Omega$), and ϵ_r is the relative permittivity of the MUT.

To obtain the RCS of an object using time domain measurements, a frequency averaged RCS is defined as [110]:

$$\sigma_{avg} = \frac{\int_{-\infty}^{\infty} |r(t)|^2 dt}{\int_{-\infty}^{\infty} |s(t)|^2 dt} \cdot \frac{(4\pi R^2)^2}{h_{et} \cdot h_{er}} \quad (5-4)$$

where $r(t)$ is the received pulse at the receiving antenna, $s(t)$ is the transmitted pulse fed to the transmitting antenna, R is the distance from the antenna to the MUT, and h_{et} and h_{er} are the effective heights [9] of the transmitting and receiving antennas respectively. The effective height of the antenna is defined as the fractional dimension of the maximum aperture size of the antenna based on its broadband radiation efficiency. Therefore, σ_{MUT} and σ_{∞} can be found from measurements using (5-4). σ_{∞} can be measured by covering the arbitrarily shaped MUT with a metal foil that can conform to its contours, and recording its reflected pulse. For a planar MUT, a metal plate can be used to obtain σ_{∞} .

If the reference metal chosen for the σ_{∞} measurement differs in its cross-section dimensions (i.e. area) to the scattering area of the MUT for far-field measurements, a scaling factor using the ratio of the areas can be applied to the received pulse. Therefore the proposed method becomes adaptable to arbitrary object sizes.

After σ_{MUT} and σ_{∞} are acquired, ϵ_r of the MUT can be derived through manipulations of (5-1–5-3) to arrive at

$$\epsilon_r = \left(\frac{1 - \Gamma_{MUT}}{1 + \Gamma_{MUT}} \right)^2 \quad (5-5)$$

where

$$\Gamma_{MUT} = \pm \sqrt{\sigma_{MUT} / \sigma_{\infty}} \quad (5-6)$$

The choice of the sign for Γ_{MUT} depends on the intrinsic impedances of the materials at the interface (from (5-2–5-3)). When the reflected pulse is from a denser to a rarer medium (i.e. $\eta_x < \eta_{MUT}$), the solution will be the positive value and vice versa.

From (5-4–5-6), the relative permittivity of a dielectric material can be derived using time domain measurements.

5.1.2 Procedure

The procedure for broadband material characterization using time domain RCS measurements is as follows:

Step 1, Calibration:

- (a) Measure the source pulse, $s(t)$.
- (b) Place a metal plate of a known size (area A_s) at distance R from the monostatic radar antenna(s). Incident angle of the wave is normal to the metal surface.
- (c) Measure the reflected pulse at the receiving antenna, $r_m(t)$.
- (d) Measure the received pulse, $r_a(t)$, without the metal plate to characterize the clutter and coupled signal between the antennas.
- (e) Calculate the corrected reflected pulse from metal with ambient response removed, $r_{mc}(t) = r_m(t) - r_a(t)$.

Step 2, Determine the size (area) of the MUT:

Using a length measurement tool, determine the area of the MUT, i.e. B_s .

Step 3, Pulse measurement of the MUT:

- (a) Place the MUT at distance R .
- (b) Measure the reflected pulse, $r_{MUT}(t)$.
- (c) Calculate the corrected MUT pulse with the ambient and coupled signal removed, $r_{MUTc}(t) = r_{MUT}(t) - r_a(t)$.

Step 4, Processing:

- (a) Scale the energy of the calibrated metal pulse $r_{mc}(t)$,

$$\int_{-\infty}^{\infty} |r'_{mc}(t)|^2 dt = \frac{B_s}{A_s} \times \int_{-\infty}^{\infty} |r_{mc}(t)|^2 dt$$

- (b) Find the frequency averaged RCS for the scaled metal plate,

$$\sigma_{avg-r'_{mc}(t)} = \frac{\int_{-\infty}^{\infty} |r'_{mc}(t)|^2 dt}{\int_{-\infty}^{\infty} |s(t)|^2 dt} \cdot \frac{(4\pi R^2)^2}{h_{et} \cdot h_{er}}$$

- (c) Find the frequency averaged RCS for the MUT,

$$\sigma_{avg-r_{MUTc}(t)} = \frac{\int_{-\infty}^{\infty} |r_{MUTc}(t)|^2 dt}{\int_{-\infty}^{\infty} |s(t)|^2 dt} \cdot \frac{(4\pi R^2)^2}{h_{et} \cdot h_{er}}$$

(d) Find Γ_{MUT} , (for free space measurements, Γ_{MUT} is negative)

$$\Gamma_{MUT} = -\sqrt{\frac{\sigma_{avg_rMUTc}(t)}{\sigma_{avg_r'_{mc}(t)}}$$

(e) Find ϵ_r ,

$$\epsilon_r = \left(\frac{1 - \Gamma_{MUT}}{1 + \Gamma_{MUT}} \right)^2$$

Only the real part of ϵ_r is obtained as both $\sigma_{avg_r'_{mc}(t)}$ and $\sigma_{avg_rMUTc}(t)$ are real valued quantities.

5.1.3 The case of thin dielectrics

For a time domain radar system, its finite bandwidth will limit the free space range resolution to $r=c/(2 \times BW)$ where c is the speed of light and BW is the 3dB bandwidth of the radar system. For a thin MUT, its reflected pulse contains the reflection from the back surface as well, which needs to be separated from the front surface. Therefore when the frequency averaged RCS of the MUT is computed in step 4(c), the overlapping energies of the combined pulse reflections from both the front and back surfaces will be included in the integration thus causing errors. To mitigate this problem for thin dielectrics, a time gating window can be applied to the pulse of $r_{MUTc}(t)$ to capture the portion of the pulse that does not contain the back surface reflection. The same integration limits have to be applied to $r'_{mc}(t)$ in step 4(b) to maintain consistency in the energy aggregation periods. The minimum thickness of the MUT for these measurements depends on the system bandwidth. As distance R is unchanged in both the $r'_{mc}(t)$ and $r_{MUTc}(t)$ measurements, the pulse position in time domain will be constant. If required, alignment of the pulses to correct for time jitter or imperfections in the radar measurement can be applied. The consequence of time gating the pulse responses will cause the frequency averaged RCS to be lower than the actual RCS. However the proposed method uses the ratio of aggregated energies, thus sufficient accuracy is maintained.

The proposed method is not limited to estimating the real part of the MUT's relative permittivity, but it is also able to derive the frequency responses of ϵ'_r and $\tan \delta$. The following section will describe a modified step 4 (processing) to extract the frequency response of the MUT.

5.1.4 Frequency response of the relative permittivity

The following is carried out in place of the prior step 4 to extract the frequency response of the material's relative permittivity.

- (a) Scale the energy of the calibrated metal pulse $r_{mc}(t)$,

$$|r'_{mc}(t)|^2 = \frac{B}{A} \times |r_{mc}(t)|^2$$

- (b) Obtain the frequency response of the time-gated scaled metal pulse,

$$r'_{mc}(\omega) = FFT(|r'_{mc}(\tau)|^2); \tau \subset t$$

- (c) Obtain the frequency response of the time-gated MUT pulse,

$$r_{MUTc}(\omega) = FFT(|r_{MUTc}(\tau)|^2); \tau \subset t$$

- (d) Find $\Gamma_{MUT}(\omega)$, (for free space measurements, Γ_{MUT} is negative)

$$\Gamma_{MUT}(\omega) = -\sqrt{\frac{r_{MUTc}(\omega)}{r'_{mc}(\omega)}}$$

- (e) Find $\varepsilon_r(\omega)$,

$$\varepsilon_r(\omega) = \varepsilon'_r(\omega) + j\varepsilon''_r(\omega) = \text{real} \left[\frac{1 - \Gamma_{MUT}(\omega)}{1 + \Gamma_{MUT}(\omega)} \right]^2 + j \text{imag} \left[\frac{1 - \Gamma_{MUT}(\omega)}{1 + \Gamma_{MUT}(\omega)} \right]^2$$

- (f) Find $\tan \delta(\omega)$,

$$\tan \delta(\omega) = \frac{\varepsilon''_r(\omega)}{\varepsilon'_r(\omega)}$$

It should be noted that the imaginary part of the fast Fourier transform is related to the shape of the pulse; thus even if the energy of the pulse is taken (e.g. magnitude-squared), the imaginary part of the frequency spectrum is non-zero. Due to different materials with varying losses (with respect to frequency), the scattered pulse amplitudes and shapes of these materials are unique. Therefore the time domain method is able to adequately extract the frequency response of a material's permittivity and loss tangent.

The time gating done in steps (b) and (c) is for capturing the non-overlapped pulse energies of thin dielectrics.

5.1.5 Thickness estimation

Furthermore, by using the time domain measurement method, the thickness of the MUT can be estimated by determining the impulse response of the MUT via deconvolution [71]. The resulting MUT response $r'_{MUTc}(t)$, after deconvolution of the

system transfer function (containing the impulse responses of antennas and cables) and source pulses, is the impulse corresponding to the time delays of the surface reflections. Together with the relative permittivity extracted from the proposed procedure, the material thickness can be derived from the speed of wave propagation in the MUT $v=c/\sqrt{\epsilon_r}$ and the time difference between the impulses of $r'_{MUTc}(t)$.

5.2 Experimental validation

Different dielectric materials with known relative permittivities are used to validate the proposed method. The materials considered for validation are a Granite slab (1ft. x 1ft. x 10mm), a Marble slab (1ft. x 1ft. x 10mm), a Formica laminate sheet (1ft. x 1ft. x 1/8in.) and a Gypsum board (2ft. x 2ft. x 1/2in.). The dielectric constants of these materials are also measured using the free space method and the dielectric probe in [37, 111].

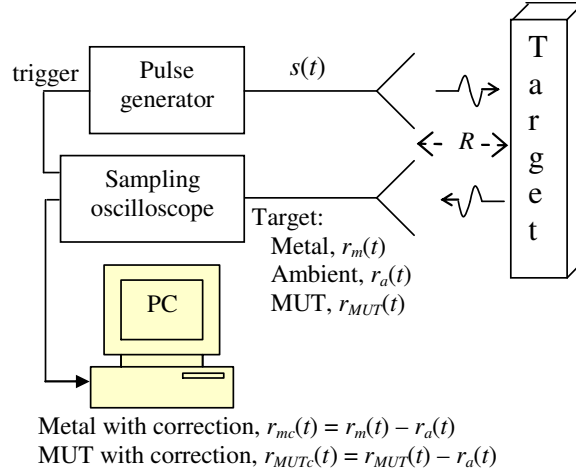


Fig. 5.1 - Experimental validation test set-up.

A block diagram of the test set-up is shown in Fig. 5.1. The source pulse is generated using an AVTECH AVP-3SA-C step generator connected to two Picosecond PSPL 5210 impulse forming network modules in cascade. The pulse generator, as the transmitter, produces 200ps (zero-crossing pulse width) first derivative Gaussian pulses, $s(t)$, at a 1MHz pulse repetition rate and a 1Vp-p amplitude as shown in Fig. 5.2. The transmitter is connected to an antipodal Vivaldi antenna which has a lower operating frequency of 2.7GHz. The effective height of the Vivaldi antenna is 5.6cm. The MUT is placed at distance, R , away from the antenna aperture. Different R values have been

selected for far-field and near-field measurements. The spacing between the identical transmit and receive antenna is 80mm, placed side by side in a mono-static (or quasi-mono-static) radar configuration. The antennas and MUT are elevated at a 1.2m height to de-couple the ground reflections from the received pulses. The receiving antenna is connected to an 18GHz Agilent DCA 86100B sampling oscilloscope being the receiver. The received pulses from the metal (calibration), ambient response and the Granite MUT captured by the receiver are shown in the lower plot of Fig. 5.2. The received pulses of Fig. 5.2 are offset for illustration purposes.

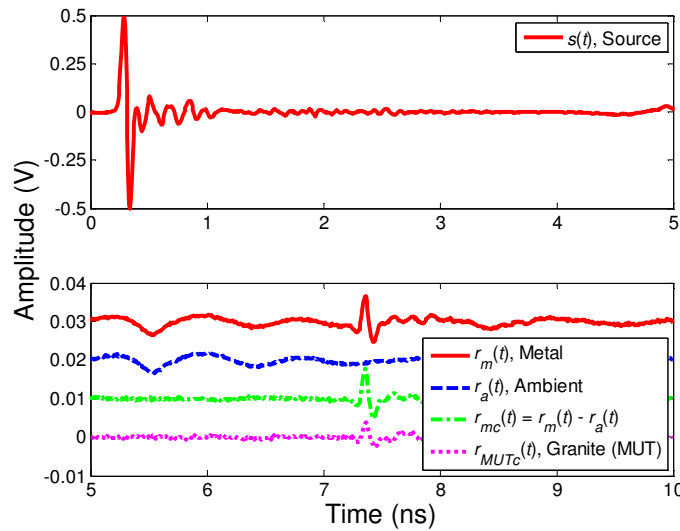


Fig. 5.2 - Transmitted and received pulses for Granite (MUT).

5.2.1 Far-field measurements

The distance R between the antennas and MUT is chosen as 1m. Calibration is done using a 160mm x 160mm (small) and a 300mm x 300mm (big) aluminum plate of 0.5mm thickness to show the scalability of the measurements. Table 5.1 shows the results of the computed ϵ_r using the proposed time domain RCS method for the various MUTs and compared to the mean ϵ_r predicted in [37] for free space measurements and the mean ϵ_r measured using an Agilent 85070E dielectric probe measurement system for a frequency range of 3 to 8GHz. The dielectric probe has a probe model accuracy of 5%. Therefore the probe accuracy in determining ϵ_r is $\pm 0.05 \times \epsilon_r$. The time domain RCS measurements in Table 5.1 are using 148ps time gated pulses as shown in Fig. 5.3 for the Granite MUT as an example. The tail of the MUT pulse is not considered due to the thickness of the

thin dielectric. For a thick MUT, the result is not sensitive to time gate length. Measurements are done at room temperature with one sample for each material. The computed ϵ_r using the proposed method has an average of 24% error as compared to the probe measurements, which is the industry gold standard. The Gypsum board measurement has a higher degree of error (34%) because of poorer signal-to-noise ratio (SNR) as compared to the other MUT; the reflected pulse amplitude is much lower.

Table 5.1
Measured ϵ_r for various MUTs using (5-5)

MUT	ϵ_r w.r.t. small metal	ϵ_r w.r.t. big metal	Mean ϵ_r reported in [37]	Mean ϵ_r using probe [111]
Granite	7.19	7.99	9.76	9.25
Marble	6.65	7.37	9.29	8.63
Formica	4.52	4.90	5.83	4.19
Gypsum	1.44	1.46	2.00	2.18

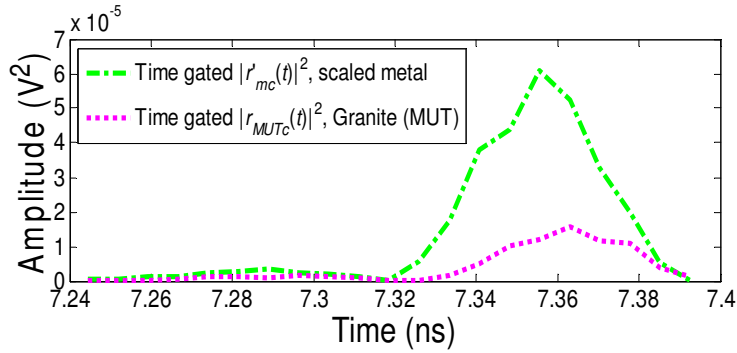


Fig. 5.3 - Time gated pulses for Granite (MUT).

Using the modified processing method, the extracted MUT frequency response is shown in Fig. 5.4 to 5.7 for the Granite slab, Marble slab, Formica laminate sheet and Gypsum board respectively. The same 148ps time-gated pulses are used to compute the frequency averaged RCS for the various MUTs and also determine their frequency responses. The black solid lines are the results of the computations for the measurements done using the big metal plate during calibration, the black dashed lines are for the small metal plate measured during calibration, the red dash-dot lines are for the free-space method presented in [37] and the dotted blue lines are for the dielectric probe measurements shown in [111]. The small metal plate result is included to demonstrate the scalability feature; however its results differ slightly from the big metal plate as some

edge effects become prominent. The mean ϵ'_r of Granite for the big metal plate from 3 to 8GHz is 9.6, Marble is 7.6, Formica is 6.04 and Gypsum is 1.45. Formica has the highest error due to its very thin profile. The computed frequency responses of the various MUT using the proposed method are comparable with the results presented in [37] and dielectric probe measurements [111], therefore verifying the feasibility of the method.

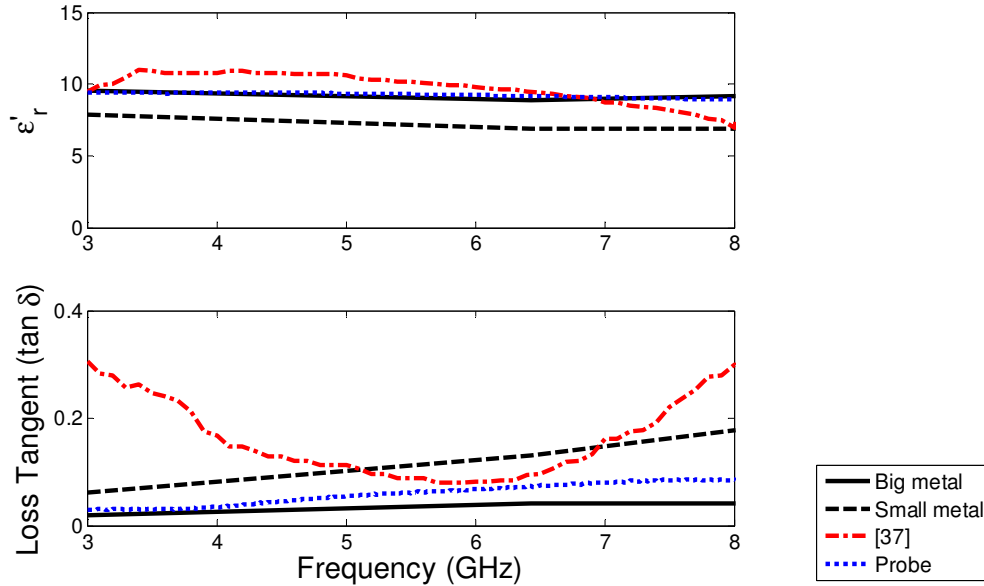


Fig. 5.4 - Material characteristics of Granite slab.

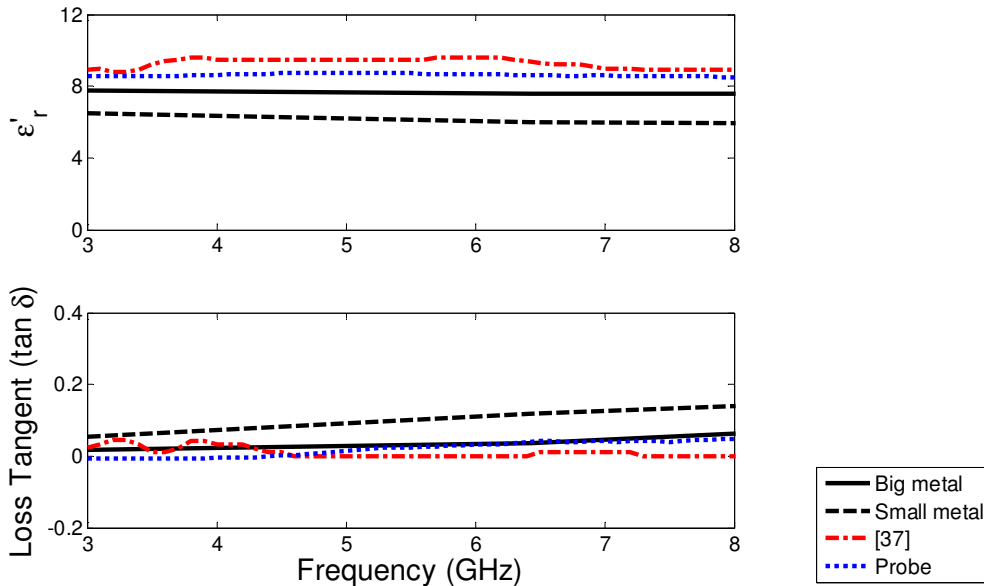


Fig. 5.5 - Material characteristics of Marble slab.

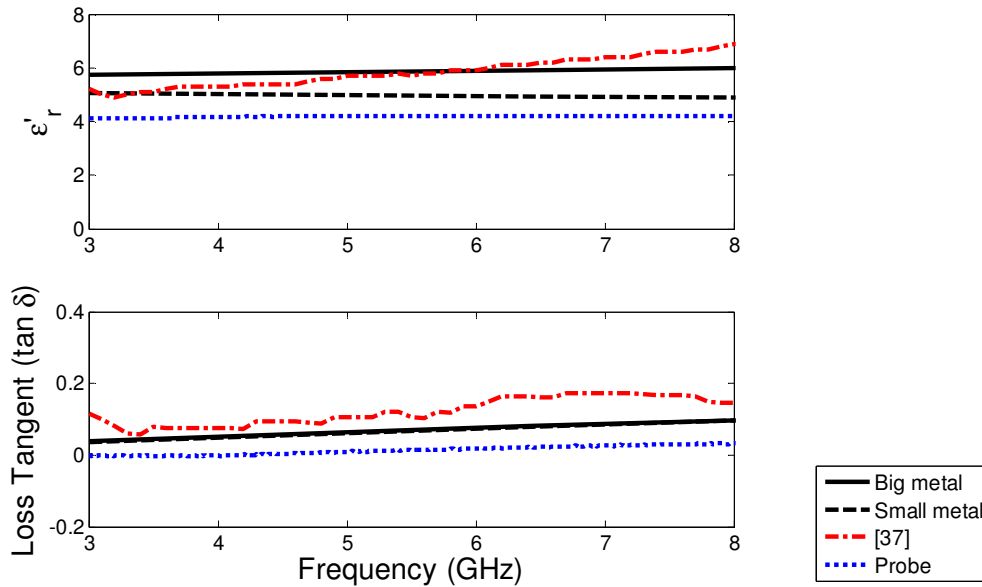


Fig. 5.6 - Material characteristics of Formica laminate sheet.

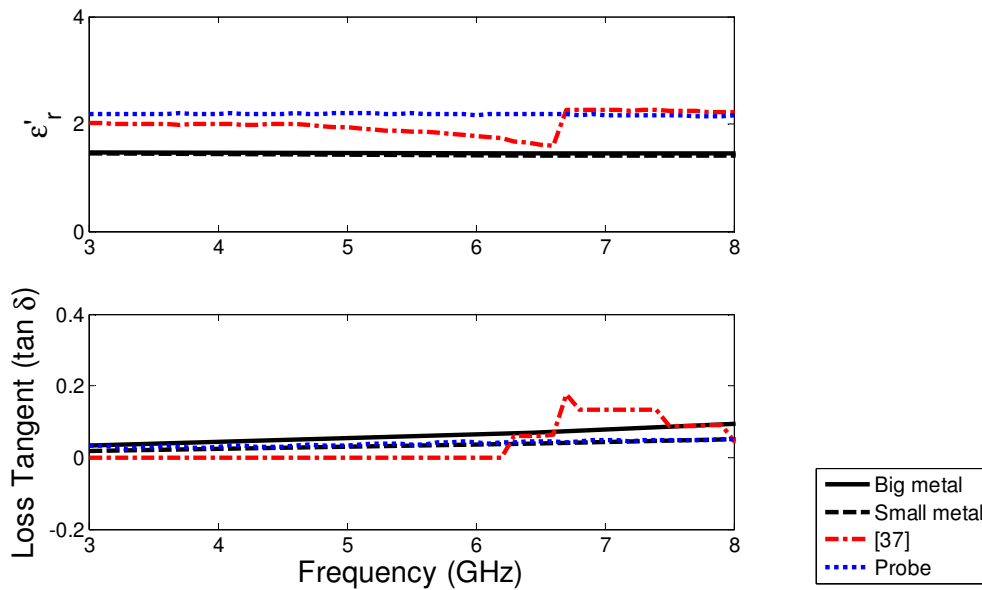


Fig. 5.7 - Material characteristics of Gypsum board.

Fig. 5.8 shows the impulse response, $r'_{MUTc}(t)$, of the Granite slab after deconvolution is applied to remove the system transfer function and source pulse $s(t)$. The reflected pulses from the front and back surfaces of the Granite slab are shown by arrows in Fig. 5.8. The deconvolution is done in the frequency domain and windowing is applied to remove the higher frequency components which have lower signal to noise

ratios. Various window lengths are iterated to estimate the stationary peak and valley locations of the deconvoluted signal. The theoretical thickness resolution (pulse width) is limited by the chosen frequency window length (bandwidth); hence determining its accuracy. The time interval between the peaks of the first and second reflections is 0.215ns. With the computed ϵ_r of the Granite slab being 7.99 taken from Table 5.1, its estimated thickness is 11.4mm computed using the speed of the pulse travelling in the Granite as 1.06×10^8 m/s. Table 5.2 gives the estimated thickness of the various MUTs using the proposed method and compared to the reported thickness in [37] and results of measurements using a Vernier caliper. The accuracy for thickness estimation is within 4mm. Even though the range resolution of the radar system used is around 2cm due to its approximate 10dB bandwidth of 7GHz, the deconvolution method is able to resolve the reflected pulses narrower than the system range resolution because of the sampling oscilloscope's 18GHz bandwidth.

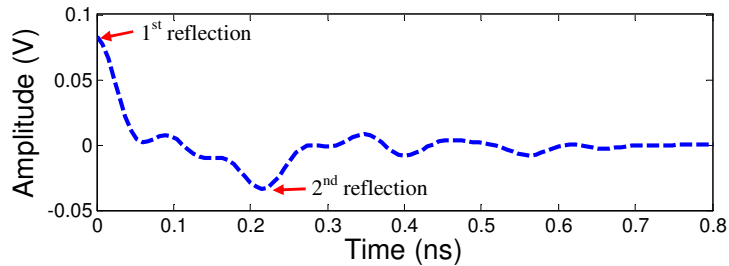


Fig. 5.8 - Impulse response, $r'_{MUTc}(t)$, of the Granite slab.

Table 5.2
MUT thickness measurements

MUT	Proposed method	Reported in [37]	Vernier caliper
Granite	11.4mm	10.0mm	10.34mm
Marble	10.3mm	9.5mm	10.07mm
Formica	3mm	3.7mm	3.22mm
Gypsum	16.5mm	13.0mm	12.86mm

5.2.2 Near-field measurements

RCS is commonly known as a far-field parameter [112], however the proposed method rely on the ratio of the reflected energy from MUT and the metal object used for calibration. Hence this method can be used to accurately measure the relative permittivity of an object in the near-field. Fig. 5.9 shows the geometry of the near-field measurement

configuration. The spacing between the antennas is maintained at 80mm. The Vivaldi antennas used in the experiment have an approximate 90° 3dB beamwidth for both principal planes across the passband. The distance R from the antenna aperture to the MUT is set at 12.5cm. For the MUT used in the experiment and the large metal plate (300mm x 300mm) used for calibration, the overlapping region of the 3dB beamwidths of the antennas at the 12.5cm near-field distance covers an area of around 50cm^2 which does not exceed the area of the object to be measured. The overlapping region of the antenna beamwidths approximates the scattering area for the measurement. Since the scattering area of the measurement is smaller than the object size for both the metal (calibration) and MUT, the area scaling step in the procedure can be omitted. Fig. 5.10 shows the near-field measurement test set-up with the large metal plate used for calibration.

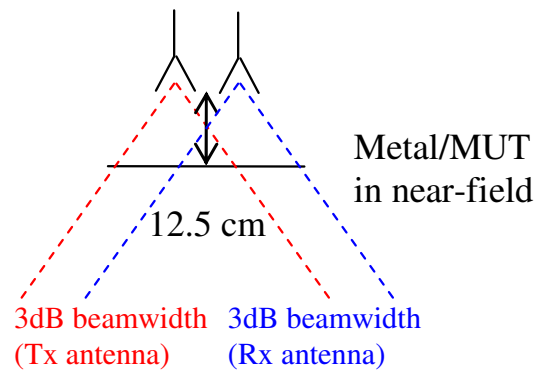


Fig. 5.9 - Geometry of the near-field measurement set-up.

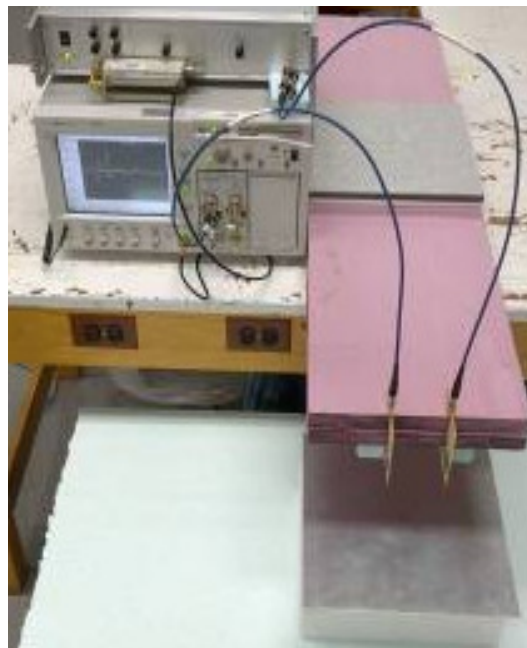


Fig. 5.10 - Near-field measurement with large metal plate used for calibration.

Table 5.3 presents the results for the near-field measurements and compared with the results presented in [37] and the dielectric probe measurements. It can be seen that the accuracy for near-field measurements using the proposed method is improved dramatically. The error between this method and the gold standard is within 3.2%. The MUT frequency response using near-field measurements are given in Fig. 5.11 to 5.14. The proposed method is the black solid line, free space estimation in [37] is the red dash-dot line and dielectric probe measurement is the blue dotted line. The mean ϵ_r of Granite from 3 to 8GHz is 8.75, Marble is 7.59, Formica is 4.08 and Gypsum is 2.37.

Table 5.3
Measured ϵ_r at near-field distance using (5-5)

MUT	Proposed method ϵ_r	Mean ϵ_r in [37]	Mean ϵ_r using probe
Granite	9.40	9.76	9.25
Marble	7.89	9.29	8.63
Formica	4.14	5.83	4.19
Gypsum	2.15	2.00	2.18

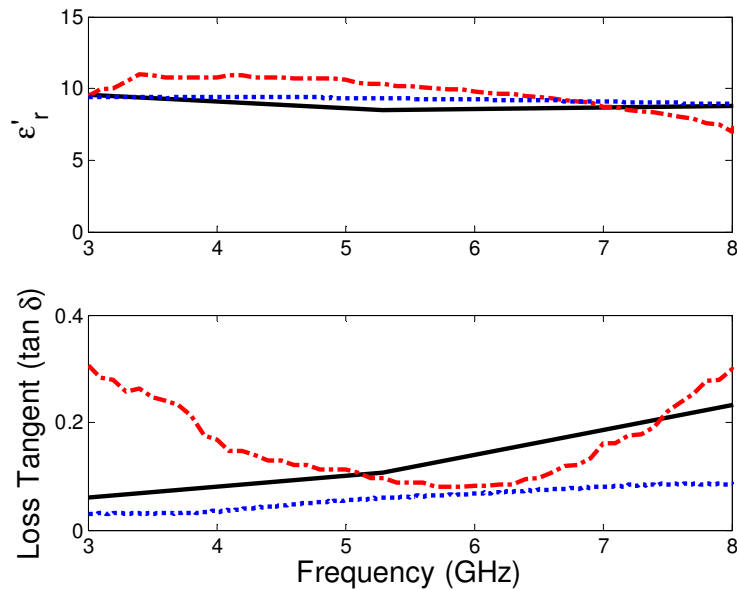


Fig. 5.11 - Material characteristics of Granite slab in near field.

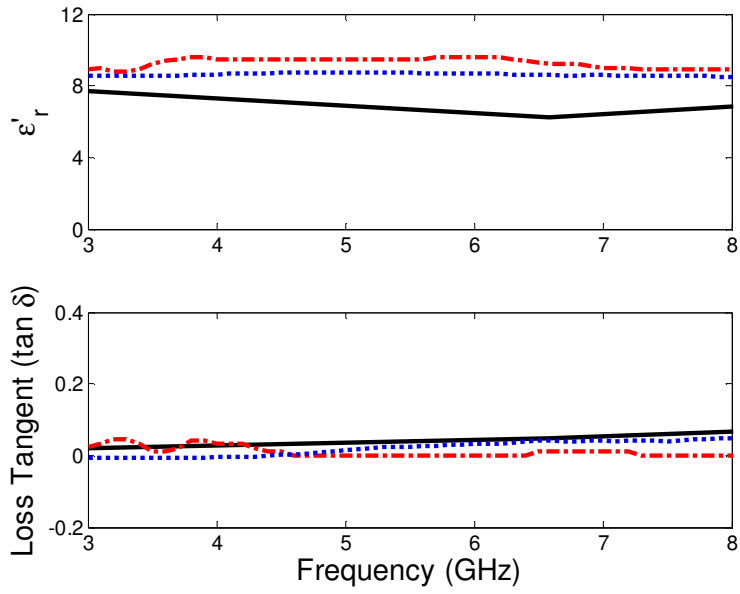


Fig. 5.12 - Material characteristics of Marble slab in near field.

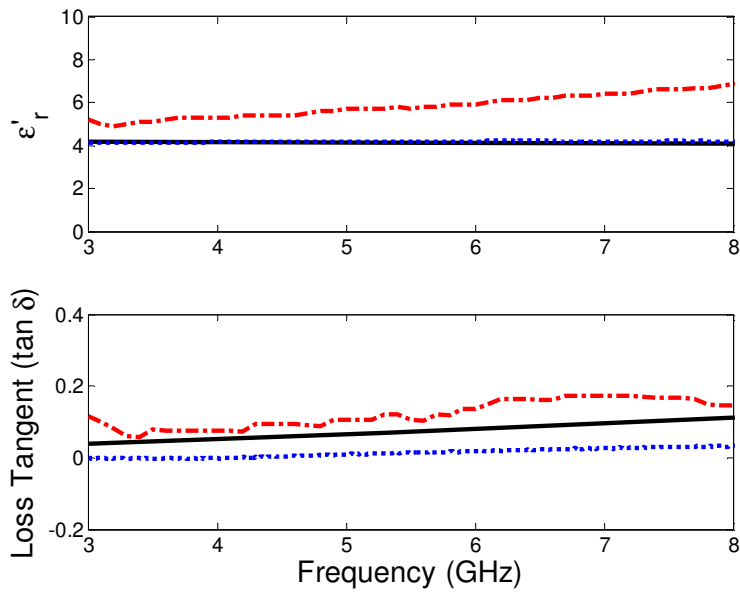


Fig. 5.13 - Material characteristics of Formica sheet in near field.

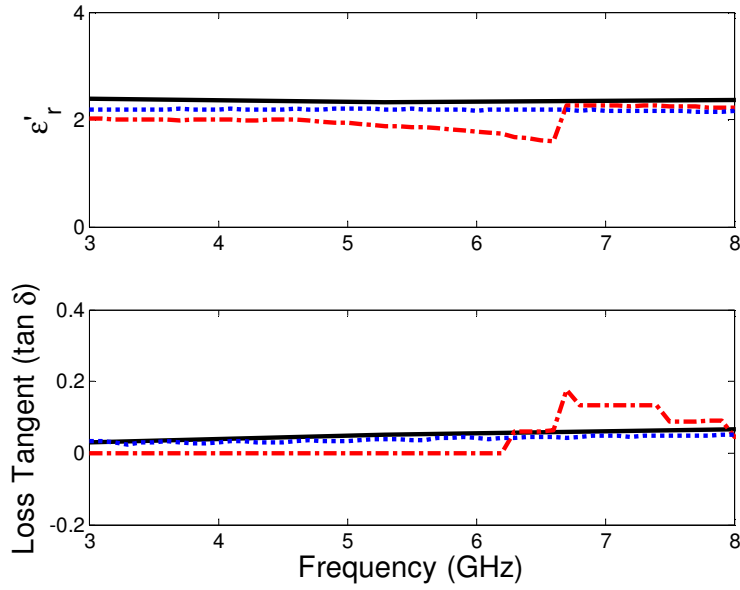


Fig. 5.14 - Material characteristics of Gypsum board in near field.

The MUT thickness estimation using the near-field data is shown in Table 5.4. Accuracy for thickness measurements have improved to less than 2mm error for the near-field measurements.

Table 5.4
MUT thickness using near-field data

MUT	Proposed method	Reported in [37]	Vernier calipers
Granite	10.33mm	10.0mm	10.34mm
Marble	10.09mm	9.5mm	10.07mm
Formica	3.28mm	3.7mm	3.22mm
Gypsum	11.37mm	13.0mm	12.86mm

5.2.3 Multi-layered MUTs

The experiment is conducted for two MUT layers; the Marble slab and Gypsum Board are placed one on top of the other. Near-field measurements are conducted for one combination of the layers and the layer order is swapped and the measurements repeated. Table 5.5 presents the ϵ_r results of the two layer measurements. For obtaining the ϵ_r for the second layer, the following equation is derived:

$$\epsilon_{r_2} = \left[\sqrt{\epsilon_{r_1} \left(\frac{1 - \Gamma_{MUT_2}}{1 + \Gamma_{MUT_2}} \right)} \right]^2 \quad (5-7)$$

Table 5.5
Measured ϵ_r for two MUT layers

$MUT_1 - MUT_2$	ϵ_r of Gypsum	ϵ_r of Marble
Gypsum – Marble	2.50	8.75
Marble – Gypsum	2.46	9.78

(5-7) is derived by substituting the respective layer's intrinsic impedances into (5-2) and solving for ϵ_{r_2} in (5-5).

5.3 Application

Obesity in humans and most animals does not depend on body weight, but on the amount of body fat or adipose tissue. Adipose tissues are of two types (i) white adipose tissue or white fat (ii) brown adipose tissue or brown fat. The main role of white adipose tissue is energy storage whereas brown adipose tissue is to generate body heat. Brown adipose tissue contains a higher amount of iron containing mitochondria, and more capillaries than white adipose tissue. Hence, electrical properties such as dielectric constant and loss tangent of the white and brown adipose tissue differ from each other. Abdominal obesity is related to metabolic disorders, hypertension, and an increased frequency of mortality and cardiovascular diseases [113]. In recent years, intra-abdominal visceral fat, especially white adipose tissue accumulation has been suggested as playing an important and etiologic role in cardiovascular diseases. Therefore the identification of visceral fat areas, thickness and volume of the fat is very important for obesity studies. Identification of white adipose tissue and computation of its percentage in total fat are very crucial for the success of obesity studies. Apart from anthropometric measurements, the current techniques for the assessment of intra-abdominal fat and the estimation of volume of adipose tissue are computed using tomography [114, 115], ultrasonography [116], and magnetic resonance imaging [117]. However, these methods are either too simple and inaccurate or expensive and time consuming.

Due to the fact that human fat and muscle have different dielectric properties [118], intra-abdominal visceral fat locations will be identified by profiling the dielectric constant of the abdominal area. The validated procedure is used for relative permittivity measurements to determine the location and thickness of intra-abdominal visceral fat.

The test set-up for the feasibility study of fat characterization is composed of a phantom model of similar biological materials as the human fat and muscle. Fat and meat

pieces of porcine parts from a local butcher shop simulate the similar human tissues [119, 120], thus forming the phantom. The test set-up for fat localization and characterization using porcine parts is shown in Fig. 5.15. A test sample with two distinct regions, namely fat and flesh, have physical dimensions of approximately 27cm x 10cm x 5.5cm for the fat region and 22cm x 14cm x 5.5cm for the flesh region. A grid of 2cm resolution is constructed over the surface of the phantom model and drawn on a Glad wrap (thin transparent plastic sheet). The grid maps the entire phantom into an area measuring 20cm x 24cm. Each intersection of the grid is a measurement point. The phantom is measured at room temperature within an hour after removing from refrigeration, and the duration of measurement is around two hours. Therefore degradation of the material is not significant.

A metal plate is first placed above the phantom's surface and a measurement is taken at the center of the metal plate as the calibration step. The measurements at each grid point of the phantom, aligned using a laser pointer, are then recorded.

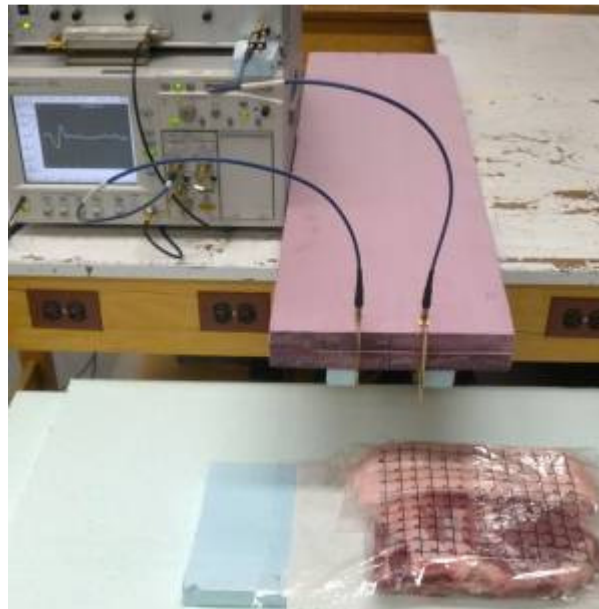


Fig. 5.15 - Test set-up for fat localization using phantom model (porcine tissue).

The processed data for mapping the regions of the phantom is shown in Fig. 5.16. The plot on the bottom of the phantom in Fig. 5.16 shows the side profile of the ϵ'_r versus position. It can be seen that the specific regions are clearly distinguished, the fat region having five grid spaces which corresponds to the actual phantom dimensions. The predicted ϵ'_r of the fat taken at the center of the fat region is 4.03. The dielectric probe

average ϵ'_r , measured over five sample points is 3.77, however the reported ϵ'_r of porcine fat tissue is ~ 7 at 5GHz [121]. The right plot in Fig. 5.16 shows the front profile of the phantom measurements predicting the ϵ'_r of the flesh region to be 45.3 taken at the center of the flesh region. This is comparable to the reported ϵ'_r of porcine muscle tissue of ~ 47 at 5GHz [121]. The ϵ'_r of the flesh region rolls off toward the edge because the scattering area at the edge includes the air around it. Thus an effective ϵ'_r is measured for the points at the edge. The estimated fat thickness from the measurement is 5cm; it should be noted that there are air gaps between the layers of fat material. The second pulse reflection from the flesh layer is not measurable as the material is too lossy, therefore the thickness for the flesh layer cannot be determined from measurements.

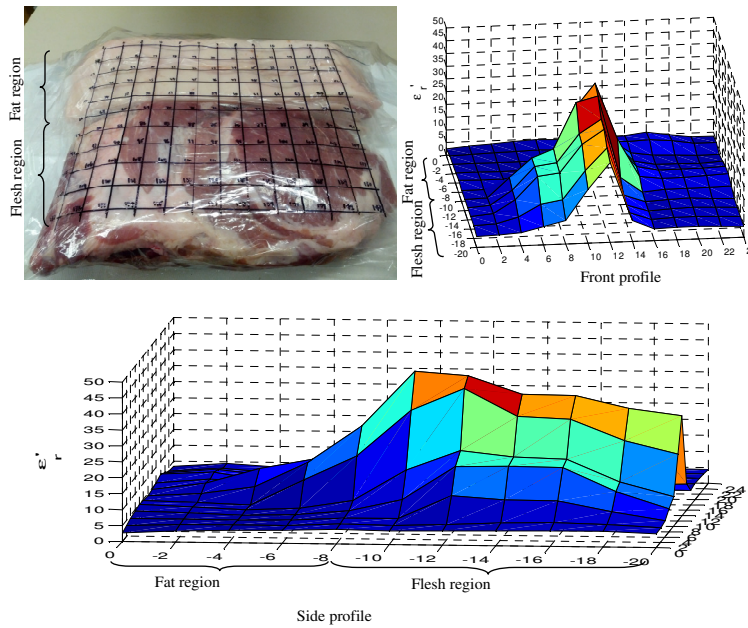


Fig. 5.16 - ϵ_r mapping of the pig's fat and flesh measurements.

5.4 Circularly polarized material characterization

The proposed methodology of using time domain RCS for material characterization is presented for a linearly polarized (LP) radar system. The ratio of the RCS between the dielectric target and metal target of same shape is polarization insensitive [109]. That is the ratio of RCS will be the same for both vertical and horizontal polarization when linear polarization is used. However the method can be extended to a circularly polarized (CP)

radar system. It is a known fact that the sense of circular polarization will be flipped for metal targets scattering. Therefore during the calibration procedure, the opposite CP receiver needs to be used. This can be easily achieved by our proposed radar system through the extraction of the cross-polarized signal from the isolated port of the feed network design. The advantage of using CP over an LP system is having a larger signal-to-noise ratio due to more energy received regardless of the orientation of object. The procedure for CP material characterization is largely the same as the method outlined for the LP case, except for the modified calibration step where an opposite CP receiver is used.

The advantages of the proposed method are (i) there is no need for sample preparation, (ii) easy to calibrate, (iii) works for arbitrary shape, (iv) can also estimate material thickness, and (v) it can easily be automated.

The developed CP UWB radar system can be improved further from the research that has been completed and reported. The next chapter lists some of the opportunities.

Chapter 6

Future work

6.1 Single circularly polarized antenna array radar system

Using the feed network presented in Section 3.3, a study is performed to measure the scattered pulse from a metal sheet (2 feet x 1 feet dimensions) placed at 1m distance away from a circularly polarized (CP) antenna array connected to a network analyzer. The test set-up is shown in Fig. 6.1. Port 1 of the network analyzer is fed to port 1 (0°) of the feed network, and port 2 of the network analyzer is connected to port 3 (90° /isolated port) of the feed network (c.f. Fig. 3.23). This experiment is conducted to investigate the scattered pulse from the metal plate using a single CP antenna array by measuring the pulse outputs from ports 1 and 3 of the feed network. From theoretical analysis, it is known that a co-polarized received pulse will be routed through port 1 of the feed network and cross-polarized through port 3. The CP antenna array is set-up for left-handed circularly polarized (LHCP) transmission; thus co-polarized reception will be LHCP and cross-polarized is right-handed circularly polarized (RHCP).

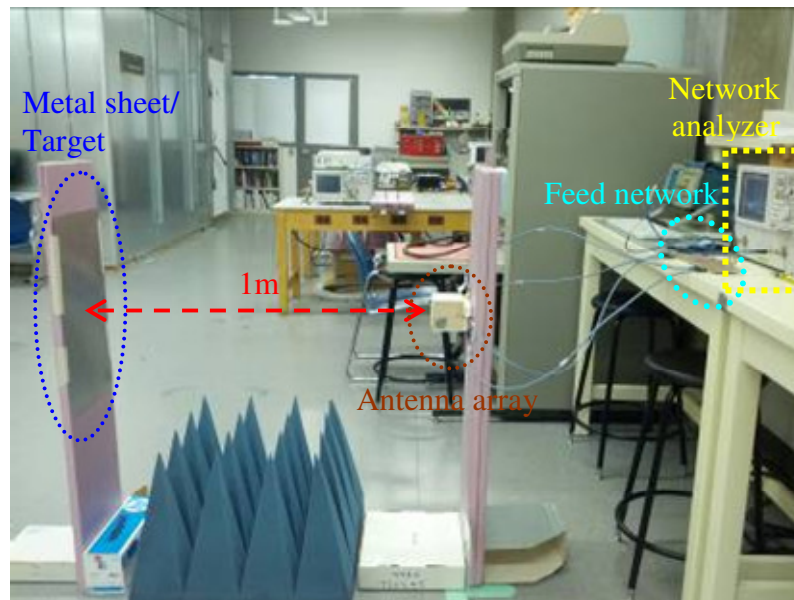


Fig. 6.1 - Test set-up for single circularly polarized antenna array radar system.

Fig. 6.2 shows the pulses recorded at ports 1 (S_{11}) and 3 (S_{21}) of the feed network. The pulses are obtained through inverse fast Fourier Transform (IFFT) of the respective scattered signals. The amplitude of the output pulse from port 3 of the feed network is about two times that of the output pulse from port 1. Therefore, it shows that the scattered energy for cross-polarization is greater than co-polarization for metallic targets in a CP radar system. From the above experiment, it is demonstrated that the proposed feed network design allows for a single CP antenna radar system. For the single CP antenna array arrangement, the transmitter will be connected to port 1 of the feed network and the receiver attached to port 3.

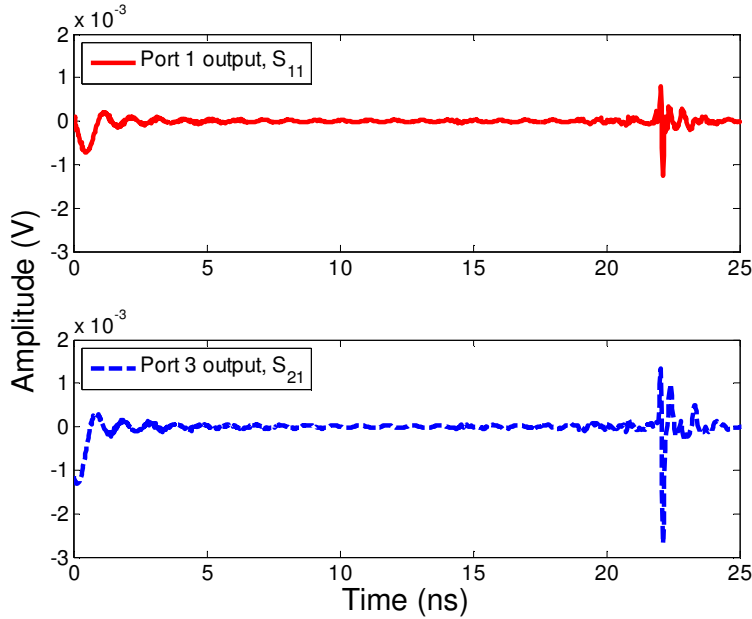


Fig. 6.2 - Pulses recorded at ports 1 (S_{11}) and 3 (S_{21}) of the feed network.

The resulting single antenna mono-static CP radar system will be considerably smaller because the second antenna array for reception is not required. Moreover in the implementation of the single antenna configuration, the mutual coupling effects between transmit and receive antenna will not be present. Additionally, the phase centre for the antenna is maintained for both transmit and receive modes in the system.

The future work can focus on building the single CP antenna array radar system and compare its performance with the two antenna system; analysis of pulse distortion with respect to the angle of arrival can be compared between the single and antenna pair

system configurations. Furthermore, the range accuracy improvement can be analyzed due to the common phase centre for transmit and receive modes in the single antenna case. Application of the single antenna system can be investigated to evaluate its performance in material characterization using the time domain RCS method proposed in this thesis in Chapter 5.

6.2 Characterization of internal organs

Using the proposed method of material characterization with time-domain RCS measurements, the study of health condition of internal organs relating to its relative permittivity can be enabled. Through the literature survey of published scientific information regarding the anatomical geometry and composition of typical internal organs such as the heart (i.e. identifying the size and shape factors), a phantom of the heart can be modeled and created. For example, the typical heart's size is about 8-9cm in diameter [122] and has a general pyramidal shape. The heart's internal chambers are made up of the left and right atriums and ventricles occupying an approximate total volume of 200ml [123]. The above information can be used in building the physical phantom model. The modeled phantom can be covered with aluminum foil on its surface to emulate its metallic equivalent. The perfectly conducting phantom heart will be used in the calibration step as outlined in the proposed procedure of Section 5.1.2. With this calibration data, a patient's heart can be characterized in terms of relative permittivity using our proposed methodology.

Various patients having different heart conditions can be studied through radar measurements to establish the correlation of heart ailment to its relative permittivity. From the measurement data, it is possible to identify and locate any fat depositions around the heart which can help in diagnosis. Another application is in the assessment of liver disease amongst alcohol abusers by quantifying the fat in liver tissues and the liver's size [124] while comparing its measurements with healthy liver.

An anticipated challenge for the characterization of internal organs (when the organ is embedded within multiple layers of tissues such as the skin, fat, muscle and bone) is the presence of the above obstructions. The obstructions vary in a three dimensional domain. The transfer function for the obstruction layers of an average person can be modeled and deconvoluted from the measurement to obtain the internal organ's response. Iterative tuning of the transfer function parameters can be done to optimize the accuracy

in determining the internal organ's response. For the difference in size and shape of the internal organs in differing individuals. The typical model is suggested to be used for calibration, and error bounds can be estimated for the size extremities.

6.3 Determining blood oxygen levels in real-time during surgery

An experiment of finding the correlation between blood oxygen levels to relative permittivity using lamb's blood has been carried out. A sample of lamb's blood with oxygenation levels from 0% to 100% in 20% steps is measured using an Agilent dielectric probe system. The blood oxygenation level is controlled by mixing carbon dioxide to 100% oxygenated lamb's blood (obtained from the Department of Agriculture) and monitoring the mixture (after stirring) with a dissolved oxygen meter. The test is done at room temperature with the samples being tested within few minutes after mixing. The lamb's blood is extracted on the same day as the test. Fig. 6.3 shows the results of the measurements done for one trial per sample for the real part of relative permittivity for the various oxygenation percentages, and Fig. 6.4 shows the loss tangent results. From Fig. 6.3, it can be noted from the curves that 60% and 80% oxygenation is not following the trend (slope) as compared to the other curves. This can be due to the inaccuracies when probing the blood samples or difference in mechanism at these levels of oxygenation. If the 60% and 80% curves are not considered momentarily, it can be observed that there is a trend in the loss tangent results to blood oxygenation levels for frequencies below 3GHz. Fig. 6.5 gives a closer view of the loss tangent curves from 1 to 3GHz. The higher the oxygenation level of the blood, the lower is its loss tangent. This trend is congruent with the fact that the presence of oxygen being an insulator will cause the blood to be less conductive [125], and thus have lesser loss.

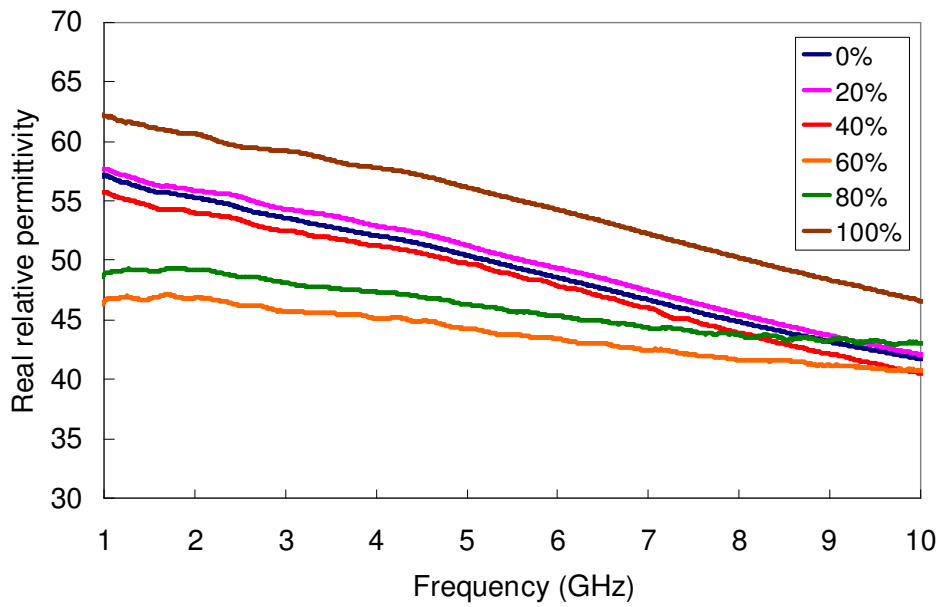


Fig. 6.3 - Relative permittivity of blood at various oxygenation percentages.

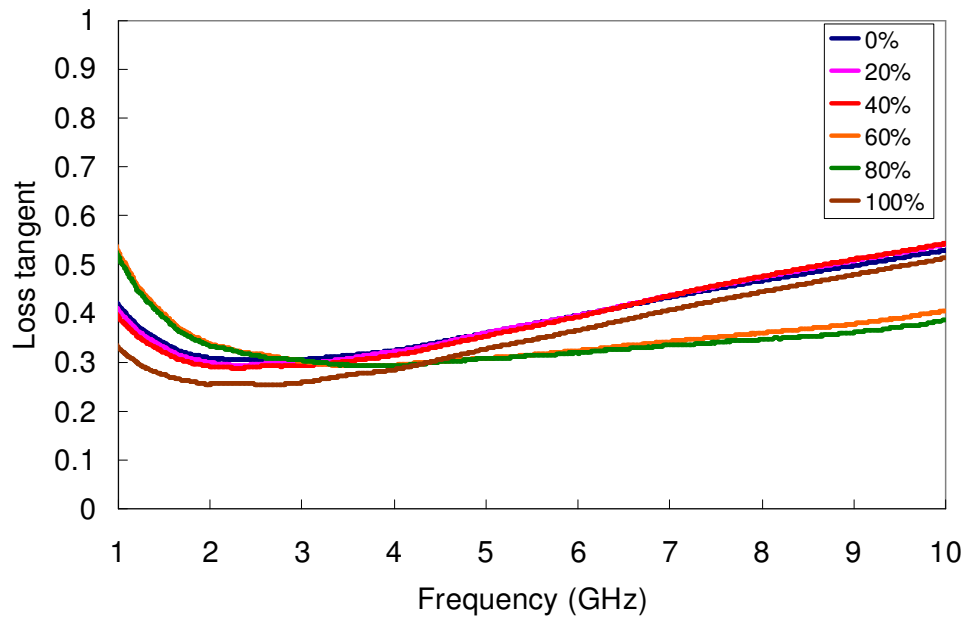


Fig. 6.4 - Loss tangent of blood at various oxygenation percentages.

With this result, a radar system can be designed with frequencies less than 3GHz to track the loss tangent of the organ using the procedure of Section 5 to monitor the blood oxygen level of patients during a surgical procedure. Currently, there is no direct method

of blood oxygen monitoring during a surgery. Pulse oximetry [67], which uses light emitting diodes (LED) and photodiode to probe the blood flow through the capillaries in a finger by measuring the scattered light intensity over time, provides an indirect method of monitoring blood oxygen saturation levels. In the case of open heart surgery, there will be a time lag between the real time blood oxygen level of the central vein to the reading of a pulse oximetry sensor due to the physical distance of the organs. Non-invasive instantaneous monitoring of blood oxygen level of the operated organ can be realized using the radar system. Time critical information from the radar sensor regarding blood volume loss [126] and real time blood oxygenation level of the central vein during surgery becomes available such that blood oxygenation levels above 75% [127] can be maintained to ensure patient stability and prevent mortality.

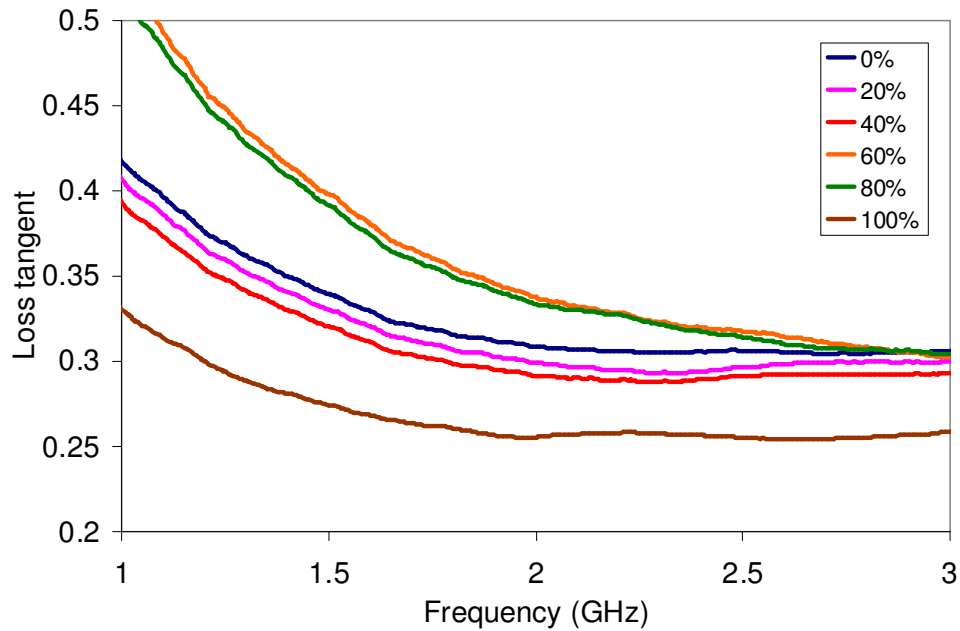


Fig. 6.5 - Loss tangent of oxygenated blood from 1 to 3GHz.

Bibliography

- [1] J. Allen, "Photoplethysmography and its application in clinical physiological measurement," *Physiol. Meas.*, vol. 28, pp. 1–39, 2007.
- [2] A. Droitcour, V. Lubecke, J. Lin, and O. Boric-Lubecke, "A microwave radio for Doppler radar sensing of vital signs," *IEEE MTT-S IMS Digest*, vol. 1, pp. 175-178, 2001.
- [3] J.D. Taylor, *Ultra-Wideband Radar Technology*, New York: CRC Press, 2001.
- [4] M.Z. Win, and R.A. Scholtz, "Impulse radio: how it works," *IEEE Communications Letters*, vol. 2, no. 2, pp. 36-38, Feb. 1998.
- [5] "FCC First Report and Order: In the matter of Revision of Part 15 of the Commission's Rules Regarding Ultra-Wideband Transmission Systems," FCC 02-48, April 2002.
- [6] S. Azevedo, and T.E. McEwan, "Micropower impulse radar," *IEEE Potentials*, vol. 16, no. 2, pp. 15-20, Apr./May 1997.
- [7] M.I. Skolnik, *Radar Handbook*, Third Edition New York: McGraw-Hill, 2008.
- [8] K. Rambabu, A.E.C. Tan, K.K.M. Chan, and M.Y.W. Chia, "Estimation of Antenna Effect on Ultra-Wideband Pulse Shape in Transmission and Reception," *IEEE Trans. Electromagn. Compat.*, vol. 51, no. 3, pp. 604-610, Aug. 2009.
- [9] K. Rambabu, A.E.C. Tan, K.K.M. Chan, and M.Y.W. Chia, "Experimental Verification of Link Loss Analysis for Ultrawideband Systems," *IEEE Trans. Antennas Propag.*, vol. 59, no. 4, pp. 1428- 1432, Apr. 2011.
- [10] C. Gabriel, *A compilation of the dielectric properties of body tissues at RF and microwave frequencies*, Radiofrequency Radiation Division, Brooks AFB, San Antonio, TX, Contract AL/OE-TR-1996-0037, 1996.
- [11] E.M. Staderini, "UWB Radars in Medicine," *IEEE AESS Sys.*, pp. 13–18, Jan. 2002.
- [12] K.K.M. Chan, K. Rambabu, A.E.C. Tan, and M.Y.W. Chia, "Efficient Passive Low-Rate Pulse Generator for Ultra-Wideband Radar," *IET Microwaves, Antennas & Propagation*, vol. 4, no. 12, pp. 2196–2199, Dec. 2010.
- [13] K.K.M. Chan, A.E.C. Tan, and K. Rambabu, "Design and analysis of a Decade Bandwidth 180° Hybrid Coupler," *IET Microwaves, Antennas & Propagation*, vol. 7, no. 1, pp. 71-77, Jan. 2013.

- [14] K.K.M. Chan, A.E.C. Tan, and K. Rambabu, "Decade Bandwidth Circularly Polarized Antenna Array," *IEEE Trans. Antennas Propagat.*, vol. 61, no. 11, pp. 5435-5443, Nov. 2013.
- [15] K.K.M. Chan, A.E.C. Tan, and K. Rambabu, "Circularly Polarized Ultra-Wideband Radar System for Vital Signs Monitoring," *IEEE Trans. Microw. Theory Tech.*, vol. 61, no. 5, pp. 2069-2075, May 2013.
- [16] K.K.M. Chan, A.E.C. Tan, L. Li, and K. Rambabu, "Dielectric Material Characterization using Time Domain RCS: A Feasibility Study for Fat Characterization," submitted to *IEEE Trans. Microw. Theory Tech.* in Aug. 2013 (9 pages).
- [17] B. Hu, and N.C. Beaulieu, "Pulse shapes for ultrawideband communication systems," *IEEE Trans. Wireless Commun.*, vol. 4, pp. 1789-1797, 2005.
- [18] Y. Jeong, S. Jung, and J. Liu, "A CMOS impulse generator for UWB wireless communication systems," *IEEE International Symposium on Circuits and Systems*, vol. 5, pp. IV-129-132, 2004.
- [19] S. Bourdel, Y. Bachelet, J. Gaubert, R. Vauché, O. Fourquin, N. Dehaese, and H. Barthélemy, "A 9-pJ/Pulse 1.42-Vpp OOK CMOS UWB Pulse Generator for the 3.1-10.6-GHz FCC Band", *IEEE Trans. Microw. Theory Tech.*, vol. 58, no. 1, pp. 65-73, Jan. 2010.
- [20] H.M. Rein, and M. Zahn, "Subnanosecond-pulse generator with variable pulsewidth using Avalanche transistors," *Electronics Letters*, vol. 11, no. 1, pp. 21-23, Jan. 1975.
- [21] P. Krishnaswamy, A. Kuthi, P.T. Vernier, and M.A. Gundersen, "Compact Subnanosecond Pulse Generator Using Avalanche Transistors for Cell Electroperturbation Studies," *IEEE Transactions on Dielectrics and Electrical Insulation*, vol. 14, no. 4, pp. 871-877, Aug. 2007.
- [22] M. Miao, and C. Nguyen, "A uniplanar picosecond impulse generator based on MESFET and SRD," *Microwave Optical Technology Letters*, vol. 39, no. 6, pp. 470-472, Dec. 2003.
- [23] H. Hafdallah, A. Ouslimani, R. Adde, G. Vernet, and P. Crozat, "Feasibility of Picosecond Electrical Sampling Using GaAs FET," *IEEE Trans. Instr. Meas.*, vol. 49, no. 1, pp. 172-177, Feb. 2000.
- [24] C.L. Bennett, and G.F. Ross, "Time-domain electromagnetics and its applications," *Proc. IEEE*, vol. 66, pp. 299-318, Mar. 1978.

- [25] "Pulse and waveform generation with step recovery diodes," Hewlett Packard Application Note AN-918, 1968.
- [26] M.J.W. Rodwell, M. Kamegawa, R. Yu, M. Case, E. Carman and K.S. Giboney, "GaAs Nonlinear Transmission Lines for Picosecond Pulse Generation and Millimeter-Wave Sampling," *IEEE Trans. Microw. Theory Tech.*, vol. 39, no. 7, pp. 1194-1204, Jul. 1991.
- [27] D. Salameh, and D. Linton, "Microstrip GaAs Nonlinear Transmission-Line (NLTL) Harmonic and Pulse Generators," *IEEE Trans. Microw. Theory Tech.*, vol. 47, no. 7, pp. 1118-1121, Jul. 1999.
- [28] S. Hamilton, and R. Hall, "Shunt Mode Harmonic Generation Using Step Recovery Diodes," *Microwave Journal*, pp. 69-78, Apr. 1967.
- [29] J.L. Moll, S. Krakauer, and R. Shen, "P-N Junction Charge-Storage Diodes", *Proc. IRE*, vol. 50, no. 1, pp. 43-53, 1962.
- [30] O.P. Falade, M.U. Rehman, Y. Gao, X. Chen, and C. G. Parini, "Single Feed Stacked Patch Circular Polarized Antenna for Triple Band GPS Receivers," *IEEE Trans. Antennas Propag.*, vol. 60, no. 10, pp. 4479-4484, Oct. 2012.
- [31] A. García-Aguilar, J. Inclán-Alonso, L. Vigil-Herrero, J. Fernández-González, and M. Sierra-Pérez, "Low-Profile Dual Circularly Polarized Antenna Array for Satellite Communications in the X Band," *IEEE Trans. Antennas Propag.*, vol. 60, no. 5, pp. 2276-2284, May 2012.
- [32] Y. Hong, J. Kim, S. Jeong, D. Kim, M. Choi, Y. Lee, and J. Yook, "S-Band Dual-Path Dual-Polarized Antenna System for Satellite Digital Audio Radio Service (SDARS) Application," *IEEE Trans. Microwave Theory Tech.*, vol. 54, no. 4, pp. 1569-1575, Apr. 2006.
- [33] J. Bang, C. Bat-Ochir, H. Koh, E. Cha, and B. Ahn, "A Small and Lightweight Antenna for Handheld RFID Reader Applications," *IEEE Antenna Wireless Propag. Letters*, vol. 11, pp. 1076-1079, 2012.
- [34] X.L. Bao, and M.J. Ammann, "Wideband Dual-Frequency Dual-Polarized Dipole-Like Antenna," *IEEE Antenna Wireless Propag. Letters*, vol. 10, pp. 831-834, 2011.
- [35] C. Liu, Y. Guo, X. Bao, and S. Xiao, "60-GHz LTCC Integrated Circularly Polarized Helical Antenna Array," *IEEE Trans. Antennas Propag.*, vol. 60, no. 3, pp. 1329-1335, Mar. 2012.

- [36] I. Nicolaescu, "Improvement of Stepped-Frequency Continuous Wave Ground-Penetrating Radar Cross-Range Resolution," *IEEE Trans. Geosc. Rem. Sens.*, vol. 51, no. 1, pp. 85-92, Jan. 2013.
- [37] L. Li, A.E.-C. Tan, K. Jhamb, and K. Rambabu, "Buried Object Characterization Using Ultra-Wideband Ground Penetrating Radar," *IEEE Trans. Microw. Theory Tech.*, vol. 60, no. 8, pp. 2654-2664, Aug. 2012.
- [38] Nasimuddin, Z.N. Chen, and X. Qing, "Symmetric-Aperture Antenna for Broadband Circular Polarization," *IEEE Trans. Antennas Propag.*, vol. 59, no. 10, pp. 3932-3936, Oct. 2011.
- [39] J. Sze, and W. Chen, "Axial-Ratio-Bandwidth Enhancement of a Microstrip-Line-Fed Circularly Polarized Annular-Ring Slot Antenna," *IEEE Trans. Antennas Propag.*, vol. 59, no. 7, pp. 2450-2456, Jul. 2011.
- [40] K.G. Thomas, and G. Praveen, "A Novel Wideband Circularly Polarized Printed Antenna," *IEEE Trans. Antennas Propag.*, vol. 60, no. 12, pp. 5564 -5570, Dec. 2012.
- [41] M.A. Elmansouri, and D.S. Filipovic, "Low-Dispersion Spiral Antennas," *IEEE Trans. Antennas Propag.*, vol. 60, no. 12, pp. 5522-5530, Dec. 2012.
- [42] S. Mao, J. Yeh, and S. Chen, "Ultrawideband Circularly Polarized Spiral Antenna Using Integrated Balun With Application to Time-Domain Target Detection," *IEEE Trans. Antennas Propag.*, vol. 57, no. 7, pp. 1914-1920, Jul. 2009.
- [43] M.A. Elmansouri, and D.S. Filipovic, "Pulse Distortion and Mitigation Thereof in Spiral Antenna-Based UWB Communication Systems," *IEEE Trans. Antennas Propag.*, vol. 59, no. 10, pp. 3863-3871, Oct. 2011.
- [44] X. Qing, Z.N. Chen, and M.Y.W. Chia, "Dual elliptically tapered antipodal slot antenna loaded by curved terminations for ultrawideband applications," *Radio Science*, vol. 41, 2006.
- [45] E. Wilkinson, "An N-way hybrid power divider," *IRE Trans. Microwave Theory and Tech.*, vol. MTT-8, pp. 116-118, Jan. 1960.
- [46] D.M. Pozar, *Microwave engineering*, second edition, John Wiley & Sons, New York, pp. 401-407, 1999.
- [47] C.H. Ho, L. Fan, and K. Chang, "Broad-band uniplanar hybrid-ring and branch-line couplers," *IEEE Trans. Microw. Theory Tech.*, vol. 41, no. 12, pp. 2116–2125, Dec. 1993.

- [48] T.T. Mo, Q. Xue, and C.H. Chan, "A broadband compact microstrip rat-race hybrid using a novel CPW inverter," *IEEE Trans. Microw. Theory Tech.*, vol. 55, no. 1, pp. 161–167, Jan. 2007.
- [49] L.K. Yeung, and Y.E. Wang, "A novel 180° hybrid using broadside coupled asymmetric coplanar striplines," *IEEE Trans. Microw. Theory Tech.*, vol. 55, no. 12, pp. 2625–2630, Dec. 2007.
- [50] M.E. Bialkowski, and Y. Wang, "Wideband Microstrip 180° Hybrid Utilizing Ground Slots," *IEEE Microw. Wireless Compon. Lett.*, vol. 20, no. 9, pp. 495-497, Sep. 2010.
- [51] A.M. Abbosh, and M.E. Bialkowski, "Design of a UWB planar 180° hybrid exploiting microstrip-slot transitions," *Microwave and Optical Technology Letters*, vol. 49, no. 6, pp. 1343-1346, Jun. 2007.
- [52] N. Yang, C. Caloz, and K. Wu, "Broad-band compact 180° hybrid derived from the Wilkinson divider," *IEEE Trans. Microw. Theory Tech.*, vol. 58, no. 4, pp. 1030–1037, Apr. 2010.
- [53] R.H. DuHamel, and M.E. Armstrong, "The tapered-line magic-T," *Parallel-coupled lines and directional couplers*, Artech House, pp. 207-233, 1972.
- [54] R.W. Klopfenstein, "A transmission line taper of improved design," *Proc. IRE*, vol. 44, pp. 31-35, Jan. 1956.
- [55] J.P. Shelton, and J.A. Mosko, "Synthesis and design of wide-band equal-ripple TEM directional couplers and fixed phase shifters", *IEEE Trans. Microwave Theory Tech.*, vol. MTT-14, pp. 462-473, Oct. 1966.
- [56] J.P. Shelton, "Impedance of offset parallel-coupled strip transmission lines," *IEEE Trans. Microw. Theory Tech.*, vol. MTT-14, pp. 7-15, Jan. 1966.
- [57] M.N.O. Sadiku, *Numerical Techniques in Electromagnetics*, second edition, CRC Press, Florida, pp. 308-311, 2000.
- [58] Y. Chun, and J. Hong, "Compact wideband branch-line hybrids," *IEEE Trans. Microw. Theory Tech.*, vol. 54, no. 2, pp. 704–709, Feb. 2006.
- [59] A. Abbosh, and M. Bialkowski, "Design of compact directional couplers for UWB applications," *IEEE Trans. Microw. Theory Tech.*, vol. 55, no. 2, pp. 189–194, Feb. 2007.

- [60] P.S. Rao, "How to design a broadband stepped quadrature hybrid coupler in triplate stripline configuration", *EE Times*, 8 Dec. 2008.
- [61] E.G. Cristal, and L. Young, "Theory and tables of optimum symmetric TEM mode coupled-transmission-line directional couplers," *IEEE Trans. Microw. Theory Tech.*, vol. MTT-13, pp. 544-558, Sep. 1965.
- [62] D.E. Goldberg, *Generic Algorithms in Search, Optimization, and Machine Learning*, Addison-Wesley, Massachusetts, 1989.
- [63] J.A. Nelder, and R. Mead, "A Simplex Algorithm for Function Minimization," *Computer J.*, vol. 7, pp. 308-313, 1965.
- [64] D. Turner, R. Wilhelm, and W. Lemberg, *Line Calc*, Agilent Technol., California, 2000.
- [65] J. Huang, "A Technique for an Array to Generate Circular Polarization with Linearly Polarized Elements," *IEEE Trans. Antennas Propag.*, vol. AP-34, no. 9, pp. 1113-1124, Sep. 1986.
- [66] A.E.C. Tan, M.Y.W. Chia, K.K.M. Chan, and K. Rambabu, "Modeling the Transient Radiated and Received Pulses of Ultra-Wideband Antennas," *IEEE Trans. Antennas Propag.*, vol. 61, no. 1, pp. 338-345, Jan. 2013.
- [67] M. Wukitsch, M. Petterson, D. Tobler, and J. Pologe, "Pulse oximetry: Analysis of theory, technology, and practice," *J. Clin. Monit.*, vol. 4, pp. 290-301, 1988.
- [68] T.E. McEwan, "Body monitoring and imaging apparatus and method," US Patent 5,766,208, 1996.
- [69] I.Y. Immoreev, S. Samkov, and T.H. Tao, "Short-distance ultrawideband radars," *IEEE A&E Systems Magazine*, pp. 9-14, Jun. 2005.
- [70] M.Y.H. Chia, S.W. Leong, C.K. Sim, and K.M. Chan, "Through-wall UWB radar operating within FCC's mask for sensing heart beat and breathing rate," *35th Eur. Microw. Conf.*, pp. 1991-1994, Oct. 2005.
- [71] M. Leib, W. Menzel, B. Schleicher, and H. Schumacher, "Vital signs monitoring with a UWB radar based on a correlation receiver," *Eur. Antennas Propag. Conf.*, pp. 1-5, Apr. 2010.
- [72] A. Lazaro, D. Girbau, R. Villarino, and A. Ramos, "Vital signs monitoring using impulse based UWB signal," *41st Eur. Microw. Conf.*, pp. 135-138, Oct. 2011.

- [73] E.F. Greneker, "Radar Sensing of Heartbeat and Respiration at a Distance with Security Applications," *Proc. of SPIE, Radar Sensor Technology II*, vol. 3066, pp. 22-27, Orlando, Florida, Apr. 1997.
- [74] P. Wu, J. Jau, C. Li, T. Horng, and P. Hsu, "Phase- and Self-Injection Locked Radar for Detecting Vital Signs with Efficient Elimination of DC Offsets and Null Points," *IEEE Trans. Microw. Theory Tech.*, vol. 61, no. 1, pp. 685-695, Jan. 2013.
- [75] C. Li, X. Yu, C. Lee, D. Li, L. Ran, and J. Lin, "High-Sensitivity Software-Configurable 5.8-GHz Radar Sensor Receiver Chip in 0.13- μ m CMOS for Noncontact Vital Sign Detection," *IEEE Trans. Microw. Theory Tech.*, vol. 58, no. 5, pp. 1410-1419, May 2010.
- [76] R. Fletcher, and J. Han, "Low-cost differential front-end for Doppler radar vital sign monitoring," *IEEE MTT-S Int. Microw. Symp. Dig.*, pp. 1325-1328, Jun. 2009.
- [77] Y. Shen, and C.L. Law, "A microstrip-fed quasi-spiral circularly polarized ultra-wideband antenna," *IEEE Intl. Symp. on Antenna and Propag. (APSURSI)*, pp. 1463-1466, 3-8 Jul. 2011.
- [78] J. Pourahmadazar, C. Ghobadi, J. Nourinia, N. Felegari, and H. Shirzad, "Broadband CPW-Fed Circularly Polarized Square Slot Antenna With Inverted-L Strips for UWB Applications," *IEEE Antenna and Wireless Propag. Letters*, vol. 10, pp. 369-372, 2011.
- [79] J.P. Shinde, R. Kumar, M.D. Uplane, and P.N. Shinde, "Circularly polarized rectangular slot antenna with trapezoidal tuning stub for UWB application," *IEEE Applied Electromag. Conf. (AEMC)*, pp. 1-4, 18-22 Dec. 2011.
- [80] J.D. Taylor, *Introduction to Ultra-Wideband Radar Systems*, Boca Raton, Florida: CRC Press, 1994.
- [81] B. Woche, T. Pfendler, and H. Pfitzemaier, "Method and apparatus utilizing time-expanded pulse sequences for distance measurement in a radar," US Patent 4132991, 1979.
- [82] T. Teshirogi, M. Tanaka, and W. Chujo, "Wideband Circularly Polarized Array Antenna with Sequential Rotations and Phase Shift of Elements," *Proc. of ISAP*, pp. 117-120, 1985.
- [83] R. Sugarman, "Sampling Oscilloscope for Statistically Varying Pulses," *The Review of Scientific Instruments*, vol. 28, no. 11, pp. 933-938, Nov. 1957.
- [84] B.-K. Park, O. Boric-Lubecke, and V. M. Lubecke, "Arctangent Demodulation With DC Offset Compensation in Quadrature Doppler Radar Receiver Systems," *IEEE Trans. Microw. Theory Tech.*, vol. 55, no. 5, pp. 1073-1079, May 2007.

- [85] Øyvind Aardal *et al.*, “Physical Working Principles of Medical Radar,” *IEEE Trans. Biomed. Eng.*, vol. 60, no. 4, pp. 1142- 1149, Apr. 2013.
- [86] Agilent, Basics of Measuring the Dielectric Properties of Materials, Application note 5989-2589EN, Apr. 2013.
- [87] E.L. Holzman, “Wideband Measurement of the Dielectric Constant of an FR4 Substrate Using a Parallel-Coupled Microstrip Resonator,” *IEEE Trans. Microw. Theory Tech.*, vol. 54, no. 7, pp. 3127-3130, Jul. 2006.
- [88] K.P. Lätti, M. Kettunen, J.P. Ström, and P. Silventoinen, “A Review of Microstrip T-Resonator Method in Determining the Dielectric Properties of Printed Circuit Board Materials,” *IEEE Trans. Instrum. and Meas.*, vol. 56, no. 5, pp. 1845-1850, Oct. 2007.
- [89] A. Deutsch *et al.*, “Extraction of $\epsilon_r(f)$ and $\tan \delta(f)$ for Printed Circuit Board Insulators Up to 30 GHz Using the Short-Pulse Propagation Technique”, *IEEE Trans. Adv. Packg.*, vol. 28, no. 1, pp. 4-9, Feb. 2005.
- [90] A.N. Franc, E. Pistono, and P. Ferrari, “Characterization of Thin Dielectric Films up to Mm-wave Frequencies Using Patterned Shielded Coplanar Waveguides,” *IEEE Microw. Wirel. Compon. Lett.*, vol. 22, no. 2, pp. 100-102, Feb. 2012.
- [91] C. Zhao, Q. Jiang, and S. Jing, “Calibration-Independent and Position-Insensitive Transmission/Reflection Method for Permittivity Measurement With One Sample in Coaxial Line,” *IEEE Trans. Electromagn. Compat.*, vol. 53, no. 3, pp. 684-689, Aug. 2011.
- [92] N.J. Farcich, J. Salonen, and P.M. Asbeck, “Single-Length Method Used to Determine the Dielectric Constant of Polydimethylsiloxane,” *IEEE Trans. Microw. Theory Tech.*, vol. 56, no. 12, pp. 2963-2971, Dec. 2008.
- [93] D.L. Faircloth, M.E. Baginski, and S.M. Wentworth, “Complex Permittivity and Permeability Extraction for Multilayered Samples Using S-Parameter Waveguide Measurements,” *IEEE Trans. Microw. Theory Tech.*, vol. 54, no. 3, pp. 1201-1209, Mar. 2006.
- [94] D.V. Blackham, and R.D. Pollard, “An Improved Technique for Permittivity Measurements Using a Coaxial Probe,” *IEEE Trans. Instrum. Meas.*, vol. 46, no. 5, pp. 1093-1099, Oct. 1997.
- [95] M. Chen, and C. Chen, “Improved Permittivity Calibration Method for Wideband In Situ Permittivity Probe,” *IEEE Geosci. Remote Sens. Lett.*, vol. 10, no. 2, pp. 323-327, Mar. 2013.

- [96] Y.K. Yeow, and Z. Abbas, "Fringing Field Correction of Admittance Model for Open-Ended Coaxial Sensor," *IEEE Sensors J.*, vol. 12, no. 5, pp. 1468-1469, May 2012.
- [97] M.D. Janezic, E.F. Kuester, and J. Baker-Jarvis, "Broadband complex permittivity measurements of dielectric substrates using a split-cylinder resonator," *Proc. IEEE MTT-S Int. Microw. Symp. Dig.*, Fort Worth, TX, pp. 1817-1820, Jun. 2004.
- [98] P.I. Dankov, "Two-resonator method for measurement of dielectric anisotropy in multilayer samples," *IEEE Trans. Microw. Theory Tech.*, vol. 54, no. 4, pp. 1534-1544, Apr. 2006.
- [99] D.K. Ghodgaonkar, V.V. Varadan, and V.K. Varadan, "A free-space method for measurement of dielectric constant and loss tangent at microwave frequencies," *IEEE Trans. Instrum. Meas.*, vol. 37, no. 3, pp. 789-793, Jun. 1989.
- [100] E.J. Rothwell, "Extraction of the wideband dielectric properties of a material layer using measured natural frequencies," *IEEE Trans. Antennas Propag.*, vol. 58, no. 2, pp. 620-623, Feb. 2010.
- [101] J.A. Hejase, P.R. Paladhi, and P. "Prem" Chahal, "Terahertz Characterization of Dielectric Substrates for Component Design and Nondestructive Evaluation of Packages," *IEEE Trans. Comp., Packag., Manuf. Technol.*, vol. 1, no. 11, pp.1685-1694, Nov. 2011.
- [102] C. Cadieu, and R. Fletcher, "Low-Cost Electronic Sensors for Air, Water, Soil, and Food," The Media Laboratory, Massachusetts Institute of Technology.
- [103] K. Sarabandi, E.S. Li, and A. Nashashibi, "Modeling and Measurements of Scattering from Road Surfaces at Millimeter-Wave Frequencies," *IEEE Trans. Antennas Propagat.*, vol. 45, no. 11, pp. 1679-1688, Nov. 1997.
- [104] E.C. Fear, S.C. Hagness, P.M. Meaney, M. Okoniewski, and M.A. Stuchly, "Enhancing breast tumor detection with near-field imaging," *IEEE Microw. Magazine*, vol. 3, no. 1, pp. 48-56, Mar. 2002.
- [105] A.M. Nicolson, and G.F. Ross, "Measurement of the intrinsic properties of materials by time domain techniques," *IEEE Trans. Instrum. Meas.*, vol. IM-19, pp. 377-382, Nov. 1968.
- [106] W.B. Weir, "Automatic measurement of complex dielectric constant and permeability at microwave frequencies," *Proc. IEEE*, vol. 62, no. 1, pp. 33-36, Jan. 1974.

- [107] I. Cuinas, and M. Sanchez, "Building material characterization from complex transmissivity measurements at 5.8 GHz," *IEEE Trans. Antennas Propagat.*, vol. 48, no. 8, pp. 1269-1271, Aug. 2000.
- [108] R.V. de Jongh, J. Marti-Canales, and L.P. Ligthart, "Analysis of time domain radar cross-section measurements in compact ranges," *Electron. Lett.*, vol. 36, no. 24, pp. 1986-1987, Nov. 2000.
- [109] D.M. Le Vine, "The Radar Cross Section of Dielectric Disks," *IEEE Trans. Antennas Propagat.*, vol. AP-32, no. 1, pp. 6-12, Jan. 1984.
- [110] L. Li, A.E.C. Tan, K. Jhamb, and K. Rambabu, "Characteristics of Ultra-Wideband Pulse Scattered From Metal Planar Objects," *IEEE Trans. Antennas Propagat.*, vol. 61, no. 6, pp. 3197- 3206, Jun. 2013.
- [111] L. Li, "Analysis of Ultra-Wideband Pulse Scattered from Planar Objects," *M.S. Thesis*, ECE Dept., Univ. Alberta, Edmonton, Canada, 2012.
- [112] E.F. Knott, M.T. Tuley, and J.F. Shaeffer, *Radar Cross Section*, 2nd ed. Raleigh, NC: SciTech, 2004.
- [113] A.N. Peiris *et al.*, "Adiposity, fat distribution, and cardiovascular risk," *Ann. Intern. Med.*, vol. 110, pp. 867-872, Jun. 1989.
- [114] K. Tokunaga, Y. Matsuzawa, K. Ishikawa, and S. Tarui, "A novel technique for the determination of body fat by computed tomography," *Int. J. Obes.*, vol. 7, no. 5, pp. 437-445, 1983.
- [115] H. Kvist, B. Chowdhury, L. Sjostrom, U. Tylen, and A. Cederblad, "Adipose volume determination in males by computed tomography and 40K," *Int. J. Obes.*, vol. 12, pp. 249-266, 1988.
- [116] R. Suzuki *et al.*, "Abdominal wall fat index, estimated by ultrasonography, for assessment of the ratio of visceral fat to subcutaneous fat in the abdomen," *Am. J. Med.*, vol. 95, pp. 309-314, 1993.
- [117] J.C. Seidell, C.J.G. Bakker, and K. Van der Kooy, "Imaging techniques for measuring adipose-tissue distribution: a comparison between computed tomography and 1.5T magnetic resonance," *Am. J. Clin. Nutr.*, vol. 51, pp. 953-957, 1990.

- [118] A. Peyman, S. Holden, and C. Gabriel, "Dielectric properties of tissues at microwave frequencies," a research report for mobile telecommunications and health research programme, Dec. 2009.
- [119] E.R. Miller, and D.E. Ullrey, "The pig as a model for human nutrition," *Ann. Rev. Nutr.*, vol. 7, pp. 361-382, 1987.
- [120] W.G. Pond, and H.J. Mersmann, *Biology of the domestic pig*, Comstock Pub. Associates: Cornell University Press, 2001.
- [121] J.M. Kim *et al.*, "In Vitro and In Vivo Measurement for Biological Applications Using Micromachined Probe," *IEEE Trans. Microw. Theory Tech.*, vol. 53, no. 11, pp. 3415-3421, Nov. 2005.
- [122] MacAnatomy, *Cardiovascular Anatomy* [online], available:
http://macanatomy.mcmaster.ca/index.php?option=com_content&id=219%3Aheart-1&Itemid=111
- [123] S. Pfaffenberger *et al.*, "Size Matters!: Impact of Age, Gender, Height, and Weight on the Normal Heart Size," *American Heart Association Circulation: Cardiovascular Imaging*, Sept. 2013.
- [124] K.D. Fairbanks, *Alcoholic liver disease* [online], available:
<http://www.clevelandclinicmeded.com/medicalpubs/diseasemanagement/hepatology/alcoholic-liver-disease/>
- [125] A. Ivorra, "Bioimpedance Monitoring for physicians: an overview," Biomedical Applications Group, CNM Barcelona, 2002.
- [126] N. Secher, and J.J.V. Lieshout, "Normovolaemia defined by central blood volume and venous oxygen saturation," *Clin. Exp. Pharmacol. Physiol.*, vol. 32, pp. 901-910, 2005.
- [127] S. Svenmarker *et al.*, "Central venous oxygen saturation during cardiopulmonary bypass predicts 3-year survival," *Interact. CardioVasc. Thorac. Surg.*, vol. 16, pp. 21-26, Oct. 2012.